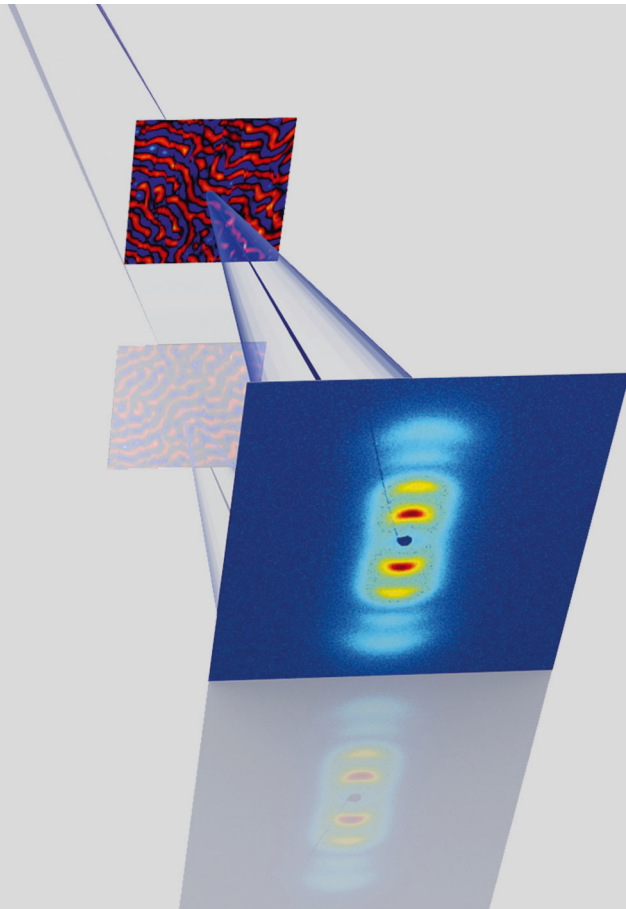


Resonant Magnetic Scattering Studies using Synchrotron Radiation and Laser-Generated Extreme Ultraviolet Light

Christian Michael Weier



Schlüsseltechnologien /
Key Technologies
Band/ Volume 105
ISBN 978-3-95806-052-4

Forschungszentrum Jülich GmbH
Peter Grünberg Institute (PGI)
Electronic Properties (PGI-6)

Resonant Magnetic Scattering Studies using Synchrotron Radiation and Laser-Generated Extreme Ultraviolet Light

Christian Michael Weier

Schriften des Forschungszentrums Jülich
Reihe Schlüsseltechnologien / Key Technologies

Band / Volume 105

ISSN 1866-1807

ISBN 978-3-95806-052-4

Bibliographic information published by the Deutsche Nationalbibliothek.
The Deutsche Nationalbibliothek lists this publication in the Deutsche
Nationalbibliografie; detailed bibliographic data are available in the
Internet at <http://dnb.d-nb.de>.

Publisher and Distributor:	Forschungszentrum Jülich GmbH Zentralbibliothek 52425 Jülich Tel: +49 2461 61-5368 Fax: +49 2461 61-6103 Email: zb-publikation@fz-juelich.de www.fz-juelich.de/zb
Cover Design:	Grafische Medien, Forschungszentrum Jülich GmbH
Printer:	Grafische Medien, Forschungszentrum Jülich GmbH
Copyright:	Forschungszentrum Jülich 2015

Schriften des Forschungszentrums Jülich
Reihe Schlüsseltechnologien / Key Technologies, Band / Volume 105

D 464 (Diss., Duisburg, Univ., 2015)

ISSN 1866-1807

ISBN 978-3-95806-052-4

The complete volume is freely available on the Internet on the Jülicher Open Access Server (JuSER)
at www.fz-juelich.de/zb/openaccess.

Neither this book nor any part of it may be reproduced or transmitted in any form or by any
means, electronic or mechanical, including photocopying, microfilming, and recording, or by any
information storage and retrieval system, without permission in writing from the publisher.

Zusammenfassung

In dieser Arbeit werden magnetische Domänenstrukturen von ferromagnetischen Filmen mittels resonanter magnetischer Streuung (RMS) untersucht. Dafür wird zum einen Synchrotronstrahlung im weichen Röntgenbereich und zum anderen extrem ultraviolette (EUV, engl. XUV) Strahlung einer laserbasierten Laborlichtquelle verwendet. Die Synchrotronmessungen geben detaillierte Informationen über die Eigenschaften magnetischer Domänen mit Nanometerpräzision und Elementkontrast. Diese technischen Vorteile gegenüber anderen magnetischen Abbildungsverfahren ermöglichen Untersuchungen der Domänenstruktur individueller Schichten in komplexen Probensystemen wie FePd/CoPd-Zweifachschichten oder CoPd/Pd/NiFe-Dreifachschichten.

Zeitaufgelöste Experimente mit sichtbarer Laserstrahlung werden durchgeführt, um die ultraschnelle Entmagnetisierung in FePd/CoPd-Zweifachlagen genauer zu verstehen. Dabei wird insbesondere der Einfluss von intensiven Laserpulsen auf die magnetische Kopplung der beiden Filme untersucht. Durch die verwendete Messtechnik kann die zeitliche Entwicklung der Magnetisierung sehr genau verfolgt werden, aber es ist auf Grund des begrenzten Auflösungsvermögen nicht möglich magnetische Domänen mit Abmessungen auf der Nanometerskala abzubilden.

Folglich wird eine neue Methode benötigt, um die Domänenstruktur und die ultraschnelle Magnetisierungsdynamik zur gleichen Zeit aufzulösen. Dieses Ziel motiviert die wichtigste Fragestellung dieser Arbeit: Ist eine Laborlichtquelle, die hohe harmonische Ordnungen von infraroten Laserpulsen generiert [engl. high-order harmonic generation (HHG)], in der Lage, genügend EUV-Strahlung für Streuexperimente an magnetischen Domänen zu erzeugen? In diesem Zusammenhang wird gezeigt, wie intensive Laserbestrahlung permanente und reversible Modifikationen der Domänenstruktur und der Morphologie verursacht.

Zum Schluss wird nicht-magnetische Streuung und Beugung an einer Kante verwendet, um Kohärenzeigenschaften der erzeugten EUV-Strahlung zu untersuchen. Die Resultate zeigen die Vorteile und die Beschränkungen der HHG-Lichtquelle für Anwendungen, die eine hohe Kohärenz erfordern.

Abstract

In this thesis magnetic domain patterns of ferromagnetic alloys are studied using resonant magnetic scattering (RMS). For this purpose synchrotron radiation in the soft X-ray range and laser-based extreme ultraviolet (XUV) light from a laboratory light source are employed. The synchrotron measurements give detailed information about the properties of magnetic domains with nanometer precision and element selectivity. These specialties allow investigations of domain patterns of complex layered systems, including FePd/CoPd bilayers or CoPd/Pd/NiFe trilayers.

Time-resolved experiments with visible laser radiation are conducted to examine the laser-induced demagnetization of FePd/CoPd bilayers, pointing out the influence of intense laser pulses on the magnetic coupling of the two layers. This technique is capable of tracing the temporal evolution of the magnetization, nevertheless it cannot image nanometer-sized magnetic domains due to the limited spatial resolution.

Consequently, a new approach is necessary to resolve domain patterns and ultrafast magnetization dynamics at the same time. This aim motivates the most important question addressed in this thesis: whether a tabletop XUV light source based on high-order harmonic generation (HHG) can be used for RMS experiments on magnetic domain patterns. In this context it is further shown, how intense laser exposure causes permanent and reversible modifications of the magnetic nanostructure and the sample morphology.

Finally, coherence properties of the generated XUV radiation are examined, using non-magnetic scattering at grains and knife-edge diffraction. The results obtained reveal the advantages and limitations of HHG sources for applications which demand a high light coherence.

Contents

1	Introduction	1
2	Fundamentals	5
2.1	Magnetism, Anisotropies and Domains	5
2.1.1	Magnetism of Transition Metals	5
2.1.2	Energy Terms in Magnetism	6
2.1.3	Magnetic Anisotropy in Co/Pt Multilayers	8
2.1.4	Magnetic Anisotropy in CoPd Alloys	9
2.1.5	Magnetic Anisotropy in FePd Alloys	10
2.1.6	Magnetic Domains	11
2.2	Classical Description of Magneto-Optics	14
2.3	Resonant Magnetic Scattering	17
2.3.1	Related Experimental Findings	22
3	Coupled Domain Patterns studied with X-ray based RMS	27
3.1	Introduction	27
3.2	Sample Characterization	28
3.3	Experimental Setup	32
3.4	Results and Discussion	36
3.4.1	CoPd and FePd Films	39
3.4.2	Micromagnetic Simulations	44
3.4.3	FePd/CoPd Bilayers	47
3.4.4	CoPd/Pd/NiFe Trilayers	49
3.4.5	Resonant Magnetic Scattering at Pd M-Edges	52
3.5	Conclusion	55
4	Ultrafast Magnetization Dynamics in FePd/CoPd Bilayers	57
4.1	Introduction	57

4.2	Experimental Setup	59
4.3	Results and Discussion	62
4.4	Conclusion	66
5	Resonant Magnetic Scattering with Tabletop XUV Radiation	69
5.1	Introduction	69
5.1.1	Laser Amplifier System	69
5.1.2	High-order Harmonic Generation	71
5.2	Experimental Setup	75
5.2.1	Considerations for the RMS Intensity	78
5.2.2	Spectrum of the HHG Source	79
5.3	Results and Discussion	82
5.3.1	Sample Characterization using MOKE and MFM	82
5.3.2	RMS with HHG - The Proof of Principle	84
5.3.3	Laser-induced Modifications of Co/Pt Multilayers	86
5.4	Conclusion	91
6	SAXS with Coherent XUV Light	93
6.1	Introduction	93
6.2	SAXS from Fe and FePd Grains	97
6.2.1	Sample Fabrication	97
6.2.2	Experimental Setup	97
6.2.3	Results and Discussion	99
6.2.4	Coherence and Speckle Contrast Considerations	104
6.3	Knife-Edge Diffraction	108
6.3.1	Experimental Setup	108
6.3.2	Results and Discussion	109
6.4	Conclusion	112
7	Summary and Outlook	113
	Bibliography	115
	Publications	133
	Conference Contributions	135

Danksagung	137
Curriculum Vitae	141
Erklärung	143

1 Introduction

The idea of storing information on a magnetic disc revolutionized information technology. Almost 60 years have passed since the commercial introduction of the first hard disc drives and great improvements of this technology were achieved implementing novel scientific concepts. A dramatic increase of the data density was accomplished by the miniaturization of hard disc read heads [1]. These sensors measure the magnetic stray field of magnetic bits using the *giant magnetoresistance* (GMR) effect, which was independently discovered by Albert Fert and Peter Grünberg [2, 3]. In layered systems, which contain two ferromagnetic layers separated by a non-magnetic spacer, the GMR effect results in pronounced dependence of the resistance on the relative orientation of the magnetic layers. Due to the importance of their discovery, Albert Fert and Peter Grünberg were awarded with the Nobel Prize in physics in 2007.

The areal density for data storage and especially for *longitudinal recording*, meaning that the magnetization vector of the bit is lying in the plane of the hard disc, is limited by the *superparamagnetic* effect, which involves thermally activated fluctuations of the magnetization for small ferromagnetic entities [4]. This effect prohibits stable and reliable data storage. By introducing *perpendicular recording media* the areal density was significantly increased, as the magnetization is oriented out-of-plane and the superparamagnetic effect is reduced by a strong magnetic anisotropy [5]. Prominent examples for perpendicular recording media are Co/Pt and Co/Pd multilayers and alloys, which have been intensively investigated during the last years and are also examined in this work [6–10]. On the other hand, magnetic films with a large perpendicular anisotropy demand larger switching fields, which are difficult to reach on a very small scale. This motivates a new concept for data storage, known as *heat-assisted magnetic recording*, where a laser heats the magnetic film close to the Curie temperature to reduce the switching field during the writing process [11]. Another improvement of the areal density can be achieved by *bit patterned media*. For these devices nanometer-sized magnetic grains are synthesized, which define the dimension of a single bit [12].

The above mentioned rapid development of data storage technology was only possible due to the discovery of many physical effects involving the electronic spin. They form a new research field, known as *spinelectronics*. The list of effects, which have scientific relevance, contains prominent examples like *interlayer exchange coupling* [13], *tunneling magnetoresistance* [14], *spin-transfer torque* [15], *spin Hall effect* [16] and *Spin Seebeck effect* [17].

Not only the higher storage density encourages new research, but also the timescale of magnetic switching processes has been thoroughly studied and is still subject of many surveys. For example, typical domain wall nucleation and propagation processes occur on the milli- to nanosecond regime [18], while Larmor precessions of magnetic moments are visible in the nano- to picosecond range [19]. Remarkably, it has been demonstrated by laser-induced switching and ultrafast demagnetization experiments that magnetism can even be manipulated on the femtosecond timescale [20, 21]. The pioneering studies by Beaupaire *et al.* in 1996 showed the possibility to quench the magnetization of a Ni film within hundreds of femtoseconds and motivated intense research involving theoretical models and experiments [22]. As described in Chapter 4, several models of the underlying microscopic processes causing the demagnetization have been proposed, taking into account the fundamental interactions between photons, spins, phonons and magnons. Although these models are capable to explain certain laser-induced effects, the general theory that includes an ultrafast channel for the dissipation of spin angular momentum has not been identified so far. However, the understanding of ultrafast spin dynamics was significantly supported by the fabrication of advanced magnetic material systems, based on the experience from spinelectronic research [23–25]. The experimental results obtained during the last years emphasize the importance of spin-dependent transport of laser-excited electrons, which may contribute to the ultrafast demagnetization process [25–30].

The temporal evolution of the magnetization is typically analyzed in a stroboscopic manner using the pump-probe technique. Typically, intense femtosecond pulses from Ti:Sapphire lasers, also called pump pulses, trigger the dynamical process, while a delayed weaker laser pulse probes the magnetization using magneto-optical effects. However, the complexity of the topic demands contemporary methods in order to gain deeper insights into ultrafast magnetization dynamics. These methods involve for instance element selectivity, provided by X-rays or XUV radiation. A very efficient way to obtain an element-specific measure of the magnetization are helicity-dependent photoabsorption measurements, because the X-ray magnetic circular dichroism (XMCD) effect is resonantly enhanced at certain absorption

edges [31]. The transmission of light through a magnetic film consequently depends on the light helicity and on the orientation the magnetization vector relative to the light wavevector [32]. Synchrotron light sources are the first choice for XMCD spectroscopy, as they deliver an intense X-ray flux with a very well defined photon energy and polarization. In general, investigations in the femtosecond regime are not possible with synchrotron radiation, because the pulse duration is in the order of tens of picoseconds. However, new approaches using femtosecond-slicing and free-electron lasers have been successfully introduced for studying ultrafast magnetization dynamics with XUV radiation or soft X-rays [27, 33], but the access to such facilities is limited. Therefore, an appropriate laboratory light source is strongly desired. Recently, HHG sources driven by intense femtosecond laser-pulses pave the way for time-resolved and element-selective measurements of ultrafast demagnetization [34]. Such tabletop light sources produce an intense XUV photon flux, which is bright enough for transverse magneto-optical Kerr effect (TMOKE) investigations at the $M_{2,3}$ edges of the 3d ferromagnets (50–70 eV) [35–37]. Latest results of pump-probe studies using HHG radiation could substantially contribute to the understanding of femtosecond magnetization dynamics and revealed the role of superdiffusive spin transport [25, 38]. Another advantage of XUV light and soft X-rays is a small wavelength in the range of several nanometers. This enables imaging of nanometer-sized objects that cannot be resolved with visible light according to the Abbe diffraction limit. It has been demonstrated that HHG sources can even be employed for advanced experimental approaches including Fresnel ptychography [39]. Thus, ultrashort-pulse XUV sources potentially allow imaging experiments of magnetic domains, enabling surveys of the fundamental quantities of nanomagnetism. Very recently, resonant magnetic scattering experiments using free-electron lasers [40] and tabletop HHG sources [41] addressed this issue and demonstrated the capabilities of the new approaches. Moreover, the analysis of the time-resolved RMS data revealed laser-induced modifications of the domain walls [27]. These changes of the magnetic structure have also been related to superdiffusive spin currents.

In this thesis layered magnetic samples, consisting of FePd and CoPd alloys, are investigated. Therefore, **Chapter 2** summarizes general aspects of the magnetic properties of these materials and provides the fundamental basis for the understanding of resonant magnetic scattering.

The synthesized alloys are examined in **Chapter 3** using X-ray based RMS. Magnetic field dependent studies elucidate the magnetic behavior of coupled magnetic domain patterns.

Furthermore, **Chapter 3** shows that the developed sample systems are interesting candidates for time-resolved RMS experiments, taking advantage of the element selectivity and the spatial resolution.

Chapter 4 presents time-resolved investigations of the fabricated FePd/CoPd bilayers employing visible laser pulses. This method is used to follow the temporal evolution of the saturation magnetization of the sample. Hysteresis loops are measured for different delays between the pump and probe pulses to study the influence of ultrashort laser pulses on the magnetic coupling of the two films. In addition, it is studied how hot electrons excited in a neighboring Au layer contribute to the laser-induced demagnetization of a CoPd film.

In **Chapter 5** the feasibility of RMS experiments with a tabletop HHG source is demonstrated. The comparison of an as-grown Co/Pt multilayer and a laser-exposed specimen shows strong differences in the RMS pattern. The laser-induced modifications are further analyzed by atomic and magnetic force microscopy (AFM and MFM).

Finally, it is shown in **Chapter 6** that HHG sources can be employed for studying changes of the sample morphology. In this context, coherence properties of the HHG radiation are evaluated by analyzing speckle patterns recorded in a small angle X-ray scattering (SAXS) geometry. Furthermore, light diffraction on a knife edge is presented and the obtained interference pattern is compared with the speckle pattern analysis, revealing the influence of the longitudinal and transverse coherence length in the different experiments. Both studies point out the possibilities of HHG sources for new applications, which could be used to investigate magnetic properties.

2 Fundamentals

2.1 Magnetism, Anisotropies and Domains

The magnetic properties of the thin films investigated in this thesis are mainly related to the ferromagnetic 3d transition metals, *i.e.*, iron, cobalt and nickel. Therefore, the origin of ferromagnetism in these elements is briefly explained and several important properties of the investigated magnetic alloys are presented. The discussions especially include the origin of magnetic anisotropies and the field-dependent behavior of magnetic domains. This chapter is based on the explanations given in [31, 42, 43], which provide many more details about magnetism and magnetic domains.

2.1.1 Magnetism of Transition Metals

Among the possible interactions, resulting in a parallel orientation of atomic magnetic moments, dipole-dipole interaction may be considered as the driving mechanism for magnetic order. However, it is simple to derive that the corresponding interaction energy is about 0.1 meV, which is much lower than the thermal energy at room temperature (~ 25 meV) [44]. Thus, dipole-dipole interaction can not explain ferromagnetic order at elevated temperatures. Instead, exchange interaction has been identified as the origin of ferromagnetism. The Pauli principle requires that two electrons with the same spin orientation cannot be localized at the same place. For a certain electron the electrostatic potential of the atom core is less efficiently screened by the remaining electrons with the same spin orientation. This causes a higher binding energy of the electron, corresponding to a reduction of the Coulomb energy. Moreover, the total energy can be further reduced, if more and more electrons align their spin in parallel. Thus, in the next neighborhood of a certain electron the density of electrons with the same spin orientation decreases as a consequence of exchange interaction, which is known as the "exchange hole". The total energy of the exchange hole is determined by the Coulomb energy and the kinetic energy. The latter one needs to be "payed", because the localization of an electron within the exchange hole is accompanied by an increase of

the kinetic energy according to Heisenberg's uncertainty principle.

A simple model developed by Stoner and Wohlfarth involves the electronic band structure, which is split and shifted in energy for spin-up and spin-down electrons [45]. In order to include exchange interaction, the one-electron energies are modified by $\pm I \cdot n_{\pm}/N$, where n_{\pm} is the number of spin-up and spin-down electrons, N is the number of atoms and I is the Stoner parameter, corresponding to the characteristic energy reduction induced by electron correlation. This approach yields a requirement for the presence of ferromagnetism, known as the Stoner criterion, which is given by

$$I \cdot D(E_F) \frac{V}{2N} > 1, \quad (2.1)$$

where V is the volume and $D(E_F)$ is the density of states at the Fermi energy E_F . The Stoner criterion is only fulfilled for iron, cobalt and nickel as a consequence of the high density of states at E_F . Some 4d elements are close to meet the criterion. One example is palladium, where the high value of $D(E_F)$ causes a large susceptibility, implying that Pd can be easily magnetized [42].

When the temperature increases, the ferromagnetic material undergoes a second-order phase transition at the Curie temperature T_C and becomes paramagnetic. Cobalt shows the highest T_C of 1395 K among the 3d transition metals. It has been demonstrated that alloying ferromagnets with non-magnetic elements results in a decrease of T_C . In Chapter 3 alloys of cobalt and palladium with the composition $\text{Co}_{35}\text{Pd}_{65}$ are investigated. The Curie temperature of this alloy is approximately 870 K [46], which is still far higher than room temperature.

2.1.2 Energy Terms in Magnetism

The origin of micromagnetic structures, like magnetic domains, can be understood, when the different contributions to the total free energy E_{tot} are taken into account [43]. Stable configurations are obtained by minimizing E_{tot} :

$$E_{tot} = \int [e_{exc} + e_{ani} + e_{stray} + e_{zee}] dV. \quad (2.2)$$

The different energy densities e_i include exchange interactions, magnetic anisotropies, stray fields and the Zeeman effect. At this point, magnetoelastic energy contributions are neglected.

As described in 2.1.1, the **exchange interaction** causes the parallel alignment of the magnetic moments in a ferromagnet. A deviation from the perfect parallel alignment demands a certain energy which can be expressed by:

$$e_{exc} = A [(\nabla m_x)^2 + (\nabla m_y)^2 + (\nabla m_z)^2]. \quad (2.3)$$

The exchange interaction is proportional to the gradient of the reduced magnetization ($\mathbf{m} = \mathbf{M}/M_s$), where M_s is the saturation magnetization. The material specific constant A is the exchange stiffness, which is typically in the order of 10^{-11} J/m for 3d ferromagnets.

The **Zeeman energy** regards the interaction of the magnetic moments with an external field \mathbf{H}_{ex} and reads

$$e_{zee} = -\mu_0 \mathbf{M} \cdot \mathbf{H}_{ex}. \quad (2.4)$$

This energy contribution favors a parallel alignment of \mathbf{M} and \mathbf{H}_{ex} .

The **stray field energy** is based on the magnetic field created by the magnet itself, which is called stray field H_s or demagnetizing field. The corresponding energy can be expressed by

$$E_{stray} = e_{stray} \cdot V = \frac{\mu_0}{2} \int_{allspace} \mathbf{H}_s^2 dV = -\frac{1}{2} \int_{sample} \mathbf{H}_s \cdot \mathbf{M} dV \quad (2.5)$$

The stray field is a consequence of the formation of "magnetic charges" and always gives a positive contribution to the total free energy [47]. Thus, the stray field energy can be minimized by avoiding magnetic charges, which is feasible when forming magnetic domains, as discussed below.

For a thin ferromagnetic film the stray field is much smaller, when orienting the magnetization parallel to the film plane. The difference in e_{stray} between an out-of-plane and in-plane orientation of the magnetization is known as shape anisotropy and amounts to:

$$e_{shape} = \frac{\mu_0}{2} M_s^2, \quad (2.6)$$

where M_s is the saturation magnetization. This energy density can be very high (\sim MJ/m³) [48] and it explains the in-plane anisotropy which is typically observed for magnetic thin films. Nevertheless, some materials show an out-of-plane anisotropy, which can be caused by very different effects, as discussed in the following.

The **magneto crystalline anisotropy** is mediated by spin-orbit interaction, which couples the orbital momentum with the electron spin. The electrostatic interaction energy of the electron clouds in a crystalline solid depends on the orientation and shape of the atomic orbitals. The overlap of the electron wavefunctions may be minimized, when the orbital angular momentum is oriented along certain crystallographic directions. The spin-orbit interaction couples the spin angular momentum accordingly and gives rise to energetically preferred spin orientations (easy axis of magnetization). For a uniaxial magnetic anisotropy the volume contribution to the energy density can be described by

$$e_{ani} = K_{1V} \cdot \sin^2(\theta) + K_{2V} \cdot \sin^4(\theta), \quad (2.7)$$

where K_{1V} and K_{2V} are the first- and second-order anisotropy constants and θ is the angle between the magnetization and the easy axis [7, 48].

2.1.3 Magnetic Anisotropy in Co/Pt Multilayers

When magnetic and non-magnetic thin films are repetitively grown on top of each other, the interface anisotropy can yield an out-of-plane easy axis. For very thin layers the absence of translation symmetry at the interface and the accompanied change in the chemical bonds can support an out-of-plane anisotropy, which is stronger than the shape anisotropy [49]. The energy density $K_{1,I}$ accounting for this interface effect adds to the first-order volume anisotropy. Including the shape anisotropy, the effective first-order anisotropy constant is given by

$$K_{1,eff} = K_{1,V} + \frac{2K_{1,I}}{d} - \frac{\mu_0}{2} M_s^2, \quad (2.8)$$

where d is the film thickness [7]. For $K_{1,eff} < 0$ and $K_2 < -1/2K_{1,eff}$ the magnetization lies in-plane, whereas for $K_{1,eff} > 0$ and $K_2 > -1/2K_{1,eff}$ the magnetic moments point out-of-plane. Different spin reorientation transitions from in-plane to out-of-plane are possible, when $K_{1,eff}$ and K_2 are changed. Either the magnetization undergoes this transition via a coexistence phase, where in-plane and out-of-plane domains exist at the same time [50–52], or the magnetization is tilted continuously from in-plane to out-of-plane [8, 53]. The later one has been found for Co/Pt multilayer films, which are investigated in Chapter 5. The important parameters for the magnetic behavior are the Co and Pt thicknesses and the number of repetitions of both layers. Other influences are related to the interface roughness

[54], interdiffusion processes during the deposition [55] and the crystalline orientation of the Co layers [56].

2.1.4 Magnetic Anisotropy in CoPd Alloys

CoPd alloys have been studied extensively and the main source for the observed perpendicular anisotropy has been ascribed to the **magnetoelastic effect** (or inverse **magnetostriction**), which relates the mechanical stress σ to the magnetization of the film. The corresponding magnetic anisotropy energy K_{me} is proportional to $\sigma \cdot \lambda_s$, where λ_s is the magnetostriction constant. Investigations of $\text{Co}_x\text{Pd}_{1-x}$ alloys have demonstrated that λ_s changes sign for $x \approx 0.5$ [57]. It has been shown that the deposition of 200 nm thick polycrystalline CoPd alloys on glass substrates leads to a strong out-of-plane anisotropy, which is maximal for 70–80 at.% Pd [58]. Moreover, this survey has demonstrated that the film thickness can strongly affect the magnetic structure. The obtained results support the assumption that the reduction of the film thickness below a certain value changes the stripe domain pattern to a single domain structure. Thus, the synthesized $\text{Co}_{35}\text{Pd}_{65}$ alloys, which are investigated in Chapter 3, are 40 nm thick to overcome the critical thickness required for an out-of-plane stripe domain pattern.

In Co/Pd multilayers, where the perpendicular anisotropy originates from the interface anisotropy (as mentioned above for the Co/Pt multilayer films), a change in magnetostriction was observed for very thin Co layers (thinner than 0.5 nm), which is caused by alloying of Co and Pd layers at the interface [59].

Nevertheless, a detailed investigation by Childress *et al.* of CoPd alloys grown by molecular beam epitaxy (MBE) onto (111)Ag layers points out the overestimation of magnetic anisotropies induced by magnetostriction [9]. For Ag/CoPd interfaces (8% mismatch) the strain-induced anisotropy amounts to 230 kJ/m^3 , but torque measurements yield a four times larger anisotropy constant. Consequently, other effects have to be regarded to explain the magnetic properties. One model involves the occurrence of the tetragonal L1_0 structure, which was observed in $\text{Co}_{50}\text{Pd}_{50}$ [60]. This crystalline phase can lead to a uniaxial magnetic anisotropy, as discussed below for 50-50 alloys of Fe and Pd. However, the ordered phase of $\text{Co}_{25}\text{Pd}_{75}$ is L1_2 , which is not known to produce a uniaxial anisotropy, unless interfaces between ordered and disordered phases break the symmetry or atomic slip planes occur, leading to a formation of Co pairs [61, 62]. Other studies claim that the MBE growth can result in a short-range order of the Co atoms [9, 63], giving rise to a uniaxial perpendicular anisotropy.

2.1.5 Magnetic Anisotropy in FePd Alloys

$\text{Fe}_{50}\text{Pd}_{50}$ alloys are known to grow under certain conditions in the **L1₀ structure**, which is tetragonal in symmetry and is atomically ordered. When a binary alloy crystallizes in the regular face-centered cubic (fcc) lattice structure, all lattice sites have the same probability to be occupied by a specific atom. The L1₀ structure can be understood as a stacking of (001) planes of the fcc structure, while the occupation of the planes alters continuously between the two types of atoms [64]. The regular fcc structure and the L1₀ structure are illustrated in Figs. 2.1(a) and (b).

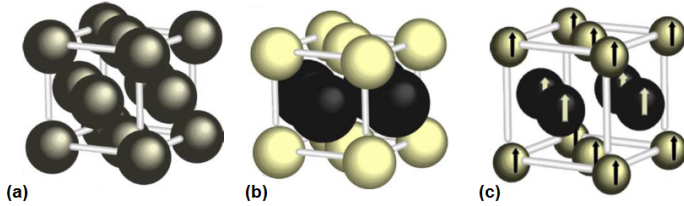


Figure 2.1: The regular fcc structure and the L1₀ structure are shown in (a) and (b). The two kind of atoms are indicated in by the different colors. The resulting anisotropy is schematically illustrated in (c) for a ferromagnetic L1₀ crystal [64].

For the L1₀ structure the symmetry is reduced compared to the regular fcc structure, giving rise to a magnetic anisotropy. For a ferromagnetic alloy the easy axis is oriented along the high symmetry axis of the structure, which is the [001] direction [Fig. 2.1(c)]. A variety of studies related the magnetic properties of FePd alloys to the crystallographic structure [65–70], pointing out important issues, which have to be considered for the growth of FePd. Several observations are summarized in the following.

For bulk $\text{Fe}_{50}\text{Pd}_{50}$ alloys the phase transition from a disordered fcc phase to the ordered L1₀ structure occurs at approximately 650 °C. For thin films, lower temperatures (200–600 °C) are sufficient to create the L1₀ structure, but the growth at low temperatures can result in a canting of the crystallographic c-axis with respect to the surface normal. In this case, the easy axis of magnetization is tilted accordingly. Moreover, it has been shown that the deposition at room temperature may result in a disordered fcc structure with an in-plane anisotropy. Thus, for a perpendicular easy axis it is necessary to grow the alloy at higher temperatures and the films have to be thicker than a certain critical thickness, which is in the order of 30 nm. Reported uniaxial anisotropy constants of FePd alloys are in the order of 1–2 MJ/m² [66, 71].

2.1.6 Magnetic Domains

For a ferromagnetic film with a strong out-of-plane anisotropy the exchange interaction prefers a parallel alignment of the magnetic moments and thus a uniform perpendicular magnetization. In this situation, the stray field energy would be very large and the magnetization may break into domains separated by thin domain walls to reduce the stray field energy. Inside one domain the atomic magnetic moments are aligned in parallel, but the magnetization vectors of neighboring domains can be oriented in very different directions. This scenario is depicted in Fig. 2.2, where the uniform magnetization (a) splits into oppositely aligned domains (b). More domains can further decrease the stray field (c), but for each domain wall the exchange and anisotropy energy contributions increase. In addition, closure domains have been observed, yielding a flux closure of the magnetic stray field (d) [72].

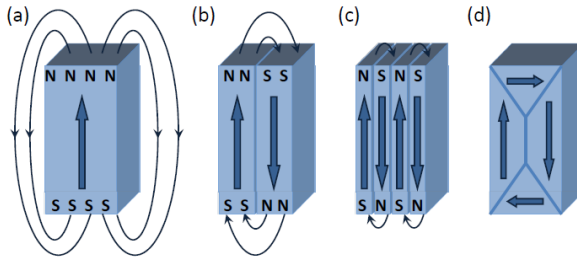


Figure 2.2: The uniform magnetization in (a) breaks into 180° domains in (b) and (c). Depending on the energetics of the ferromagnetic it is favorable to create more or fewer domain walls. Even an entire flux closure can occur (d) [44].

In the following, important properties of magnetic domains are summarized. The discussion is based on the detailed description given in Ref. [43].

For the understanding of the field dependent behavior of the magnetic domains it is important to regard the domain walls, which are separating the domains from each other. It has been demonstrated that different types of domain walls can occur, which are known as **Bloch** and **Néel** walls. In a Bloch wall the magnetization rotates continuously within a plane parallel to the domain wall, whereas the rotation plane of a Néel wall is perpendicular to the domain wall. The two domain wall types are illustrated in Fig. 2.3. Both of them contribute to the complex magnetic structure of the domain pattern, as described in the micromagnetic simulations presented in Chapter 3.

Within a Bloch wall the magnetization rotates away from the easy axis to the antiparallel orientation. Therefore the anisotropy energy favors small domain walls. The exchange energy prefers a parallel alignment of adjacent magnetic moments and thus larger domain walls are desirable for reducing the exchange energy. The width of a Bloch wall is given by $\delta_w = \pi\sqrt{A/K_{1,eff}}$, where A is the exchange stiffness constant and $K_{1,eff}$ the effective anisotropy constant under the assumption that $K_2 = 0$. As explained above, δ_w reduces for decreasing A or increasing $K_{1,eff}$. The width of a Néel wall is more complicated to derive and is discussed elsewhere [43].

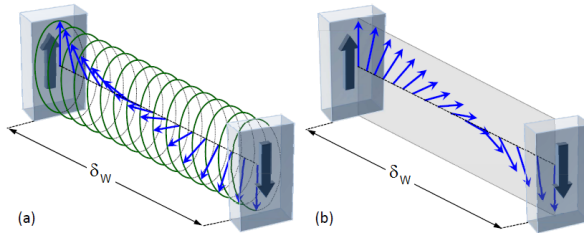


Figure 2.3: Illustrations of a Bloch (a) and Néel (b) wall [44].

Magnetic domains can occur in many different shapes and sizes, depending on the sample geometry, the external field, the film strain, the temperature and other parameters. Kooy and Enz developed a model for calculating the stray field energy of parallel aligned stripe domains (also called band domains) in an infinite plane with domain walls of zero thickness [73]. It is further assumed that the perpendicular anisotropy is large compared to the stray field energy. Based on this model, the size of the "up" and "down" domains $W_{u,d}$ was studied, when applying **out-of-plane** fields. The obtained results show a divergence of the domain period $d = W_u + W_d$ upon approaching saturation. For increasing out-of-plane field W_u increases, while W_d decreases. This process is reversible and does not change the overall pattern, if the external field is not exceeding a critical value. At this field W_d reaches a minimum and stays constant. Upon further increasing the external field, the "down" domains are irreversibly annihilated by expelling the domains beyond the sample boundaries, which results in a divergence of d [43]. At even larger fields the stripe domain pattern can break to segments and evolve to bubble patterns [74]. The increase of the domain period was also confirmed experimentally for FeGd alloys [72] and coupled systems of Co/Pt multilayers and FeMn [75] using resonant magnetic scattering.

The influence of **in-plane** fields on out-of-plane domains is also discussed in Ref. [43]. Based on micromagnetic equations, the equilibrium configuration of a homogenous stripe domain pattern can be calculated [76] and the obtained results are in agreement with the analytical model given by Marty *et al.* [77]. The following observations are relevant for the performed experiments presented in Chapter 3.

Depending on both the anisotropy energy density and the strength of the external field, a critical film thickness D_{cr} can be determined. For films thinner than D_{cr} the out-of-plane stripe domains are unstable and the magnetization is expected to lie in-plane, as presented in Ref. [67]. Furthermore, it has been simulated that an increasing in-plane field reduces the domain width, which was verified experimentally for FePd and FeGd alloys [77, 78]. The influence of in-plane fields acting on a stripe domain pattern is displayed in Fig. 2.4. When the external field increases, the domain size reduces and the domains arrange in a well ordered magnetic grating (a)-(c). When the field increases further, the contrast reduces, according to the rotation of the out-of-plane magnetization towards the film plane. For even larger fields, the order of the domain pattern reduces (d)-(f), as a consequence of the reduced dipolar interaction between the domains accompanying the magnetization tilt. This effect is also observed in the experiments, shown in Chapter 3.

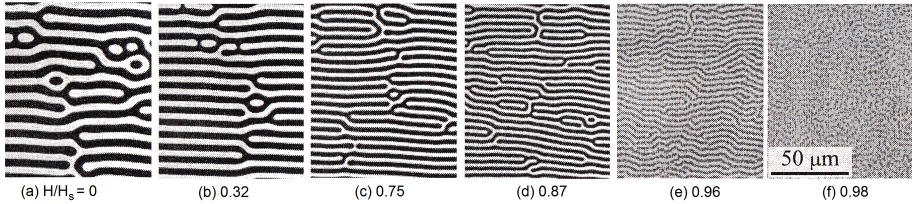


Figure 2.4: Calculated domain patterns for varying in-plane fields. The field strength is normalized to the saturation field H_s . For increasing fields the domain period decreases and the order among the domains improves (a-c). Upon reaching saturation, the domains are less ordered and the out-of-plane contrast decreases (d-f) [43].

2.2 Classical Description of Magneto-Optics

The interaction between light and condensed matter has been thoroughly investigated for decades and led to a large variety of applications, which are nowadays standard tools in solid state physics. A detailed overview, including the interaction of polarized X-rays and magnetism, can be found in Ref. [31], providing also the basis for this chapter. Further information can be found in literature [78–83].

Starting with a phenomenological description of optical effects, it is useful to introduce the complex refractive index $n(\omega)$, which is given by

$$n(\omega) = 1 - \delta(\omega) + i\beta(\omega). \quad (2.9)$$

An electromagnetic (EM) plane wave can be expressed by $\mathbf{E}_i = \mathbf{E}_0 \exp[-i(\omega t - \mathbf{k} \cdot \mathbf{z})]$, where ω is the frequency and k is the wave number, propagating in z -direction. When this wave is transmitted through a medium with the refractive index $n(\omega)$, the different phase velocity in the medium causes a phase shift by $\delta(\omega) k z$ and the amplitude \mathbf{E}_0 reduces by $\exp(\beta k z)$. Therefore, the real part $\delta(\omega)$ is linked to refraction and the imaginary part to absorption processes. The dependence of n on the frequency ω is known as dispersion. The refractive index is related to the relative dielectric tensor ϵ , where $\epsilon = \mathbf{1} + \chi$ and χ is the susceptibility tensor. For an isotropic medium, n is independent from the direction of the electric field vector and n is connected to ϵ via $n^2 = \epsilon$. For the non-isotropic case the polarization of the electric field is typically expressed by two certain orthogonal modes \mathbf{e}_m and the refractive index for these modes is related to the dielectric tensor by

$$n_m^2 = e_{m,i}^* e_{m,j} \epsilon_{i,j}, \quad (2.10)$$

where $m = 1, 2$ and $i, j = x, y, z$. Please note that Einstein's summation convention is used. According to classical electrodynamics, the interaction of a solid with an electromagnetic wave can be derived from Maxwell's equations

$$\begin{aligned} \operatorname{div}(\mathbf{B}) = 0 & \quad \operatorname{rot}(\mathbf{H}) = \mathbf{j} + \frac{\partial \mathbf{D}}{\partial t} \\ \operatorname{div}(\mathbf{D}) = \rho & \quad \operatorname{rot}(\mathbf{E}) = -\frac{\partial \mathbf{B}}{\partial t}, \end{aligned} \quad (2.11)$$

where \mathbf{E} denotes the electric field, \mathbf{D} the electric displacement, \mathbf{H} the magnetic field and \mathbf{B} the magnetic induction. In the following, the charge and current densities (ρ and \mathbf{j}) are

set to zero, corresponding to the absence of electric charges and currents. The quantities in equation 2.11 are related to each other by

$$\begin{aligned}\mathbf{D} &= \epsilon_0(\mathbf{E} + \mathbf{P}) \\ \mathbf{B} &= \mu_0(\mathbf{H} + \mathbf{M}),\end{aligned}$$

where ϵ_0 denotes the electric permittivity, μ_0 the magnetic permeability, \mathbf{M} the magnetization and \mathbf{P} the polarization. Furthermore, a static magnetization \mathbf{M} is assumed, which is reasonable for optical frequencies. This assumption implies that $\partial\mathbf{B}/\partial t$ equals $\mu_0\partial\mathbf{H}/\partial t$. The relation $\mathbf{D}(\omega) = \boldsymbol{\epsilon} \cdot \mathbf{E}(\omega)$ involves the relative dielectric tensor $\boldsymbol{\epsilon}$ and the Fourier transforms of $\mathbf{D}(t)$ and $\mathbf{E}(t)$. Using equation 2.11 with the assumptions above and $\mathbf{n} = \mathbf{k}c/\omega$, the Fresnel equation can be derived, which reads

$$[n^2\delta_{ik} - n_in_k - \epsilon_{ik}]E_k(\omega) = 0. \quad (2.12)$$

A non trivial solution demands

$$\det |n^2\delta_{ik} - n_in_k - \epsilon_{ik}| = 0. \quad (2.13)$$

With the resonant magnetic scattering experiment discussed in Chapter 3 the out-of-plane magnetization is probed in transmission. Therefore, a situation is considered, when both the magnetization and the wave vector point along the z-axis. In this case the dielectric tensor is given by

$$\boldsymbol{\epsilon} = \begin{pmatrix} \epsilon_{xx} & \epsilon_{xy} & 0 \\ -\epsilon_{xy} & \epsilon_{yy} & 0 \\ 0 & 0 & \epsilon_{zz} \end{pmatrix}. \quad (2.14)$$

Equations 2.13 and 2.14 yield

$$n_{\pm}^2 = \epsilon_{xx} \pm i\epsilon_{xy}. \quad (2.15)$$

Employing this result, equation 2.12 determines the corresponding electric field vectors \mathbf{E}_{\pm} , which can be expressed by

$$\mathbf{E}_{\pm}(\mathbf{r}, t) = \frac{1}{\sqrt{2}} E_o e^{i(n_{\pm}kz - \omega t)} \begin{pmatrix} 1 \\ \pm i \\ 0 \end{pmatrix} = E_o e^{i(n_{\pm}kz - \omega t)} \mathbf{e}_{\pm}. \quad (2.16)$$

When the magnetization and the wave vector are oriented in z-direction, the proper modes for the polarization vectors $\mathbf{e}_{1,2}$ in equation 2.10 are the polarization vectors of left and right circularly polarized light. Consequently, for this radiation the polarization state is not affected by the medium, but the light wave experiences a phase shift and a certain absorption, corresponding to $n_{\pm}^2 = \epsilon_{xx} \pm i\epsilon_{xy}$. For instance the absorption difference $\Delta\mu$ for left and right circularly polarized light can be approximated by

$$\Delta\mu = \text{Im} \{n_+ - n_-\} = \text{Im} \{ \sqrt{\epsilon_{xx} + i\epsilon_{xy}} - \sqrt{\epsilon_{xx} - i\epsilon_{xy}} \} \approx \text{Re} \left(\frac{\epsilon_{xy}}{\sqrt{\epsilon_{xx}}} \right)$$

This difference $\Delta\mu$ is typically measured in transmission spectroscopy employing X-ray magnetic circular dichroism (XMCD), either by inverting the helicity of the incident light or by reversing the magnetization with an external field.

It is remarkable that other magneto-optical effects, for instance polar, longitudinal and transverse magneto-optical Kerr effects (MOKE), are connected with the dielectric tensor in a very similar way [35]. These effects require that the off-diagonal elements of the dielectric tensor do not vanish, which can be understood in a classical picture. If the incident beam is linearly polarized in the x-direction (for the y-direction the discussion is equivalent), the electrons in the solid follow the electric field oscillation. The magnetic field accompanying the magnetization of the medium is oriented in z-direction and the Lorentz force acting on the oscillation electrons is parallel to $\mathbf{e}_x \times \mathbf{e}_z = -\mathbf{e}_y$. The Lorentz force causes an additional y-component in the electron motion, which in turn affects the emitted dipole radiation. Consequently a change of the light polarization is expected, which is expressed by the antisymmetric off-diagonal tensor elements.

Please note that for a correct description of the microscopic mechanisms causing the magneto-optical effects a quantum theoretical approach is necessary, which is included in the next chapter.

2.3 Resonant Magnetic Scattering

The excitation of a single electron by an EM wave $\mathbf{E}(\mathbf{r}, t) = \mathbf{E}_0 \exp[i(\omega t - \mathbf{k}_0 \mathbf{r})]$ results in a time-dependent electric dipole moment, which points in the direction of \mathbf{E} . The magnetic field $\mathbf{B}(t)$ of the EM wave causes a precession of the electron spin \mathbf{s} around an axis parallel to $\mathbf{B}(t)$. As illustrated in Fig. 2.5, the torque acting on \mathbf{s} changes its sign according to $\mathbf{B}(t)$, which results in an oscillation of the perpendicular spin component \mathbf{s}_d .

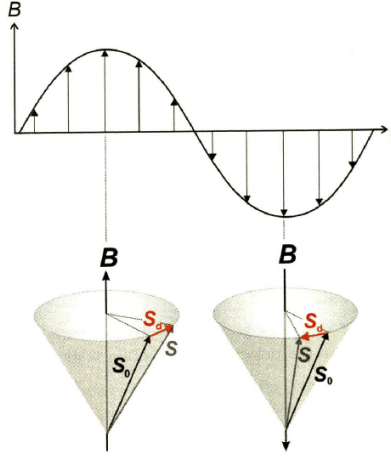


Figure 2.5: Precession of an electron spin \mathbf{s} , induced by a time-dependent magnetic field $\mathbf{B}(t)$. When the electron spin is expressed by $\mathbf{s} = \mathbf{s}_0 + \mathbf{s}_d$, the perpendicular component \mathbf{s}_d follows the oscillation of $\mathbf{B}(t)$ [31].

The induced electric and magnetic dipoles re-radiate spherically symmetric waves with the amplitude $e^{ik' r}/r$. For light scattering processes linked to the electron's charge and spin the following relations can be derived for the electric fields \mathbf{E}'_{charge} and \mathbf{E}'_{spin} :

$$\mathbf{E}'_{charge}(t) \sim [\mathbf{k}' \times \mathbf{E}(t)] \times \mathbf{k}' \quad \mathbf{E}'_{spin}(t) \sim [\mathbf{s} \times (\mathbf{k} \times \mathbf{E}(t))] \times \mathbf{k}',$$

where \mathbf{k} and \mathbf{k}' denote the wave vectors of the incident and scattered light. Two important conclusions can be drawn from this simple picture. First, charge scattering conserves the light polarization, while spin scattering results in a rotation of the polarization. Second, the charge and spin scattering cross-sections, σ_c and σ_s , are very different and they can be expressed by

$$\sigma_c = \frac{8\pi}{3} r_0^2 \quad \text{and} \quad \sigma_s = \frac{\sigma_c}{4} \left(\frac{\hbar\omega}{m_e c^2} \right)^2,$$

where r_0 is the classical electron radius and σ_c is the Thomson cross-section ($\sigma_c = 0.665 \text{ barn} = 0.665 \cdot 10^{-28} \text{ m}^2$). The spin scattering cross-section σ_s is a factor of $\frac{1}{4} \left(\frac{\hbar\omega}{m_e c^2} \right)^2$ smaller compared to the σ_c , where $m_e c^2$ is 511 keV. Thus, spin scattering in the XUV or soft X-ray regime (*i.e.*, $\hbar\omega < 10 \text{ keV}$) is orders of magnitudes less efficient than charge scattering.

Taking into account that an atom contains many electrons, which are distributed in the atomic volume with a specific electron density $\rho(\mathbf{r})$, it is useful to introduce the atomic form factor $f_0(\mathbf{Q})$ for a mathematical description of the scattering process within the first-order Born approximation. The scattering amplitude is given by the atomic form factor

$$f_0(\mathbf{Q}) = -\frac{1}{e} \int \rho(\mathbf{r}) e^{i\mathbf{Q}\cdot\mathbf{r}} d\mathbf{r}.$$

The intensity of the scattered light depends on the total scattering cross-section, which can be derived by integrating the differential atomic scattering cross-section $\frac{d\sigma}{d\Omega}$. For the non-resonant case the following relation has been found:

$$\left(\frac{d\sigma}{d\Omega} \right)_{atom} = r_0^2 |\mathbf{e} \cdot \mathbf{e}'| |f_0(\mathbf{Q})|^2, \quad (2.17)$$

where \mathbf{e} and \mathbf{e}' denote the polarization vectors of the incident and scattered light and $\mathbf{Q} = \mathbf{k} - \mathbf{k}'$ the momentum transfer vector. When λ becomes large relative to the atomic size, $\left(\frac{d\sigma}{d\Omega} \right)$ equals Z , which is the atomic number. The energy independent factor $f_0(\mathbf{Q})$ is also known as the Thomson charge scattering amplitude.

As the electrons are bound to an atomic Coulomb potential, it is necessary to modify the scattering amplitude by

$$f(\mathbf{Q}, \omega) = f_0(\mathbf{Q}) + f'(\omega) + i f''(\omega), \quad (2.18)$$

where $f'(\omega)$ and $f''(\omega)$ are the energy-dependent dispersive and absorptive contributions. Consequently, $[f_0(\mathbf{Q}) + f'(\omega)]$ is proportional to the real part of the refractive index $\delta(\omega)$ and $f''(\omega)$ is linked to the imaginary part $\beta(\omega)$.

Moreover, it is important to regard that the materials investigated contain an assembly of identical scattering objects. Thus, the scattered intensity $I(\mathbf{Q})$ is typically expressed by $I(\mathbf{Q}) = F(\mathbf{Q})^2 S(\mathbf{Q}) I_0$, where $F(\mathbf{Q})$ is the form factor, $S(\mathbf{Q})$ the structure factor and I_0 the intensity of the incident light. The form factor is the Fourier transform of the shape of the

object times its scattering amplitude and the structure factor accounts for the arrangement of the scattering objects. Hill and McMorrow included the polarization dependence by introducing a scattering tensor $\mathbf{F}(\mathbf{Q})$, which replaces the form factor and has the form of a 2×2 matrix, as shown in equation 2.24 [84].

Considering an one-dimensional ordered structure of N identical magnetic domains, the structure factor is given by the sum over the coordination positions of the domains, *i.e.*, $S(Q) = \sum_{k,l=1}^N e^{iQ(r_k - r_l)}$. Assuming that the magnetic domains arrange in a perfect periodic lattice with the domain period d , $S(Q)$ is given by

$$S(Q) = N\tau \sum_{n=-\infty}^{\infty} \delta(Q - n\tau), \quad (2.19)$$

where $\tau = 2\pi/d$. Thus, the structure factor samples the form factor of a single domain at integer multiples n of the inverse period τ . The number n is also known as diffraction order.

If the photon energy matches the energy difference between two electronic levels, the scattering amplitude is resonantly enhanced. In a quantum theoretical approach the time-dependent EM wave excites a transition from the initial state $|i\rangle$ to a final state $|f\rangle$ or involves intermediate states $|n\rangle$. These transitions are called first-order and second-order processes. The formalism developed by Dirac (for the first-order processes) [85] and by Kramers and Heisenberg (for the second-order processes) [86] leads to an expression for the transition probability per unit time T_{if} from the initial to the final state, known as *Fermi's golden rule* [87]. It is given by

$$T_{if} = \frac{2\pi}{\hbar} \left| \langle f | \mathcal{H}_{int} | i \rangle + \sum_n \frac{\langle f | \mathcal{H}_{int} | n \rangle \langle n | \mathcal{H}_{int} | i \rangle}{E_i - E_n} \right|^2 \delta(E_i - E_f) \rho(E_f), \quad (2.20)$$

where $|i\rangle$ and $|f\rangle$ denote the initial and final states and the corresponding energies are E_i and E_f . The second term is summed over all intermediate states $|n\rangle$. $\rho(E_f)$ is the density of final states per unit energy and \mathcal{H}_{int} is the interaction Hamilton operator, which reads

$$\mathcal{H}_{int} = \frac{e}{m_e} \mathbf{p} \cdot \mathbf{A}, \quad (2.21)$$

where \mathbf{p} is the momentum operator and \mathbf{A} the vector potential. The latter one is related to the electric field by $\mathbf{E} = -\frac{\partial \mathbf{A}}{\partial t}$. The differential scattering cross-section $\frac{d\sigma}{d\Omega}$ is proportional to the square of the scattering amplitude and it can be linked to the number of transitions per unit time into the solid angle $d\Omega$ by

$$\frac{d\sigma}{d\Omega} = \frac{T_{if}}{\Phi_0 d\Omega}, \quad (2.22)$$

where Φ_0 is the incident photon flux. Using the dipole approximation for the matrix elements $\langle a | \mathcal{H}_{int} | b \rangle$, the resonant contributions to the elastic-scattering amplitude can be derived. Hannon *et al.* calculated the resonant scattering amplitude f_{E1}^{res} [88], contributing to $f' + if''$. The resonant scattering terms are added to the non-resonant scattering amplitude f_0 and, thus, the total scattering amplitude $f_{E1} = f_{E1}^{res} + f_0$ is given by

$$f_{E1} = (\mathbf{e}'^* \cdot \mathbf{e}) f_c - i(\mathbf{e}'^* \times \mathbf{e}) \mathbf{m} f_{m1} + (\mathbf{e}'^* \cdot \mathbf{m})(\mathbf{e} \cdot \mathbf{m}) f_{m2}. \quad (2.23)$$

\mathbf{e} and \mathbf{e}' are the polarization vectors of the incident and scattered light, \mathbf{m} is the unit magnetization vector and $f_{c,m1,m2}$ are linear combinations of transition matrix elements, as described in equation 2.20. They can be decomposed into the radial transition matrix elements \mathcal{R} , defined by $\langle a | r | b \rangle$, and by Racah's spherical tensor operator, which is directly linked with the spherical harmonics $Y_{l,m}(\theta, \phi)$. The denominator of the factors $f_{c,m1,m2}$ is given by $(\hbar\omega - E_n + E_i + i\Gamma(n)/2)$. When the photon energy is equal to the energy difference between the initial and excited state, $|i\rangle$ and $|n\rangle$, the scattering amplitude increases significantly, according to the line width of the excited state $\Gamma(n)$.

The first term in equation 2.23 is independent from the magnetization \mathbf{m} and is therefore called charge scattering amplitude. It contains the non-resonant term (proportional to the atomic number Z) and a resonant contribution. The second term is linear in \mathbf{m} and accounts for *circular* magnetic dichroism. For linearly polarized light the magnetic scattering process causes a rotation of the polarization plane, which is reflected by $(\mathbf{e}'^* \times \mathbf{e})$. The last term is quadratic in magnetization and its polarization dependence is more complicated. It describes *linear* magnetic dichroism.

Equation 2.23 can be rewritten in the form of a Jones matrix, as mentioned above. This approach yields a relation for the scattered radiation field \mathbf{E}' , which is obtained by multiplying a 2-by-2 scattering matrix with the incident light field \mathbf{E} . A linear basis is used to divide the electric field vectors into their s- and p-polarization components. The matrix formalism is presented in equation 2.24, where the linear dichroism is neglected [89].

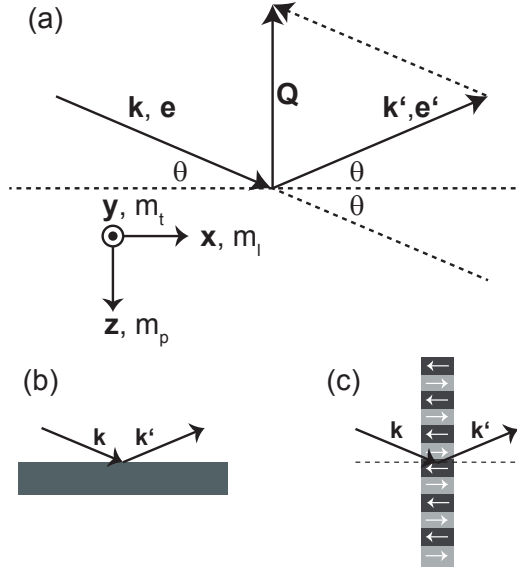


Figure 2.6: The general picture of the scattering process is depicted in (a), where \mathbf{k} and \mathbf{k}' are the incoming and scattered wave vectors, defining the scattering plane. \mathbf{e} and \mathbf{e}' are the corresponding polarization vectors and \mathbf{Q} equals $\mathbf{k}' - \mathbf{k}$. The coordinate system together with the longitudinal, transverse and polar components of the magnetization are indicated. (b) and (c) show the reflection and transmission geometry (for an out-of-plane domain pattern), respectively.

$$\begin{pmatrix} E'_s \\ E'_p \end{pmatrix} = \left[f_c \begin{pmatrix} 1 & 0 \\ 0 & \cos(2\theta) \end{pmatrix} - if_{m1} \begin{pmatrix} 0 & m_p \sin(\theta) + m_l \cos(\theta) \\ -m_p \sin(\theta) - m_l \cos(\theta) & m_t \sin(2\theta) \end{pmatrix} \right] \times \begin{pmatrix} E_s \\ E_p \end{pmatrix} \quad (2.24)$$

$m_{p,l,t}$ refers to the polar, longitudinal and transverse magnetization component and θ is the scattering angle, where 2θ is the angle between \mathbf{k} and \mathbf{k}' . An illustration of the scattering geometries is given in Fig.2.6, where the magnetization components follow the notation introduced in [89].

The first term in equation 2.24, proportional to the charge scattering amplitude, conserves the polarization state, but the p-component vanishes for $\theta = 45^\circ$, which is known as Brewster

effect. The second term changes the polarization state according to the magnetization. The p-to-s and s-to-p scattering channels are proportional to the projections of the polar and longitudinal magnetization onto \mathbf{k} . The p-to-p channel is determined by the transverse magnetization and there is no s-to-s scattering, as known from reflectivity measurements using the transverse magneto-optical Kerr effect (TMOKE). Consequently, the second matrix reflects the magneto-optical Faraday and Kerr effects, affecting the polarization and the intensity of the scattered light.

Equation 2.24 can be further approximated for the small angle scattering limit ($\theta \rightarrow 0$) [89], leading to the expression

$$\begin{pmatrix} E'_s \\ E'_p \end{pmatrix} = \begin{pmatrix} f_c & -im_l f_{m1} \\ im_l f_{m1} & f_c \end{pmatrix} \begin{pmatrix} E_s \\ E_p \end{pmatrix}. \quad (2.25)$$

Using this equation, it can be shown that the scattered intensity for left and right circularly polarized X-rays is given by

$$I_{\pm}(\mathbf{Q}) = f_c^* f_c S_{cc}(\mathbf{Q}) \pm 2 \operatorname{Re}[m_l f_c^* f_{m1}] S_{cm}(\mathbf{Q}) + m_l^2 f_{m1}^* f_{m1} S_{mm}(\mathbf{Q}), \quad (2.26)$$

where $S_{ij}(\mathbf{Q})$ are the partial structure factors. S_{mm} and S_{cc} account for spatial correlations of pure magnetic and pure charge origin, whereas S_{cm} includes a helicity dependent charge-magnetic cross term. This term cancels out for linearly polarized light, in agreement to other observations [90]. At this point it becomes clear that the scattered light intensity is proportional to m_l^2 , although the underlying magnetic dichroism depends linearly on the magnetization.

2.3.1 Related Experimental Findings

Investigations of CoPt multilayer films employing soft X-rays scattering at the L_2 resonance of Co showed a specific scattering pattern, where the magnetic scattering from an out-of-plane oriented domain pattern is compared with the charge scattering caused by the crystalline grain structure of the magnetic film [91]. A real space image of the magnetic domain pattern, obtained with transmission X-ray microscopy, is displayed in Fig.2.7(a). In this study charge density variations are distinguishable from the magnetic domain structure, as the corresponding structure factors have their maxima at different Q -values and both scattering processes show different energy dependencies.

In detail the magnetic structure is responsible for the peak at $Q = 0.04 \text{ nm}^{-1}$, while the charge density leads to the field-independent scattering signal at higher momentum transfer

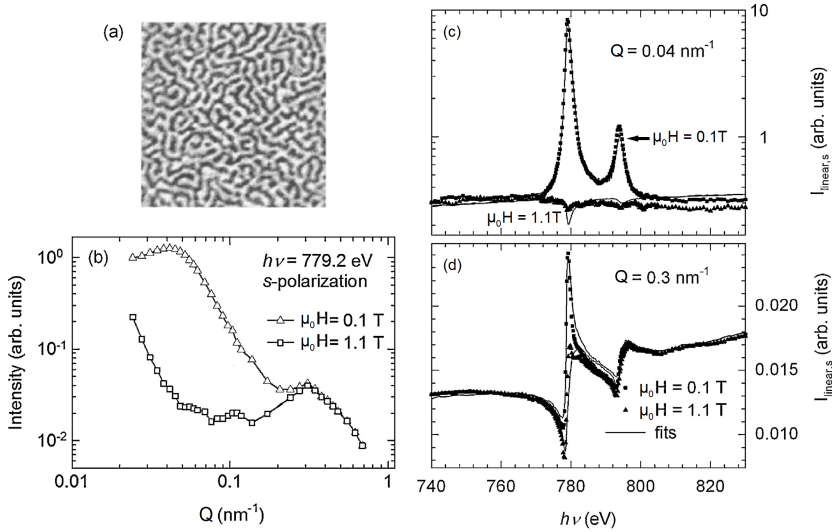


Figure 2.7: A transmission X-ray microscope image of the domain pattern of a Co/Pt multilayer film (a). The resulting scattered intensity is plotted against Q in (b). The data were recorded with linearly polarized photons of 779.2 eV (Co L_3 -edge) for an external field close to remanence ($\mu_0 H = 0.1$ T) and for saturating the film out-of-plane ($\mu_0 H = 1.1$ T). Energy dependencies of the scattered intensity for $Q = 0.04$ nm^{-1} and $Q = 0.3$ nm^{-1} are presented in (c) and (d), respectively. The fits are obtained from absorption measurements, as explained in the text [91].

vectors ($Q = 0.3$ nm^{-1}) [Fig.2.7(b)]. The energy dependency of the magnetic and charge scattering signal is studied in Figs.2.7(c) and (d). Close to remanence ($\mu_0 H = 0.1$ T) strong magnetic scattering is observable at the L_3 and L_2 edges (778 eV and 793 eV). Moreover, the scattering completely disappears, when the sample is saturated and all domains point into the same direction ($\mu_0 H = 1.1$ T) [Fig.2.7(c)]. The energy dependence of the charge scattering, observed at higher Q -values, shows a bipolar behavior at the resonance [Fig.2.7(d)], which is consequently well distinguishable from the magnetic scattering. For circularly polarized radiation it can be important to consider a charge-magnetic cross term for a correct modeling of the data, but for linear polarization this effect cancels out.

The solid lines in Figs.2.7(c) and (d) are fits, derived by measuring the energy dependence of the scattering amplitudes $f_{\pm} = f_c \pm f_{m1}$. The imaginary part of f_+ and f_- have been determined by absorption spectroscopy using circularly polarized light, while saturating the sample out-of-plane and switching the helicity. The real parts of f_+ and f_- have been

calculated by Kramers-Kronig transformation. The scattering data shown in Fig. 2.7 can be treated as the result of an equal illumination with left and right circularly polarized light. For modeling the measured RMS intensity, the scattering amplitude includes contributions of pure charge and pure magnetic origin. The good agreement between the scattering data and the fits demonstrates the possibility to interpret the scattering patterns regarding the electronic and magnetic contributions.

Peters *et al.* have conducted similar studies on out-of-plane oriented magnetic domains in FeGd alloys, where the XMCD contrast measured by absorption spectroscopy has been related to the scattering amplitude [92]. At the Gd $M_{4,5}$ -edges (1222 eV and 1190 eV) and Fe $L_{2,3}$ -edges (720 eV and 707 eV) an excellent agreement between the measured and calculated RMS intensity has been found. The corresponding measurement taken at the Fe resonances is plotted in Fig. 2.8(a).

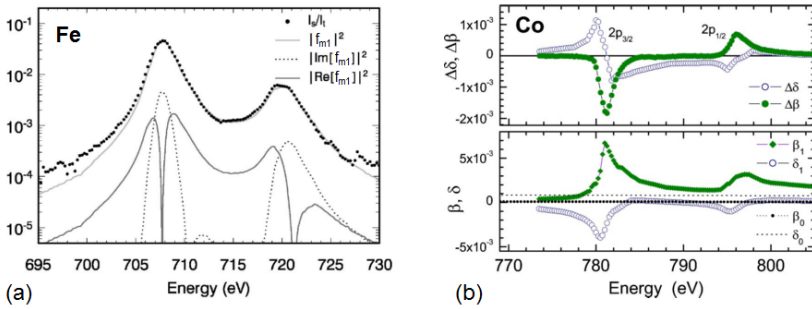


Figure 2.8: RMS measurements of an FeGd alloy at the Fe $L_{2,3}$ -edges are plotted in (a), thereby including a comparison of the squared scattering amplitude f_{m1} (soft gray line) with the scattered light intensity normalized to the transmitted intensity I_s/I_t (black points). The imaginary part of f_{m1} (dotted line) was obtained from XMCD measurements and the real part (dark gray line) was calculated using Kramer-Kronig transformation [92]. The energy dependent evolution of δ , $\Delta\delta$, β and $\Delta\beta$ close to the Co $L_{2,3}$ -edges is shown in (b) [93].

The intensity of the scattered light I_s is related to the magneto-optical constants by

$$\frac{I_s(\omega)}{I_t(\omega)} \sim (DE)^2 [\Delta\beta(\omega)^2 + \Delta\delta(\omega)^2], \quad (2.27)$$

where ω is the light frequency, I_t the helicity-averaged intensity of the transmitted light, D the sample thickness and $E = \hbar\omega$ the photon energy [92]. For left (-) and right (+) circularly polarized light the refractive index is given by

$$n_{\pm} = 1 - (\delta \pm \Delta\delta) + i(\beta \pm \Delta\beta), \quad (2.28)$$

where $\Delta\delta$ and $\Delta\beta$ are the so-called magneto-optical constants. They introduce a helicity dependent absorption and dispersion, which is proportional to the magnetization. Furthermore, the imaginary (real) part of the scattering amplitude f_{m1} is proportional to $\Delta\beta$ ($\Delta\delta$). In Fig. 2.8(a) the imaginary part of f_{m1} was determined by absorption measurements and the real part was calculated by Kramer-Kronig transformation, as described above. The squared sum of both parts follows very closely the data points, which were obtained by energy dependent scattering experiments. When the photon energy matches with the $L_{2,3}$ -edges of Fe, Co and Ni ($\hbar\omega_{res}$) the absorption is highest. At this energy β and $\Delta\beta$ show a maximum according to the resonant enhancement, while $\Delta\delta$ crosses zero. This is visible in Fig. 2.8(a) at the Fe $L_{2,3}$ -edges, where the imaginary part of f_{m1} peaks and the real part vanishes. Very similar energy dependent trends of δ , $\Delta\delta$, β and $\Delta\beta$ were observed for Co and Ni at the $L_{2,3}$ edges (see Fig. 2.8(b) and Refs. [32, 93]). The scattering data presented in Chapter 3 are measured on-resonance and thus the contribution of $\Delta\delta$ to the signal intensity is expected to be negligible. In this case the intensity of the scattered light is determined by $\Delta\beta$.

According to equation 2.27, the intensity of the scattered light depends quadratically on $\Delta\beta$ and $\Delta\delta$, which was also reported in other publications [94, 95]. Furthermore, the quadratic dependence on the film thickness and photon energy needs to be regarded, when magnetic films and alloys are compared at different elemental absorption edges by RMS.

Finally it is notable that the RMS patterns recorded with circularly polarized light are also influenced by the in-plane magnetization components [72]. The magnetic contrast is linked with the second order of scattering amplitude f_{m2} introduced in equation 2.23. The in-plane magnetization originates from the domain walls, surrounding one domain. When the "up" and "down" domains in the pattern are equally large, only odd diffraction orders are observed in the scattering pattern, as it is explained in Chapter 3. The distance between two walls is half of the domain period d , resulting in even diffraction orders. Consequently, the intensity ratio of the second and first diffraction order is proportional to $|f_{m2}|^2 / |f_{m1}|^2$ [92].

3 Coupled Domain Patterns studied with X-ray based RMS

3.1 Introduction

Resonant magnetic scattering (RMS), which means here small-angle X-ray scattering (SAXS) from magnetic domains in transmission, is a powerful technique to study the properties of magnetic structures due to several advantages. For extreme ultraviolet light and soft X-rays, the magnetic domain scattering amplitude is resonantly enhanced at the $M_{2,3}$ and $L_{2,3}$ absorption edges of the 3d ferromagnets, providing element contrast. The element selectivity allows the analysis of buried domain structures, which are inaccessible to magnetic force microscopy (MFM) and many other magnetic imaging techniques. Due to the high transmission of condensed matter in the soft X-ray spectral region relatively thick systems of 100 nm and more can be investigated, which is not given in surface sensitive imaging experiments like photo-emission electron microscopy (PEEM). Another advantage of RMS compared to electron-based magnetic imaging techniques, including Lorentz microscopy or scanning electron microscopy with polarization analysis (SEMPA), is the possibility to apply external fields during the measurement. Moreover, the main limitation of the spatial resolution is the X-ray wavelength, which is in the order of a few nanometers or less. In contrast to many real-space imaging techniques, the required exposure time for a reasonable magnetic contrast is small (\approx milliseconds to seconds). This benefit results from the simplicity of RMS, which does not require any additional optical element like a holography mask, a small frame (as it is used in lensless imaging) or a zone plate. The comparably short exposure time permits fast scans of the available parameters, which are the external field and the photon energy. Finally, RMS is very sensitive to small changes of the average arrangement of the magnetic domains, which can be difficult to observe in real-space microscopes with a limited field of view.

In this chapter, RMS is employed for the analysis of magnetic domains in thin films consisting of FePd and CoPd alloys, which exhibit out-of-plane oriented stripe domain patterns with different domain sizes. The magnetic-field-dependent behavior of these patterns is examined by applying external fields in-plane and out-of-plane. The interpretation of the RMS images explains several distinct characteristics related to the magnetic properties of the synthesized samples and the experimental data are additionally supported by micromagnetic simulations.

Furthermore, layered structures, including FePd/CoPd bilayers and CoPd/Pd/NiFe trilayers, are investigated by tuning the photon energy to the L_3 edges of the ferromagnetic 3d transition metals. RMS reveals the domain pattern of individual films within the coupled systems and it answers the question, how the domain pattern is affected by the magnetic coupling, which depends on the interplay of exchange and dipolar interactions as well as on the magnetic anisotropy.

For the FePd/CoPd bilayers the interaction between two adjacent out-of-plane domain patterns is investigated and the obtained results are compared with RMS patterns taken from the individual alloys. For the CoPd/Pd/NiFe trilayers, it is demonstrated that the out-of-plane domain pattern of the CoPd layer can be "projected" into the NiFe film, which is in-plane oriented, employing interlayer exchange interaction.

The presented study clearly reveals the capabilities of element-selective RMS that can be used to investigate many details of layered magnetic systems. As a consequence, the CoPd/FePd bilayer and CoPd/Pd/NiFe trilayer structures provide new options for future time-resolved surveys of ultrafast magnetization dynamics, as it is explained in the following for the individual samples. In general, a time-resolved RMS analysis of these specimens allows to study laser-induced changes of both the magnetic coupling and the domain size. Such effects could be examined with femtosecond precision, nanometer resolution and elemental contrast by RMS, if an ultrashort-pulse light source is employed, as it is discussed in Chapter 5.

Finally, magnetic dichroism at the Pd $M_{2,3}$ -edges is employed to image with RMS the magnetic structure of a CoPd alloy, which is presented for the first time to the best of my knowledge.

3.2 Sample Characterization

Ferromagnetic thin films were grown by molecular beam epitaxy (MBE) on top of polycrystalline, 50 nm thin Si_3N_4 membranes (provided by *Ted Pella, Inc.*), which are supported by

a rigid silicon frame with a $500 \times 500 \mu\text{m}^2$ large membrane window. The samples fabricated are listed in Table 3.1. All layers were grown at room temperature, apart from the FePd alloy, which was deposited at 500 K. As described in Chapter 2, the growth of 50:50 compositions of FePd films at similar temperatures yields the $L1_0$ ordered tetragonal structure, which gives rise to a uniaxial out-of-plane anisotropy related to the strong spin-orbit interaction, originating from the heavy 4d transition metal Pd [66, 68]. As the perpendicular anisotropy of CoPd alloys is a consequence of magnetostriction and an atomic short-range order [9], the desired out-of-plane anisotropy is already observable for room-temperature deposition. The ferromagnetic alloys are 40 nm thick to overcome the critical thickness for an out-of-plane anisotropy [67] and all samples are capped with 2 nm Pd or Al as protection against oxidation.

Table 3.1: Synthesized samples consisting of FePd and CoPd alloys, bilayers of both and trilayers with Permalloy.

Name	Composition (thicknesses in nm)
CoPd	Pd(2)/Co ₃₅ Pd ₆₅ (40)/Pd(2)
FePd	Fe ₅₀ Pd ₅₀ (40)/Pd(2)
FePd/CoPd	Fe ₅₀ Pd ₅₀ (40)/Co ₃₅ Pd ₆₅ (40)/Pd(2)
CoPd/Pd/NiFe	Pd(2)/Co ₃₅ Pd ₆₅ (40)/Pd(1)/Ni ₈₁ Fe ₁₉ (10)/Al(2)

Hysteresis loops of the synthesized samples, given in Fig. 3.1(a), have been recorded by employing the polar magneto-optical Kerr effect (PMOKE). More details regarding the experimental technique are given in section 4.2, but at this point it is important to mention that in the polar geometry the incidence angle of the laser beam is only a few degrees with respect to the surface normal and, thus, mainly the out-of-plane component of the magnetization is measured. As the penetration depth ($1/e$ decay) of the visible laser light ($\lambda = 375 \text{ nm}$) is about 12 nm (or less) for the metals investigated, mainly the top layer facing the laser beam is probed. These are CoPd and NiFe for the FePd/CoPd and CoPd/Pd/NiFe samples, respectively. Consequently, the measured hysteresis loops cannot give the full picture of the magnetic behavior, including all details about the magnetic anisotropy, but they certainly permit a first comparison. Instead of a rectangular hysteresis loop, a pronounced waist close to remanence is visible for all samples, resulting from domain nucleation and propagation of domain walls. Due to the formation of antiparallel oriented domains the remanence of the samples is small. The pure **CoPd** film shows the lowest saturation field of 330 mT and the **FePd** film the highest of 640 mT, as expected from

other studies of CoPd and FePd alloys [9, 66, 71]. In these publications, it has been shown that both the uniaxial anisotropy constant ($K_{FePd} \approx 1.5 \text{ MJ/m}^3$ and $K_{CoPd} \approx 0.9 \text{ MJ/m}^3$) and the saturation magnetization ($\mu_0 M_{s,FePd} \approx 1.5 \text{ T}$ and $\mu_0 M_{s,CoPd} \approx 0.8 \text{ T}$) are higher for the FePd alloy. This affects in turn the magnetic behavior of the material including the shape of the hysteresis loop and the saturation field. However, the magnetic properties, especially the magnetocrystalline anisotropy, strongly depend on the substrate, which can cause a canting of the easy axis of magnetization with respect to the surface normal. A canted easy axis, as reported for $\text{Fe}_{50}\text{Pd}_{50}$ alloys grown on $\text{MgO}(111)$, can lead to an increase of the saturation field [69]. The deposition of FePd films on top of polycrystalline Si_3N_4 substrates potentially results in similar effects.

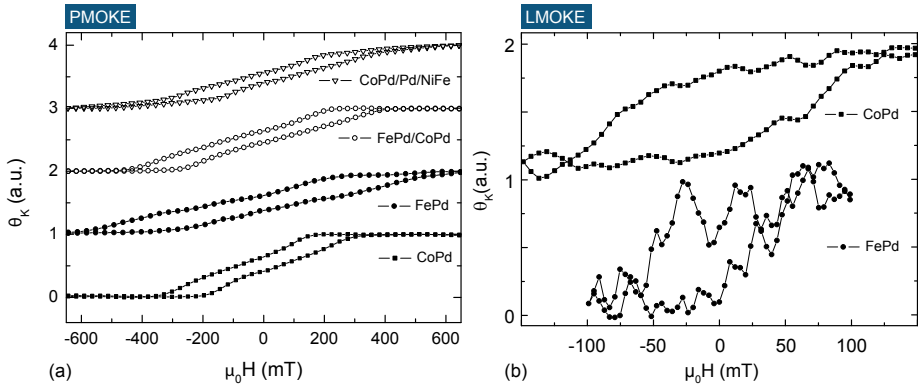


Figure 3.1: Hysteresis loops, measured with PMOKE (a) and LMOKE (b), for the different magnetic systems listed in Table 3.1. For the PMOKE (LMOKE) measurements the external field is applied out-of-plane (in-plane) and the incidence angle of the laser beam is about 1° (45°) with respect to the surface normal.

The **FePd/CoPd** bilayer reveals an intermediate saturation field of 460 mT, giving rise to two interesting questions: first, whether the domain pattern is affected by the coupling of the two magnetic films and, second, whether this coupling is influenced by the exposure with intense femtosecond laser pulses used in ultrafast demagnetization experiments. The first point is addressed in the following with resonant magnetic scattering using soft X-rays and the second issue is studied in Chapter 4 with femtosecond near-infrared laser pulses. If both films in the bilayer are ferromagnetically coupled, the decrease of the saturation field of FePd/CoPd bilayer (relative to the FePd film) is unexpected. A possible explanation of this effect may be exchange softening, which has been reported for exchange coupled

FePt/CoPt bilayers [96] or FeRh/FePt exchange spring films [97]. In these materials the softer magnet supports the switching process of the magnetically harder material, which reduces the saturation field.

In addition, the FePd easy axis could be canted, as mentioned above. In this case, the canting angle might be reduced due to the coupling to the CoPd layer and consequently the perpendicular switching process of the FePd/CoPd bilayer becomes easier. A possible canting of the easy axis is investigated in Fig. 3.1(b) by MOKE measurements in a longitudinal geometry (LMOKE). For these measurements the external field is oriented in-plane and the incidence angle of the laser beam is about 45° . The comparison of the FePd and CoPd films reveals for both materials an opening of the hysteresis loop, corresponding to the switching process of the in-plane magnetization component. Remarkably, the coercive fields of the FePd and CoPd films are about 50 mT and 120 mT, suggesting that the FePd can be switched easier in-plane due to a stronger tilt of the easy axis with respect to the surface normal.

The CoPd/Pd/NiFe trilayer shows an increase of the saturation field (440 mT) compared with the CoPd film (330 mT). This increase originates from the shape anisotropy of the NiFe film, favoring an in-plane orientation of the magnetization.

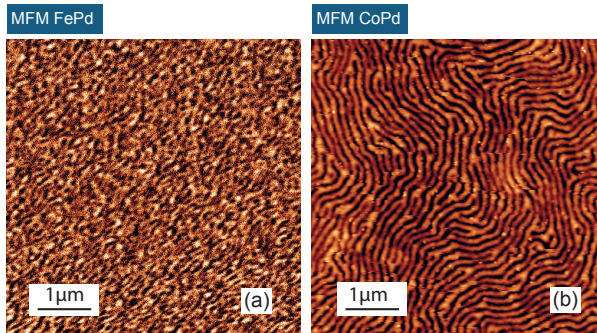


Figure 3.2: MFM images (phase contrast at 30 nm lift of the magnetic tip) for the FePd and CoPd sample are shown in (a) and (b), respectively.

Magnetic force microscope (MFM) images of the FePd and CoPd films are presented in Fig. 3.2. Both alloys, especially the CoPd specimen, show stripe domains thinner than 100 nm. The exact difference is determined below with RMS. Please not that the domain size depends on the magnetic history and is very different for random maze-like patterns and highly aligned striped domains. The influence of in-plane fields on out-of-plane oriented

domains is also analyzed in this chapter experimentally by RMS and theoretically by micromagnetic simulations.

3.3 Experimental Setup

The RMS data were measured at the beamline P04 of the synchrotron PETRA III (Deutsches Elektronen-Synchrotron (DESY), Hamburg, Germany), providing circularly polarized soft X-rays from an APPLE-II-type undulator [98]. The apparatus for the RMS measurements was designed at the University of Hamburg and includes vacuum chambers for mounting the required elements (pinhole, shutter, sample, beam block, CCD camera). All measurements were carried out in collaboration with the University of Hamburg (Institut für Angewandte Physik) and DESY (Coherent Imaging Group). A schematic drawing of the setup is given in Fig. 3.3. The X-ray beam is transmitted through an aperture (pinhole) with a diameter of $30\ \mu\text{m}$, cutting the beam profile to a circular spot. A fast beam shutter can be moved into the X-ray beam to adjust the exposure time and to avoid radiation damages of the detector. The thin-film sample is positioned with a six-axis piezo-driven stage (SmarPod, *SmarAct*) and the diffraction pattern is recorded by an in-vacuum charge coupled device (CCD) camera (1100S, *Spectral Instruments*, $15\times 15\ \mu\text{m}^2$ large pixels in a 4000×4000 array), placed 19 cm downstream of the sample.

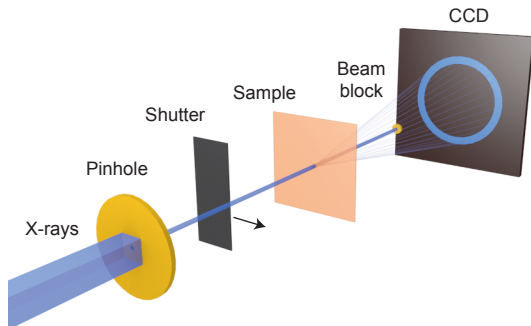


Figure 3.3: Schematics of the scattering setup. The X-ray beam is cut by a circular aperture ($30\ \mu\text{m}$ pinhole) and a shutter is employed to adjust the exposure time. The beam illuminates the transparent sample and the scattered light is measured with a CCD camera, while the direct beam is blocked.

Because the RMS signal is created by the scattered photons and the far more intense direct beam can easily saturate the camera, the non-scattered, direct beam is blocked by a metallic sphere, suspended by a thin tungsten wire. In-plane and out-of-plane external fields, up to 140 mT, are applied with four permanent magnets, mounted around the sample holder [99, 100]. The RMS images are integrations of 10–50 illuminations with short exposure times ranging from 15 ms to a few seconds, depending on the magnetic contrast of the investigated sample. It is important to note that the limit for the exposure time is given by the intensity of the light scattered by the magnetic domains and not by the direct beam, which is removed by the beam block.

A crucial parameter in RMS is the photon energy, which has to be tuned to the resonance edges of the specific elements and is determined by both the undulator and the monochromator. In order to optimize the beamline settings, the photon energy is varied while monitoring the intensity of the light transmitted through the sample with a photodiode. The scans are plotted in Fig. 3.4, where different samples are investigated at certain resonance edges. The energy-dependent transmission is in good agreement with the literature values of the $L_{2,3}$ -edges of Fe, Ni and Co. Moreover the Pd $M_{2,3}$ -edges are visible, although the corresponding transmission measurements suffer from a far lower signal-to-noise ratio. In general, the transmission scans allow the adjustment of the photon energy with high precision and any systematic deviation of the monochromator can be compensated.

In order to demonstrate the capabilities of the setup, a typical RMS pattern is given in Fig. 3.5, displaying in (a) the entire CCD sensor and in (b) the central region (indicated in (a) with a dashed box). In this measurement, 853 eV photons (Ni L_3 -edge) were scattered at the magnetic domains of a CoPd/Pd/NiFe trilayer, which is further examined in section 3.4.4. The full image (a) reveals an asymmetric ring occurring at the momentum transfer vector $Q = 0.59 \text{ nm}^{-1}$ [marked by an arrow Fig. 3.5(a)]. The scattering signal is associated with randomly distributed material grains, as explained below, and the asymmetry of the scattering image is related to the shape of the beam profile.

The point-like scattering in (b) occurs at $Q = 0.039 \text{ nm}^{-1}$ and is created by magnetic domains. As explained in the following, the scattering vector yields the dimensions of the scattering object, which is 81 nm for the magnetic scattering shown in (b) and about 5 nm for the scattering presented in (a). It can be easily verified that the large ring visible in (a) is of non-magnetic origin by shifting the photon energy away from the resonance edge or by saturating the sample during the X-ray exposure. For off-resonance measurements the magnetic scattering in (b) vanishes, while the larger ring in (a) remains unaffected.

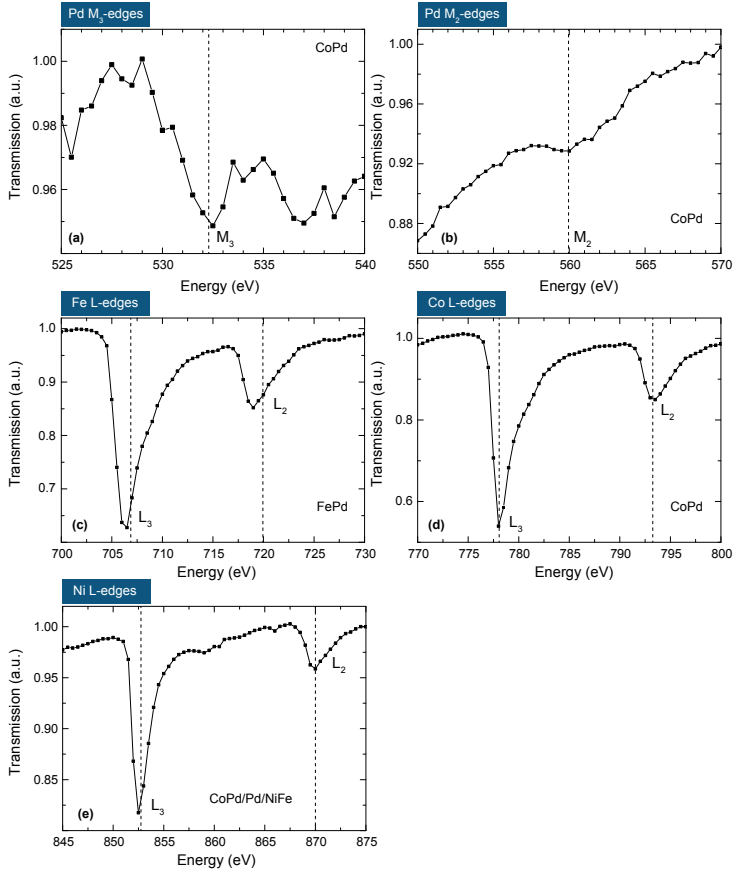


Figure 3.4: Transmission of the individual thin films as a function of the photon energy. The dashed lines mark the literature values of the Pd $M_{2,3}$ -edges and $L_{2,3}$ edges of Fe, Co and Ni.

Therefore, it is very likely that the scattering presented in Fig. 3.5(a) is produced by the polycrystalline structure of the film. The recorded images demonstrate that the CCD sensor covers a sufficiently large area in reciprocal space, but also smaller structures could be detected by decreasing the distance between sample and detector or by increasing the photon energy.

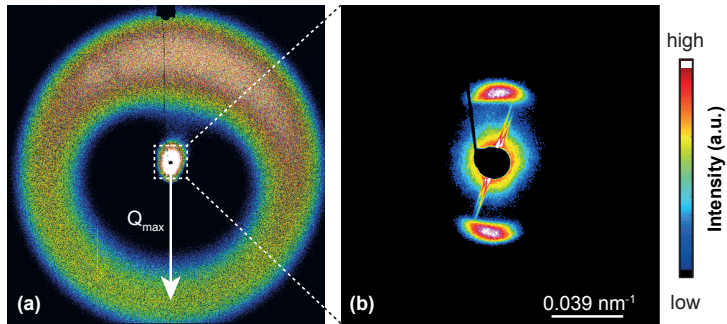


Figure 3.5: The RMS pattern of a CoPd/Pd/NiFe trilayer measured with a photon energy of 853 eV is plotted on a logarithmic intensity scale. The full CCD sensor is shown in (a), while the central part (marked with the dashed white box) is displayed in (b).

3.4 Results and Discussion

Figure 3.6 displays a typical scattering image of a CoPd sample obtained at the Co L_3 -edge. The figure illustrates the procedure to obtain radial integrations, which yield the Q -dependence of the scattered intensity. In the following mainly radially integrated RMS signals are studied for a quantitative comparison.

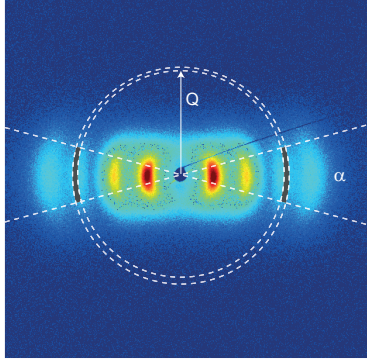


Figure 3.6: RMS patterns of a CoPd alloy with a schematic illustration of the radial integration. The transfer vector Q corresponds to a certain radius. Depending on the symmetry of the image, it is useful to constrain the integration by a cone with the opening angle α , which improves the signal-to-noise ratio. The step width of the integration consequently defines the area (indicated in dark gray), from which the light intensity is integrated and plotted against the corresponding Q -value to obtain the radially integrated signal.

Figure 3.7 shows an overview of the scattering data taken from three different layered magnetic samples (CoPd, FePd and FePd/CoPd). RMS images measured at the L_3 edges of Fe (707 eV) and Co (778 eV) are plotted for an FePd and a CoPd film in (a) and (b). For both materials, stripe domains generate a point-like scattering pattern. Randomly arranged domains, on the other hand, would create a scattering ring, as shown above in Fig. 3.5(a) for the non-magnetic scattering. For the FePd sample the scattering occurs at larger Q vectors, reflecting the different domain sizes in the two specimens. Q can be calculated by

$$Q = \frac{4\pi}{\lambda} \sin\left(\frac{1}{2} \arctan\left(\frac{r}{D}\right)\right), \quad (3.1)$$

where λ is the wavelength, r is radial distance to the transmitted beam and D is the distance between sample and detector. For the CoPd sample also higher diffraction orders are visible due to the high degree of order among the CoPd domains, which in turn increases

the scattering efficiency. The scattering images recorded at the Co resonance for the CoPd film and for the FePd/CoPd bilayer, *i.e.*, Fig. 3.7(b) and (c), are almost identical. For a detailed data analysis, radial integrations of the RMS patterns are presented in Fig 3.7(d). The maxima of the first diffraction orders for the FePd (black curve) and CoPd film (green curve) are located at $Q = 0.068 \text{ nm}^{-1}$ and $Q = 0.036 \text{ nm}^{-1}$. The average domain period, τ , is connected with Q by $\tau = 2\pi/Q$ and the domain size equals $\tau/2$, when the "up" and "down" domains have the same dimension. The analysis of the radial integration yields domain sizes of 46 nm and 87 nm for the FePd and CoPd samples.

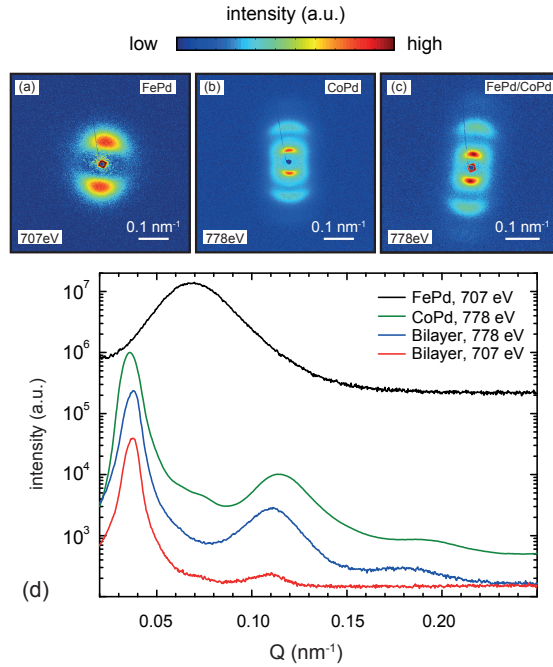


Figure 3.7: RMS patterns of an FePd film, a CoPd film and an FePd/CoPd bilayer, measured at remanence, are plotted on a logarithmic scale in (a), (b) and (c). As indicated in the plots, the photon energy is tuned to the L_3 edges of Fe (707 eV) and Co (778 eV). Radial integrations of the RMS patterns are shown in (d). The scattering data from the FePd and CoPd films (black and green curve) are multiplied with individual scaling factors and are shifted on the y-axis for a better comparison. The scattering curves from the bilayer measured at the L_3 edges of Co and Fe (blue and red curve) are on the same scale.

The equal size of the "up" and "down" domain causes a suppression of the even diffraction orders, which is known from a regular diffraction grating with a grating constant that is two times larger than the slit width. Thus, only odd diffraction orders are detectable in Fig. 3.7(d). The exact arrangement of the magnetic domains and consequently the details of the RMS pattern (including the visibility of even diffraction orders) depend on the external field and the magnetic history, as presented below.

The comparison of the RMS intensities recorded at the Co and Fe resonance for the CoPd and FePd films shows a far lower scattering efficiency for the FePd specimen, which is linked with the much larger relative width of the scattering peak as a consequence of the broader domain size distribution and the lower magnetic order of the FePd domains. In other words the CoPd film produces a higher RMS signal due to the better alignment of the stripe domains.

The scattering signals of the FePd/CoPd bilayer recorded at the Co and Fe edges (blue and red curves) reveal diffraction peaks at the same position, *i.e.*, $Q = 0.038 \text{ nm}^{-1}$ for the first order. The comparison of all scattering curves leads to the conclusion that the domain pattern in the FePd and CoPd layers of the FePd/CoPd bilayer are very similar, as a result of the magnetic coupling between both films. Moreover, the domain structure within the bilayer is dominated by the CoPd film, because the scattering curves measured for the CoPd sample coincide with the bilayer RMS signals [green and blue curve in Fig. 3.7(d)]. This important observation implies that the FePd domain structure adapts to the CoPd, which has been grown on top of the FePd film. If the magnetic anisotropy and the saturation magnetization are higher for FePd alloys, it may be surprising that the FePd magnetization mimics the CoPd domain pattern. However, the domain pattern of the FePd/CoPd bilayer is determined by the energy minimization of the entire system. In addition, a canted easy axis of the FePd layer may support the formation of the CoPd domain structure in the coupled FePd/CoPd bilayer.

For the FePd/CoPd bilayer, the ratio of the scattered light (integrated over the first diffraction order) at the Fe and Co resonance is $I_{Fe}/I_{Co} = 1/5 = 0.2$, which is far lower than expected, as explained in the following. The magneto-optical constants of Fe, Co and Ni at the L_3 edges are in the same order, but among the 3d ferromagnets Fe shows the highest magnetic contrast, because the atomic magnetic moment is largest for Fe [31, 32]. Thus, the higher magnetic contrast and the larger amount of Fe atoms in the $\text{Fe}_{50}\text{Pd}_{50}/\text{Co}_{35}\text{Pd}_{65}$ bilayer lead to the expectation that the RMS signal is stronger at the Fe resonance, as the arrangement of the magnetic domains is identical in both layers. As

discussed in Chapter 2, the RMS intensity depends quadratically on the atomic density and the magneto-optical constants. For the FePd/CoPd bilayer the ratio of the scattered light intensities at the Co and Fe edge can be calculated by equation 2.27. For an approximation, effective thicknesses of 20 nm and 14 nm are assumed for Fe and Co, according to the relative atomic concentrations. The magneto-optical constants $\Delta\beta$ and $\Delta\delta$ are taken from [32] and the ratio of the transmitted light intensity at the two edges is measured with a photodiode.

Thus, at the Fe and Co L₃-edges a relative intensity difference of 2.9 is expected. However, the measured intensity ratio is 0.2, which supports the assumption of a canted easy axis in the FePd film. A smaller out-of-plane component of magnetization in turn reduces the magnetic contrast and RMS intensity. The canting of the magnetization can be included in equation 2.27 by adding the factor $\cos^2(\alpha)$, where α is the angle between the magnetization and the surface normal. Assuming that the tilt of the CoPd easy axis is small, the comparison between the expected and observed intensity ratio yields a canting angle of approximately 75° for the FePd easy axis.

3.4.1 CoPd and FePd Films

The influence of external fields on CoPd domains is presented in Figure 3.8(a), showing several distinct effects that are visible in the radially integrated scattering pattern. As explained above, for $\mu_0 H = 0$ (black curve) the even diffraction orders are suppressed. When applying an external field of 150 mT out-of-plane (red curve), the "up" domains (oriented in field direction) are expected to grow, while the "down" domains reduce their size. This in turn changes the magnetic form factor and even diffraction orders show up. Figure 3.9 illustrates this effect for two transmission gratings, which have the same grating constant τ but different slit widths (b_1 and b_2). The position of the higher diffraction orders in reciprocal space is given by $Q_n = n \cdot G$, where $G = 2\pi/\tau$ denotes the reciprocal grating constant. The intensity of the diffracted light is determined by the form factor, which corresponds to the envelope curve shown in Fig. 3.9. The diffracted light intensity $I(\theta)$ can be easily derived by

$$I(\theta) = I_S \cdot \frac{\sin^2[\pi(b/\lambda)\sin(\theta)]}{[\pi(b/\lambda)\sin(\theta)]^2} \cdot \frac{\sin^2[N\pi(\tau/\lambda)\sin(\theta)]}{[\pi(\tau/\lambda)\sin(\theta)]^2}, \quad (3.2)$$

where θ is the diffraction angle, I_S the intensity of a single slit, b the slit width, λ the wavelength, N the number of illuminated slits and τ the grating constant [101]. As shown Fig. 3.9, the even diffraction orders are suppressed for $b_1 = 0.5\tau$. Strikingly, the even

diffraction orders are visible for $b_2 = 0.7\tau$, but also the intensity of the odd diffraction orders changes.

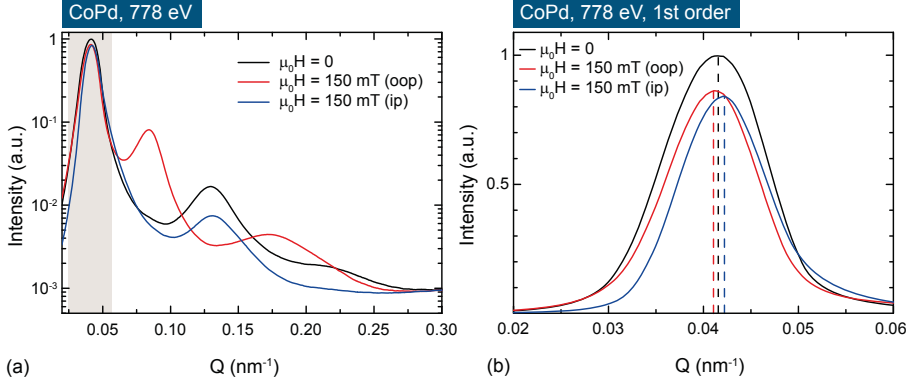


Figure 3.8: Radial integrations of the RMS patterns from a CoPd film are presented in (a). The black curve was taken at remanence ($\mu_0 H = 0$), while the red and blue curves were measured for an external field of 150 mT oriented out-of-plane (oop) and in-plane (ip). The photon energy is 778 eV (Co L_3 -edge) and the shaded area is magnified in (b). The external fields shift the scattering signal, as illustrated by the dashed lines.

For an in-plane field of 150 mT (blue curve) the scattered light intensity decreases as a consequence of the reduced magnetic contrast caused by a tilt of the magnetization towards the sample plane. The shaded area, marking the first diffraction order, in Fig. 3.8(a) is magnified on a linear intensity scale in (b). Please note that the reduction of the light intensity, observable for out-of-plane fields, is caused by the modification of the form factor, as described above. In addition, the external out-of-plane (in-plane) field shifts the scattering signal towards lower (higher) Q -values, leading to the conclusion that the out-of-plane field increases the domain period τ , while the in-plane field reduces τ .

As discussed in Chapter 2, the first point, *i.e.*, the increase of τ induced by **out-of-plane** fields, has been reported by C. Kooy and U. Enz [73]. Moreover, their findings have been confirmed in other experiments [72, 75]. In Ref. [72] the domain period increases significantly, when out-of-plane fields are applied. In particular, between remanence and saturation an domain expansion by a factor of 2 is reported. For the case presented here (Fig. 3.8) the out-of-plane field reaches about 45% of the saturation field and induces only very small modifications of the domain period. Hellwig *et al.* observed a field-independent domain period, which they related to crystalline grains, serving as pinning centers and prohibiting a

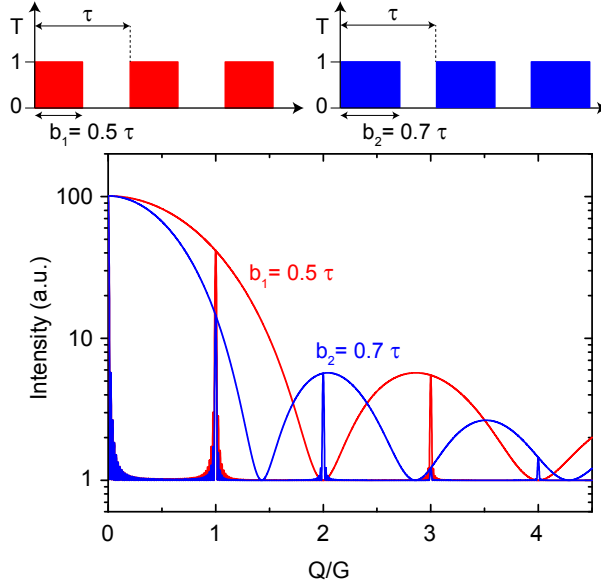


Figure 3.9: The sketches in the top part of the figure show two transmission gratings, which have the same grating constant τ but different slit widths (b_1 and b_2). The calculated diffracted light intensity is plotted against the normalized momentum transfer vector Q/G .

free domain expansion [6]. The polycrystalline structure of the here investigated specimen could act similarly on the magnetic domains, explaining the comparable small change of the domain period, which is in the order of 1%.

The second point, *i.e.*, the decrease of τ created by **in-plane** fields, is also described in Chapter 2 and is known from literature [43, 78]. For the CoPd film a small shift of the scattering pattern towards higher Q -vectors is visible [see Fig. 3.8(b)], corresponding to a domain size reduction by 1%. This effect is explained in more detail with experiments and simulations for an FePd film, which is affected stronger by in-plane fields.

Figure 3.10 shows the influence of external fields on FePd samples, exposing distinct differences compared to CoPd films. The RMS patterns were measured at the Fe L_3 -edge (707 eV), when external fields of 125 mT were subsequently applied out-of-plane (a), in-plane (b) and again out-of-plane (c). The orientation of the field is indicated in the right upper corner of the images. The domain walls align along the field lines, which causes the rotation of the scattering image (b). Moreover, the RMS intensity lowers, because the domains tilt

towards the in-plane direction. When the external field is oriented again out-of-plane (c), the intensity increases again, while the domain walls seem to remain in their field induced orientation.

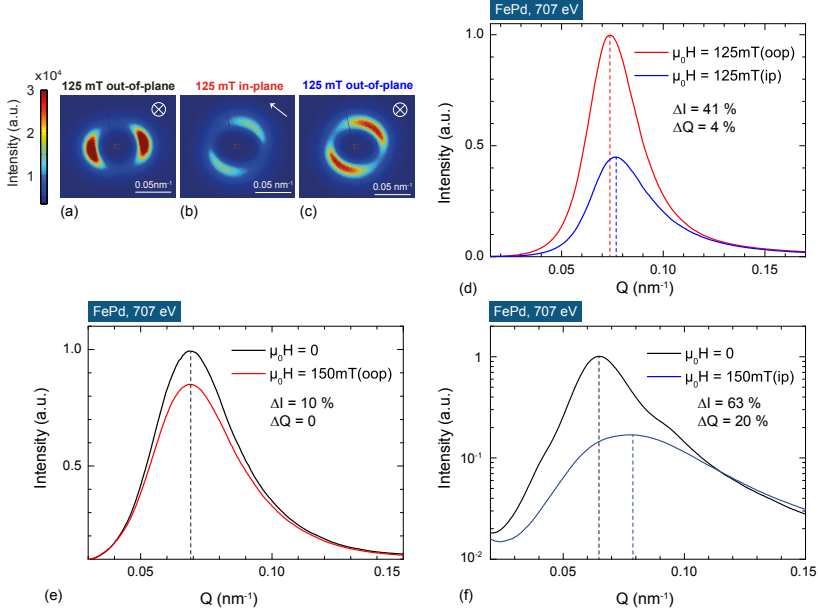


Figure 3.10: RMS images of the FePd sample taken at the Fe L_3 -edge (707 eV) are plotted on a linear scale in (a), (b) and (c). For these measurements the external field of 125 mT is subsequently applied out-of-plane (oop), in-plane (ip) and again out-of-plane. Radial integrations of (b) and (c) are plotted in (d). The influence of out-of-plane and in-plane fields of 150 mT is presented for identically grown FePd films in (e) and (f), where the dashed lines indicate the maximum of the scattering signal. The relative change of the total integrated RMS signal (ΔI) and momentum transfer vector (ΔQ) is included in the plots.

As mentioned above, the overall RMS intensity depends on the canting angle of the magnetization with respect to the surface normal and on the degree of order of the magnetic domains. The long-range order in a stripe-domain pattern is limited and can be expressed by a correlation length, which is given by the full-width at half maximum of the first diffraction order, ω . In Fig. 3.10(d) ω amounts to 0.0286 nm^{-1} at remanence. The corresponding value in real space, ϵ , is given by $2\pi/\omega$, which yields $\epsilon = 220 \text{ nm}$. Thus, ϵ is 2.6 times larger than the domain period ($\tau = 85 \text{ nm}$). The ratio of ϵ/τ is far higher for the CoPd domain

pattern ($\approx 6-7$), providing a higher scattering efficiency and therefore the observation of higher diffraction orders becomes feasible (as shown in Fig. 3.8). The different degree of order among the domains is also visible in the MFM images (Fig. 3.2), but RMS provides a simple and elegant way to quantify this difference.

In detail, the domain size and thus the position of the domain wall is affected by the external field, as it can be seen in the radial integrations shown in Fig. 3.10(d). The total intensity difference ΔI is 41 %, when 125 mT strong fields are applied out-of-plane and in-plane. Furthermore, the maximum of the scattering curve shifts by 4 % (ΔQ) towards higher Q -vectors.

The scattering signals measured at remanence and for $\mu_0 H = 150$ mT oriented out-of-plane (in-plane) are compared in Fig. 3.10(e) and (f). These measurements were taken for identically grown FePd films, which show almost identical domain patterns. This reflects the high reproducibility of the magnetic alloy in agreement with the high control of the MBE growth. For out-of-plane fields the intensity decreases by 10 % and no Q -shift is found [Fig. 3.10(e)]. On the other hand, the in-plane fields yield a pronounced drop of 63 % suggesting that the FePd magnetization can tilt easier towards the in-plane field [Fig. 3.10(f)]. The measurements also support the statement that the easy axis of magnetization is canted. According to the shift of the scattering peak in Fig. 3.10(f), the in-plane fields give rise to a domain "shrinking" by 20 %. As it is pointed out in Chapter 2, the reduction of the domain period is a consequence of the field-driven creation of new domain walls. This effect is unveiled in section 3.4.2 by micromagnetic simulations, exhibiting complex changes of the FePd domain pattern, when applying in-plane fields.

Moreover, the RMS peak shown in Fig. 3.10(f) broadens, resulting in a reduction of ϵ/τ , which drops from 2.3 (at $\mu_0 H = 0$) to 1.4 (at $\mu_0 H = 150$ mT). The increased width of the scattering signal suggests a broader domain size distribution. This is at the first glance surprising, as the in-plane fields orient the domain walls and consequently improves the alignment of the stripe domain. On the other hand, the canting of the domains towards the sample plane reduces the out-of-plane component and in turn the dipolar interaction between the stripe domain decreases, which causes a higher disorder of the magnetic domains (as described in Chapter 2).

3.4.2 Micromagnetic Simulations

To provide more details about the field-dependent evolution of the FePd domains, finite element micromagnetic simulations were employed to simulate the magnetic domain pattern of a 40 nm thin FePd disk with 1 μm in diameter, using the TetraMag code [102]. The simulations are based on the Landau-Lifshitz-Gilbert equation, which is numerically integrated with a strong Gilbert damping to obtain the domain pattern. The important material parameters used for the calculations are the exchange stiffness $A = 1.6 \cdot 10^{-11}$ J/m, the uniaxial anisotropy constant $K = 1.5 \cdot 10^6$ J/m³, and the saturation magnetization $\mu_0 M_s = 1.88$ T. These parameters are taken from literature [71] and may be different for the FePd alloys studied in the RMS experiment due to the growth on Si₃N₄ membranes. Especially, the simulations assume a perpendicular easy axis of magnetization, oriented parallel to the surface normal. Keeping these differences in mind, the evolution of the out-of-plane domain pattern inside an in-plane field is analyzed and compared with the experimental results.

The simulations are presented in Fig. 3.11. The surface normal of the FePd disk points in z-direction and the external field H is applied along the x-axis. Figures 3.11(a-d) show cuts parallel to the x-y plane through the middle of the film. With increasing magnetic field, the walls of the randomly arranged magnetic domains align along the external field lines, when increasing the field amplitude from 0 mT (a) to 0.35 mT (c). The domain pattern for $\mu_0 H = 1$ T (left half) is compared in (d) with the pattern, which develops after returning back to remanence (right half). Apparently, the in-plane field causes a reduction of the domain period τ , which can be extracted from line scans through the domain pattern (not shown). The average domain size is about 90 nm at remanence and 76 nm for $\mu_0 H = 1$ T. This change of the domain width matches very well with the experimental result reported in section 3.4.1, but the RMS measurements exhibit this decrease for a much smaller field strength of $\mu_0 H = 0.15$ T. This discrepancy could be explained by a canting of the easy axis, which is not regarded in the simulations. However, it is remarkably that experiment and simulation yield very similar values for the domain size, which also strongly depends on the chosen parameters. In addition, the effects described below seem to be a general phenomenon, as they are also visible in simulations using very different parameters ($A = 1.6 \cdot 10^{-11}$ J/m, $K = 0.2 \cdot 10^6$ J/m³, $\mu_0 M_s = 0.63$ T). For these parameters the out-of-plane domains are much larger, but very comparable modifications of the magnetic structure have been found for smaller external fields.

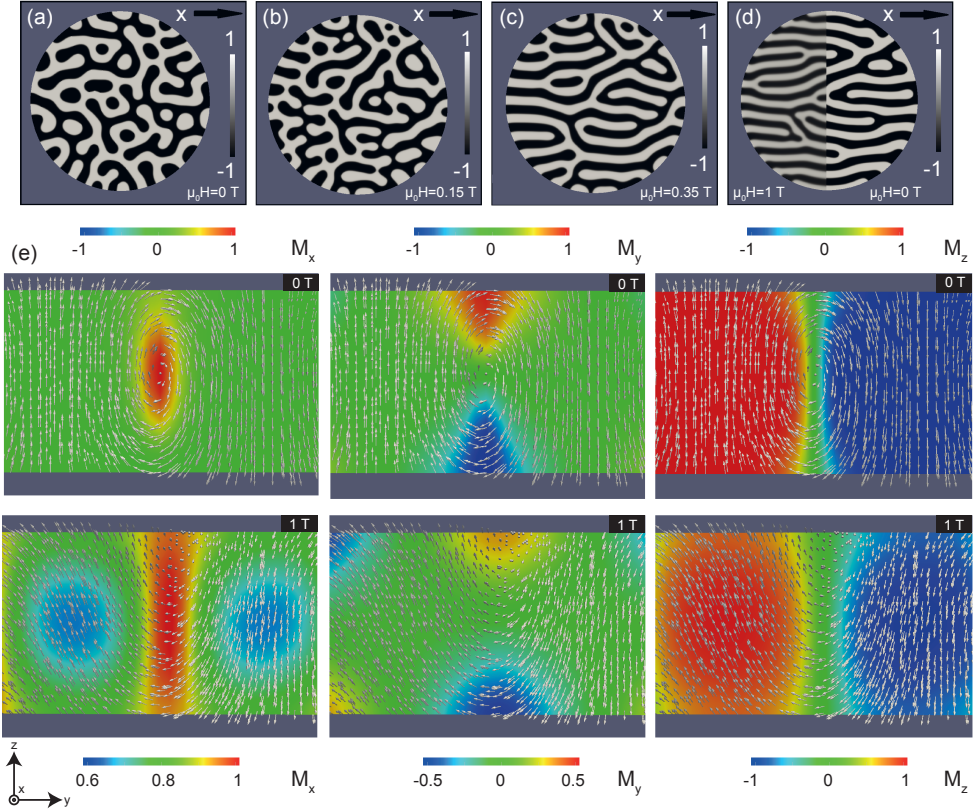


Figure 3.11: Results of micromagnetic simulations. The images shown in (a), (b) and (c) are cuts through the center of a 40 nm thin FePd disk with a diameter of $1 \mu\text{m}$ perpendicular to the surface normal, which points in z -direction. The gray levels correspond to M_z (normalized z -component of the magnetization) and the external field, $\mu_0 H$, is oriented in x -direction. The field strength is 0 T in (a), 0.15 T in (b) and 0.35 T in (c). In order to study the field dependence of the domain period, the domain structure induced by an in-plane field of 1 T [left half in (d)] is compared with the pattern which develops after returning to remanence (right half). (e) shows cross sections (along the y - z plane) and the M_x , M_y and M_z components are plotted from left to right. The upper row treats the case for $\mu_0 H = 0$ and the lower row for $\mu_0 H = 1$ T.

Figure 3.11(e) shows cross sections along the y - z plane of the 40 nm thick disk for $\mu_0 H = 0$ (upper row) and $\mu_0 H = 1$ T (lower row). The color corresponds to the normalized magnitude of M_x , M_y and M_z component (from left to right) and the arrows indicate the local magnetization vector. At remanence ($\mu_0 H = 0$) the magnetization displays a vortex at the domain wall, where the Bloch-type component is oriented along the x -direction (visible in the M_x component). Toward the film bottom and surface the domain walls are capped with Néel-type closure domains (visible in the M_y component).

For $\mu_0 H = 1$ T the x -component of magnetization, M_x , is always positive. This implies that all Bloch walls orient parallel to the field and the magnetization vectors within the domains tilt towards the x -axis. The magnetization (indicated by the arrows) changes from a flux closed structure at remanence to a more complex open pattern, where the magnetization is tilted and oscillates like a wave within the film.

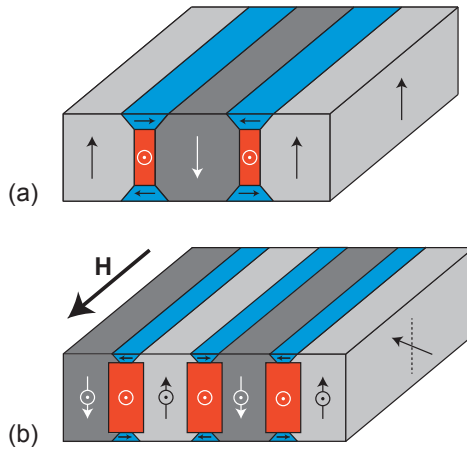


Figure 3.12: Schematic illustration of the domain pattern at remanence is shown in (a). The different domains are indicated in light and dark gray, while the Bloch walls are colored red and the closure domains blue. The influence of an external in-plane field \mathbf{H} is depicted in (b).

The mentioned reduction of the domain size is understandable, because the in-plane field aligns the magnetic moments along the field lines, which in turn reduces the Zeeman energy. This contribution to the total energy is even capable to compensate the required energy to form new domain walls, yielding a decrease of the domain period, while the domain walls broaden.

The field-induced changes of the magnetic domain pattern described above are summarized in Fig. 3.12. At remanence the "up" and "down" domain (light and dark gray) are separated by Bloch walls with flux closure domains (red and blue). The in-plane field \mathbf{H} leads to an increase of Bloch wall, while the contribution of the closure domain decreases. In addition, more domains are created and the magnetization vector within the domains tilts towards the field direction.

In conclusion, the micromagnetic simulations depict in detail, how the domains and the walls are affected by in-plane fields. Remarkably, the domain size and also the field-induced domain shrinking are in good agreement with the experimental results, although the observed effects occur at far higher fields in the simulations, emphasizing the role of the canted easy axis of the synthesized FePd film.

3.4.3 FePd/CoPd Bilayers

In Fig. 3.13 the influence of out-of-plane and in-plane external magnetic fields is studied for the FePd/CoPd bilayer system. The data have been recorded at the L_3 edge of Co (778 eV), yielding much more intense scattering images compared with the RMS signal taken at the Fe edge, as mentioned above. As explained for the CoPd specimen in section 3.4.1, even diffraction orders show up in the RMS pattern, when **out-of-plane fields** are applied [Fig. 3.13(a)]. At the same time the intensity of the odd orders reduces due to the changing form factor. The data show that the magnetic field dependence is very similar to the CoPd film, which is expected, because the CoPd layer determines the domain arrangement and the magnetic properties of the FePd/CoPd bilayer. However, applying in-plane fields results in a different response of the magnetic domains compared to the CoPd sample, as it is explained in the following.

The influence of **in-plane** fields is studied in Fig. 3.13(b). In this case, a shift of the RMS pattern, which may be very small, cannot be resolved. The total scattered intensity decreases for stronger fields due to tilt of the magnetization towards the in-plane field. The overall decrease of the RMS intensity reaches 50% for a field strength of 150 mT. For the pure CoPd and FePd alloy the corresponding decrease induced by in-plane fields is 25 % [Fig. 3.8(b)] and 63 % [Fig. 3.10(f)], respectively. Consequently, the magnetization tilt is largest for the FePd film and smallest for the CoPd film, while the FePd/CoPd bilayer exhibits an intermediate change in the scattering intensity. Furthermore, the relative

difference of the RMS intensity measured at the Co and Fe resonances is unaffected by the external field, suggesting that the magnetic coupling of the two layers is preserved. Based on the described results, one can conclude that the coupling between the FePd and CoPd supports the out-of-plane orientation of the FePd domains and therefore the influence of in-plane fields is less pronounced.

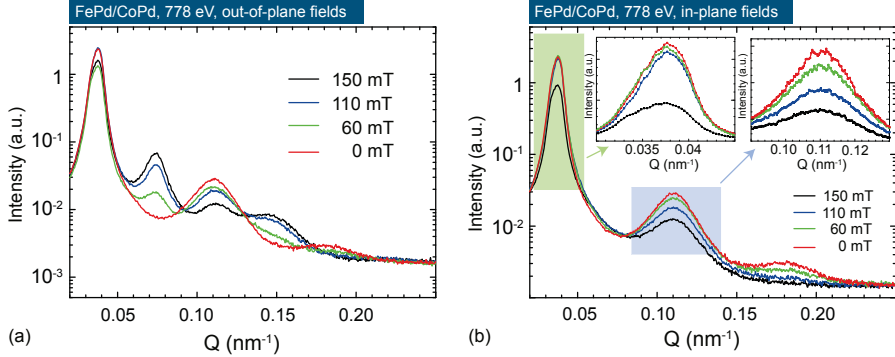


Figure 3.13: Radial integrations of the RMS patterns from the FePd/CoPd bilayer, while applying external fields out-of-plane (a) and in-plane (b). The photon energy is 778 eV, matching with L_3 edge of Co. The insets in (b) are magnifications with a linear intensity axis of the green and blue colored regions.

The insets of Fig. 3.13(b) display on a linear scale the first and third diffraction order, marked with the green and blue boxes. The first diffraction order reveals a sudden drop of the intensity at 150 mT, while the third diffraction order decreases continuously. As mentioned before, for increasing in-plane fields the Zeeman energy can overcome the magnetic anisotropy energy term and cause a significant tilt of the domains, reducing the total RMS intensity. The domain walls, on the other hand, orient along the field lines, which improves the order of the domain pattern and causes a higher scattering efficiency. Consequently, the third diffraction order reduces less than the first. Because this effect was not seen for stand-alone CoPd films, it may be the case that the canted easy axis of the FePd film supports the field-induced ordering of the stripe domains.

3.4.4 CoPd/Pd/NiFe Trilayers

Finally, RMS measurements of a CoPd/Pd/NiFe trilayer are presented, where in-plane oriented NiFe (Permalloy) is coupled through a Pd spacer to CoPd. As demonstrated below, this specimen reveals significantly different magnetic properties compared to the FePd/CoPd bilayer. An RMS pattern recorded at remanence for the Co L_3 -edge (778 eV) is plotted in Fig. 3.14(a). As expected, this pattern is very similar to the data taken from the CoPd film, shown in Fig. 3.7. The radial integrations normalized to the maximum intensities, including the RMS signals measured at the L_3 edges of Fe (707 eV) and Ni (852 eV), are shown in Fig. 3.14(b).

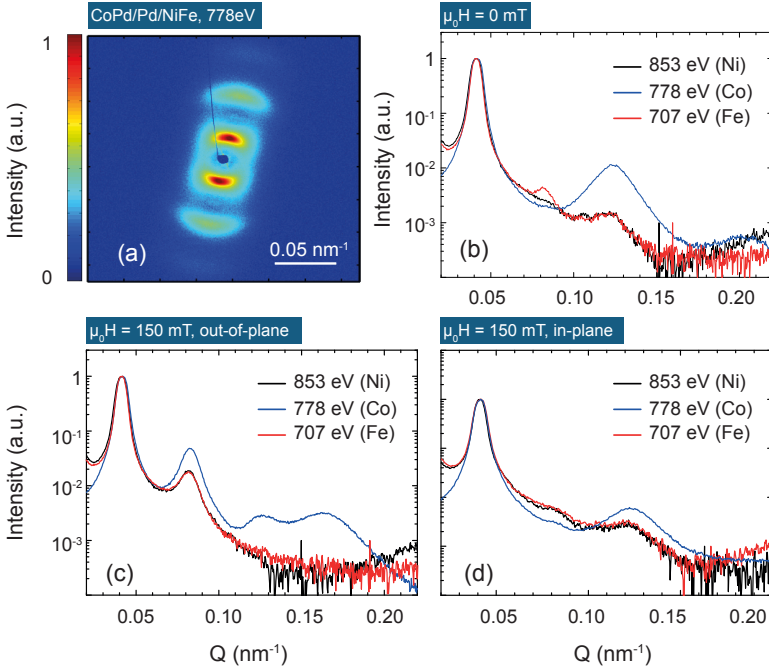


Figure 3.14: An RMS image taken from a CoPd/Pd/NiFe trilayer at the Co L_3 -edge (778 eV) is plotted on a logarithmic scale in (a). Normalized radially integrated RMS signal, recorded at remanence for the Fe, Co and Ni L_3 -edges (707 eV, 778 eV and 853 eV), are plotted in (b). (c) and (d) show the RMS signals, when applying 150 mT out-of-plane and in-plane.

Certainly, at all three resonances magnetic scattering is visible and the first diffraction order peaks at the same positions in reciprocal space ($Q \approx 0.041 \text{ nm}^{-1}$). Conclusively, the NiFe magnetization mimics the out-of-plane domain pattern of the CoPd layer, which is mediated by interlayer exchange coupling and the magnetic stray field of the CoPd film, as it is assumed for comparable sample systems [103, 104]. Moreover, the CoPd layer may magnetize the Pd spacer due to proximity effects, supporting a ferromagnetic coupling of the two magnetic layers [105].

The average domain period τ , extracted from the peak position of the first diffraction order, is 154 nm. The corresponding domain size is 77 nm under the assumption that "up" and "down" domains have the same width at remanence. The domain size agrees very well with the RMS and MFM images taken from the pure CoPd layer. Moreover, the correlation length ϵ amounts to 967 nm and the ratio of ϵ/τ is 6.3, which holds for all investigated resonances (red, blue and black curve). This underlines that the out-of-plane component of the NiFe layer almost perfectly adjusts to the CoPd domain pattern, although smaller differences between the two domain patterns are visible, when comparing the intensity of the higher diffraction orders (see Fig. 3.14). The differences are further discussed below.

The intensity of the first diffraction order measured at the Ni (Fe) L_3 -edge is 85 (170) times lower compared to the intensity obtained at the Co L_3 -edge. As shown above for the FePd/CoPd bilayer, the relative intensity difference can be approximated using equation 2.27. At the Fe and Ni edges a relative intensity difference I_{Fe}/I_{Ni} of 0.29 is expected. However, the measured intensity ratio is 0.5, which is slightly higher than the prediction. This discrepancy is potentially a consequence of disregarding $\Delta\delta$ for the magneto-optical contrast. For a small mismatch with resonance energy ($\sim 0.5 \text{ eV}$) also the dispersive part of the refractive index needs to be taken into account due to the bipolar behavior of $\Delta\delta$ at the resonance (see Fig. 2.8). In this case the highest expected contrast is about 0.45, which is very close to the experimental observation.

When comparing the RMS signals measured at the Ni and Co L_3 -edges a relative intensity difference between 0.039 and 0.053 is predicted. Please note that the exact value depends on the assumed magneto-optical constants. The measured intensity ratio I_{Fe}/I_{Co} is 0.0059, implying that the NiFe magnetization is tilted by $\approx 70^\circ$ with respect to the surface normal. Figure 3.15 illustrates this situation, where the domain pattern in the NiFe layer is strongly canted. The ratio I_{Ni}/I_{Co} yields comparable canting angles, confirming the experimental approach.

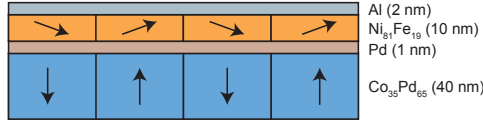


Figure 3.15: Schematics of a CoPd/Pd/NiFe trilayer. The magnetic coupling of the two magnetic layers results in a canted out-of-plane domain pattern within the NiFe film.

Another feature in Fig. 3.14 (b) is the absence of even diffraction orders at the Co edge, originating from the equal size of the "up" and "down" domains at remanence. On the contrary, the scattering curves measured at the Ni and Fe edges clearly show second diffraction orders. The smaller differences between the Fe and Ni scattering remain unclear, at this point. According to [72], in-plane components of the magnetization with half the periodicity of the domain pattern (τ), *i.e.*, the Bloch-type domain walls and the closure domains, can create even diffraction orders at remanence. The magnetic contrast provided by the domain walls emerges from the third term of equation 2.23, which is proportional to f_{m2} . A likely reason for the visibility of the even diffraction orders exclusively at the Ni and Fe edges, could be a stronger influence of these in-plane components with the periodicity $\tau/2$ for the canted domain pattern in the NiFe layer for which the out-of-plane magnetization is significantly reduced compared to the CoPd layer.

The magnetic field dependent behavior of the CoPd/Pd/NiFe trilayer is studied in Figs. 3.14 (c) and (d), which show the influence of out-of-plane and the in-plane fields with a strength of 150 mT. In general, the differences between the scattering curves recorded at the individual resonances are noticeable, but less pronounced compared to the scattering data recorded at remanence [Fig. 3.14(b)]. The positions of the diffraction orders are unaffected by the magnetic field strength and direction, as observed for the FePd/CoPd bilayer. For the out-of-plane field sweep even diffraction orders occur due to the different sizes of the "up" and "down" domains. This effect superimposes the second diffraction order observed at $\mu_0 H = 0$ for the Ni and Fe edges. Remarkably, the relative intensity difference of the scattered light at the different absorption edges remains almost constant for the applied out-of-plane fields. For in-plane fields of 150 mT, this relative difference changes significantly. At the Co resonance the scattered intensity decreases by 25%, whereas at the Ni and Fe resonances the intensity drops by 54%. A reasonable explanation is a stronger field-induced tilt of the NiFe magnetization, originating from the intrinsic in-plane anisotropy of Permalloy and a

weaker coupling of the CoPd and NiFe film compared with the FePd/CoPd bilayer, which did not show this behavior.

Conclusively, the angle between the magnetization vectors of the magnetic layers can be varied by applying an in-plane field (of 150 mT) for the CoPd/Pd/NiFe sample in contrast to the FePd/CoPd bilayer. Therefore, the CoPd/Pd/NiFe trilayer provides the possibility to manipulate the relative orientation of the two layers, without introducing a single domain state. The advantage of the FePd/CoPd bilayer is the larger RMS signal at the Fe L₃-edge. Nevertheless, the tuning possibility of the angle between two adjacent domain patterns gives further options to investigate ultrafast demagnetization in magnetic networks. In pump-probe experiments the canting angle could become a highly interesting parameter, for instance, when laser-induced superdiffusive spin currents, excited in the CoPd film, reach the NiFe layer. Recently published investigations of bilayers systems with non-collinear magnetization vectors demonstrated that ultrafast spin-transfer torques can be created by femtosecond laser pulses [30, 106], which may be observed as well in coupled domain patterns with a strong canting angle.

3.4.5 Resonant Magnetic Scattering at Pd M-Edges

Another option to investigate magnetism in CoPd alloys is provided by the chemical contrast of Pd. A first indication of the Pd M_{2,3}-edges was visible in transmission spectra, exhibiting a rather weak contrast at the Pd resonances (Fig. 3.4). However, the scattering images shown in Fig. 3.16(a) and (b) demonstrate the possibility to investigate domain patterns in magnetic alloys also at the Pd M-edges. The RMS pattern taken at the Co L₃-edge is plotted on a logarithmic scale in 3.16(c) and is apparently very similar to the RMS images recorded at the Pd resonances. Radial integrations of the Pd scattering patterns [Fig. 3.16(d)] reveal only little differences between the M₂ and M₃ edges, implying that at both photon energies the scattering efficiency is similar. It is remarkable that the overall intensity detected at the Pd edge is a factor of $2 \cdot 10^{-4}$ smaller relative to the Co signal. This is a significant diversity compared to the small intensity differences observed at the Co M-edge and Pd N-edge. RMS measurements of Co/Pd multilayer films conducted at the Co M_{2,3}-edges (60 eV) and Pd N₃-edges (51 eV) reveal a comparable scattering efficiency at the Co and Pd edges, depending on the exact composition of the multilayer [95].

The RMS results presented here agree with the pronounced differences of the XMCD contrast at the Co L₃- and Pd M_{2,3}-edges. The Co L₃-edge is known to cause huge XMCD asymmetries ($\approx 20\%$), whereas the Pd M_{2,3}-edges show a much smaller magnetic contrast ($\approx 0.1\%$) [107, 108], which is related to the low white line intensities at the Pd M-edges. On the other hand, the L_{2,3} resonances of Pd (3172 eV and 3330 eV) can yield a far better XMCD contrast [109], but these photon energies are not accessible with the used soft X-ray beamline, which is limited to 3 keV [98]. Measuring RMS patterns at the Pd M_{2,3}-edges consequently demands a very intense soft X-ray source and furthermore a high scattering efficiency of the magnetic specimen. For instance, no magnetic scattering at the Pd resonances was detected for FePd films, which is associated with the lower scattering efficiency.

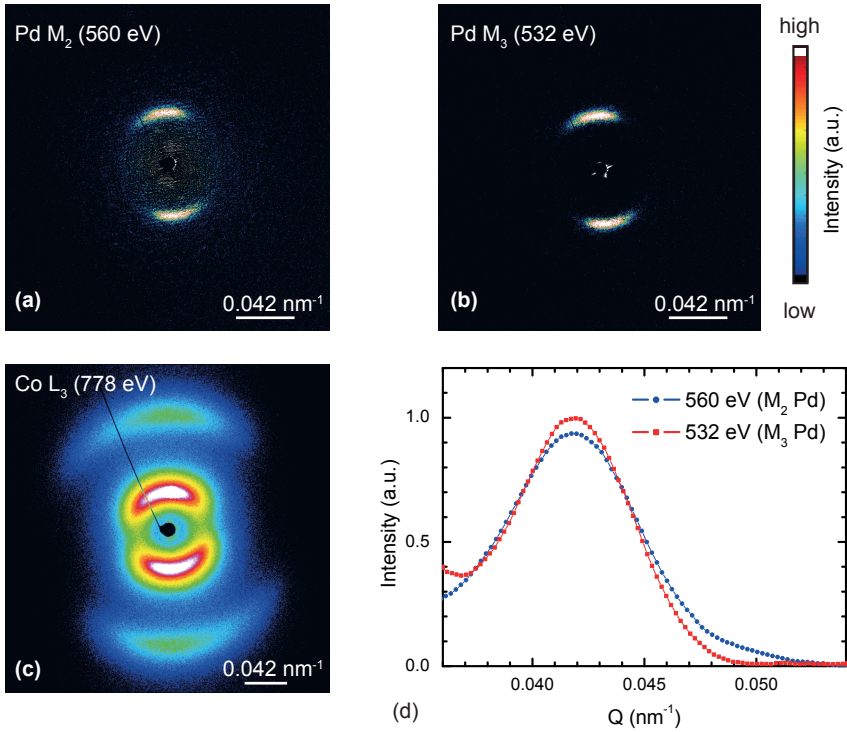


Figure 3.16: RMS patterns taken from a CoPd film at the Pd M_2 - and M_3 -edge (560 eV and 532 eV) are plotted on a linear scale in (a) and (b). For comparison the RMS image measured at the Co L_3 -edge is shown on a logarithmic scale in (c). Radial integrations of the Pd scattering data are presented in (d).

3.5 Conclusion

In conclusion, we have achieved to grow FePd and CoPd films on polycrystalline Si₃N₄-membranes with high quality regarding the magnetic properties. These alloys reveal very different domain sizes, providing the possibility to investigate the interaction between two adjacent domain patterns. For this study, small-angle X-ray scattering has been employed, which allows one to investigate the domain pattern of CoPd and FePd thin films and bilayers of both alloys with element selectivity. A comparison of the FePd/CoPd bilayer with the individual magnetic films demonstrates the dominating influence of the CoPd alloy in the coupled systems. Furthermore, the magnetic behavior has been analyzed by applying external fields up to 150 mT. For FePd films the field-induced tilt of the magnetization is strongest, which is related to a canted easy axis of magnetization. The impact of in-plane fields on out-of-plane oriented magnetic domains is further examined with micromagnetic simulations, which show a complex modification of the domain pattern and confirm the reduction of the domain width, as observed in the experiment. Additionally, the simulations reveal that the Bloch-type domain walls continuously grow, while the closure domains vanish.

The RMS analysis of coupled CoPd/Pd/NiFe trilayers points out the possibility to adjust the canting angle of the domain patterns in the two magnetic layers by applying in-plane fields. Finally, it has been demonstrated that X-ray scattering is capable to investigate magnetic domains using the magnetic dichroism at Pd M_{2,3}-edges.

The static element-selective resonant magnetic scattering results provide deep insights into the magnetic properties of coupled magnetic thin-films and form the basis for time resolved RMS experiments on these structures. Therefore, the investigated FePd/CoPd bilayers and CoPd/Pd/NiFe trilayers are promising candidates to elucidate the role of superdiffusive spin currents generated by ultrashort laser pulses [25, 27]. The temporal evolution of the magnetization of the FePd/CoPd bilayer is studied in the next chapter using visible laser pulses.

4 Ultrafast Magnetization Dynamics in FePd/CoPd Bilayers

4.1 Introduction

The interaction of photons and condensed matter was described in section 2.2, showing the feasibility to probe magnetism with photons. Beaurepaire *et al.* demonstrated the inverse process, *i.e.*, the ultrafast manipulation of magnetism with photons, employing femtosecond laser pulses [22]. Following this key experiment an impressive amount of experiments presented new facets of ultrafast magnetization dynamics. On this background many theoretical models have been developed to explain the experimental findings. They include phenomenological approaches like the three-temperature model [22, 110] and atomistic spin models based on Landau-Lifshitz-Gilbert [111] or Landau-Lifshitz-Bloch equations [112]. For a microscopic picture several models have been proposed, which could potentially contribute to the ultrafast magnetization dynamics. These models involve the Zang-Hübner model [113], coherent spin-photon coupling [114], spin-flip scattering of electrons on phonons [21] or magnons [115] and superdiffusive spin transport [26]. Detailed explanations of these models can be found elsewhere [116, 117].

This chapter focuses on the FePd/CoPd bilayer, which have been introduced in Chapter 3. The survey presented here investigates the influence of ultrafast laser-induced demagnetization on the magnetic coupling of the two layers. Moreover, studies of Au/CoPd samples reveal the role of hot electrons, which are excited by the pump laser in the Au layer and influence the demagnetization process of the CoPd layer. Please note that the time-resolved measurements were conducted with femtosecond laser pulses in the near infrared to visible region of the electromagnetic spectrum.

As it has been mentioned in Chapter 3, a very helpful approach to understand laser-induced magnetization dynamics in more detail is the design of suitable structures. For instance,

layered magnetic systems have been used to highlight certain mechanisms contributing to the demagnetization process. This includes, for example, systems of ferromagnetic and non-magnetic materials, as well as metals or insulators [24, 25, 28, 38, 118]. Two published results are of particular interest for the laser-induced demagnetization of the synthesized FePd/CoPd bilayers. One is the finding that the exchange coupling between FePt and CoPt layers, grown on top of each other, can be manipulated on ultrafast timescales [96]. Hysteresis loops, probed before the arrival of the pump pulse (zero delay) and 1 ps after zero delay, are shown in Figs. 4.1(a) and (b). The laser pumping causes besides demagnetization a decoupling of the magnetic layers, which results in the two steps of the hysteresis loop in (b).

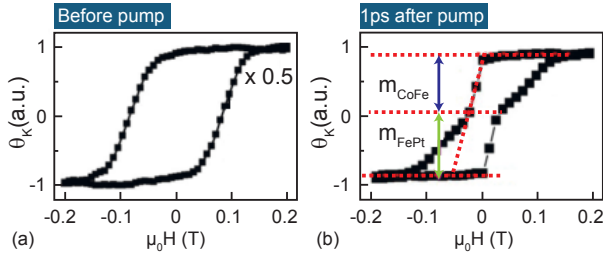


Figure 4.1: Hysteresis loops of an FePt(6 nm)/CoFe(2 nm) bilayer taken for different delays between pump and probe pulses. At zero delay the pump pulse (2 mJ/cm^2) quenches the magnetization and decouples both magnetic layers, which causes an individual switching of both layers. This decoupling manifests in a two-step hysteresis loop visible for a delay of 1 ps (b). The individual switching steps are indicated by m_{CoFe} and m_{FePt} . Adapted from [96].

The second result considers the generation of superdiffusive spin currents for the understanding of ultrafast magnetization dynamics. When studying Fe/Ru/Ni-trilayers, laser-induced spin currents excited in the Ni layer can result in a magnetization enhancement of the Fe layer [25]. In addition, spin transport, based on the excitation of non-equilibrium electrons, can explain the demagnetization of a Ni film, protected against the direct laser illumination with a thick Au layer. According to the interpretation given in [28], the Au layer absorbs the laser energy, which results in a current of hot electrons. When entering the Ni film, minority and majority spins have different transport properties, because spin-majority electrons scatter much less, which is connected to the spin-dependent density of states in Ni. The spin-minority electrons get trapped at the Au/Ni-interface, while the spin-majority electrons reach the substrate (Al foil), resulting in a decrease of the Ni magnetization.

Moreover, spin-filtering effects at the Au/Ni-interface may be taken into account to explain the laser-induced demagnetization. The obtained results underline the importance of spin transport in femtosecond magnetization dynamics and it seems to be evident that a direct interaction with the laser field is not necessary for a quenching of the magnetization.

Therefore, it may be important to consider spin transport effects also for the FePd/CoPd bilayer, because the typical penetration depth of infrared and visible light in metals is about 10–15 nm and the CoPd film, covering the FePd, is 40 nm thick. This implies that a fraction of more than 90 % of the laser light is absorbed in the CoPd film, which is directly excited by the pump laser.

4.2 Experimental Setup

The temporal evolution of the magnetization in FePd/CoPd bilayers is studied with a pump-probe setup, using near infrared (≈ 800 nm) pump and visible (≈ 400 nm) probe pulses created with an ultrashort-pulse laser amplifier (Spitfire, *Spectra Physics*). The probe beam measures the out-of-plane component of magnetization by employing the polar magneto-optical Kerr effect (PMOKE). A simplified drawing of the pump-probe scheme is given in Fig. 4.2. During the measurement the specimen is saturated by an external field, which is applied perpendicular to the sample surface. The PMOKE signal is proportional to the rotation of the polarization plane of the probe beam, which is reflected at the CoPd layer.

As mentioned above, due to the penetration depth of the laser light, mainly the top layer (CoPd) is pumped and probed. The delay of the pump and probe pulses can be adjusted by changing the optical path with a moveable mirror pair, which is often called delay stage. The incident angle of both pump and probe beam is only a few degrees with respect to the surface normal, providing highest contrast for the out-of-plane component of magnetization and minimal temporal smearing, which limits the temporal resolution of the measurements for a pronounced angle between pump and probe beam. The duration of the laser pulses is determined using auto- and cross-correlation techniques, yielding a pulse duration of 70 fs for the pump pulses and 90 fs for the probe pulses. A detailed description of the setup is given in Ref. [119].

Figure 4.3 shows hysteresis loops of a CoPd film and an FePd/CoPd bilayer, which were already presented in section 3.2. For these measurements a pulsed diode laser with repetition rate of 40 MHz and a wavelength of 375 nm (LDH-P-C-375, *PicoQuant*) was used. The

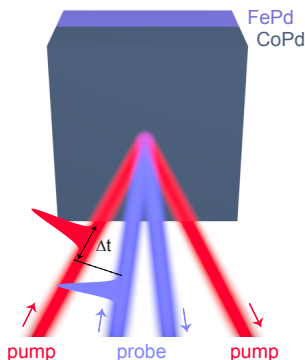


Figure 4.2: Schematic drawing of the time-resolved PMOKE measurement. For sake of simplicity, only the magnetic layers of the sample are shown and the angles of the pump and probe beam with respect to the surface normal are exaggerated. The delay between the pump and probe pulse, Δt , can be adjusted with a delay stage. The outgoing probe pulses are guided to a detector, which is sensitive to polarization changes of the light.

laser beam is additionally modulated with a frequency of 1 kHz by a chopper wheel for lock-in amplification.

The polarization rotation, corresponding to the Kerr angle, is detected by splitting the laser field with a Wollaston prism into two orthogonal polarization components, which are measured with a balanced photodiode bridge. The difference of the photodiode voltages is amplified using the lock-in technique. As mentioned above, the reference frequency of the lock-in amplifier is the modulation frequency of the chopper wheel, but the repetition rate of the diode laser (40 MHz) is much higher than the repetition rate of the laser amplifier system (1 kHz), used for the time-resolved measurements. The resulting signal-to-noise ratio is thus far better for the high frequency diode laser, as a consequence of the larger number of laser pulses averaged during the integration time of the lock-in amplifier. For time-resolved and static measurements the difference of the photo diode signals is divided by the sum of both signals, measured at the same time with a second lock-in amplifier, in order to normalize to the laser intensity.

As mentioned in Chapter 3, the saturation field clearly increases from 330 mT for the CoPd sample to 460 mT for the FePd/CoPd bilayer, which is indicated by the dashed vertical lines in Fig.4.3. The following time-resolved measurements study, whether decoupling

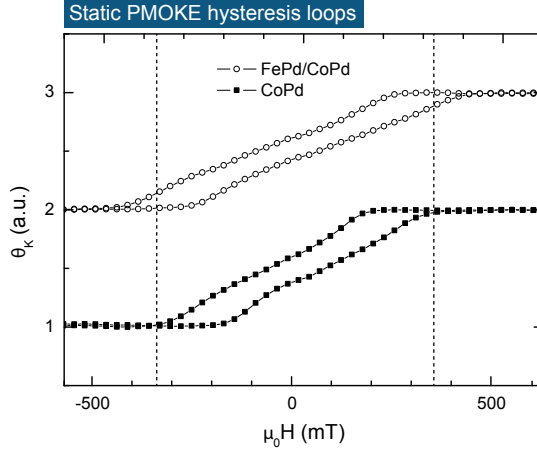


Figure 4.3: PMOKE hysteresis loops of $\text{Co}_{35}\text{Pd}_{65}$ (40 nm) and $\text{Fe}_{50}\text{Pd}_{50}$ (40 nm)/ $\text{Co}_{35}\text{Pd}_{65}$ (40 nm) films measured with a pulsed diode laser ($\lambda = 375$ nm). The vertical dashed lines mark the saturation field of the CoPd sample.

effects, as observed for FePt/CoFe bilayers (Fig. 4.1), occur for the FePd/CoPd specimen. In order to reach the highest magnetic signal, the sample is saturated during the delay scans by applying an out-of-plane field of 500 mT. Subsequently, the direction of the external field is inverted and the delay scan is repeated, resulting in a mirrored demagnetization curve. Subtracting both scans from each other removes any non-magnetic background and, thus, the difference signal is proportional to the laser-induced change of the saturation magnetization.

4.3 Results and Discussion

Figure 4.4(a) shows a time-resolved PMOKE signal of the FePd/CoPd bilayer for a pump fluence of 2 mJ/cm^{-2} . The measured Kerr angle Θ_K is plotted against the delay between the pump and probe pulses. The curve is normalized to the signal before zero delay and the data point density has been chosen higher within the first picoseconds next to the point of zero delay. As it has been observed in many other experiments, the magnetization quenches (by 40 %) on the femtosecond scale, while the following recovery of the magnetization happens on the picosecond scale.

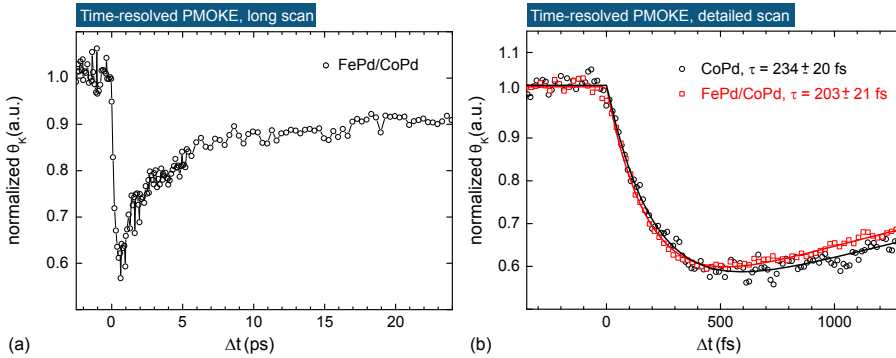


Figure 4.4: Time-resolved PMOKE signal of an FePd/CoPd bilayer for a pump fluence of 2 mJ/cm^2 (a). At the point of zero delay a sharp drop of the magnetization by 40% is visible, followed by a far slower recovery. The data point density is higher close to the point of zero delay. The initial femtosecond quenching of the magnetization for the CoPd film and the FePd/CoPd bilayer is studied within the first picosecond in (b).

The fast drop of the magnetization within the first picosecond after the point of zero delay is investigated with higher resolution. The time-dependent MOKE measurement of the FePd/CoPd bilayer is displayed together with the data of a pure CoPd film in Fig. 4.4(b). Note that the same pump laser intensity was used for both samples. Moreover, the relative quenching of the magnetization and the temporal responses of the two samples are almost identical. The data have been fitted with a double-exponential function, given by

$$\Theta_{K,norm} = 1 - Q \cdot H(\Delta t) \left[1 - e^{-\Delta t/\tau_m} \right] e^{-\Delta t/\tau_r}, \quad (4.1)$$

where τ_m and τ_r are the time constants for the demagnetization process and for the magnetic recovery, Q is the quenching and $H(\Delta t)$ is the Heaviside function [120].

The delay scans demonstrate that the underlying FePd does not lead to a significant change of the demagnetization dynamics of the CoPd. One could expect that the FePd magnetization, which is not directly exposed to the laser field, may stabilize the CoPd magnetization, resulting in a smaller quenching of the FePd/CoPd bilayer sample. On the other hand, superdiffusive spin currents should be excited in the same manner within the penetration depth of the pump laser light, because the top layers, *i.e.*, $\text{Co}_{35}\text{Pd}_{65}(40\text{ nm})/\text{Pd}(2\text{ nm})$, are identical for both samples. In this scenario, a similar quenching is understandable. Moreover, the demagnetization time constant of the FePd/CoPd bilayer ($\tau_m = 203 \pm 21\text{ fs}$) seems to be a bit shorter compared to the CoPd film ($\tau_m = 234 \pm 20\text{ fs}$), although the time constants are comparable within the fitting errors. In general, this trend could be related to the high electrical conductivity of the 40 nm thick FePd layer underneath the CoPd. The pure CoPd film is grown on a Pd seed layer, which is only 2 nm thin, and thus, any excited spin current reaches the insulating substrate earlier. This circumstance can potentially affect the quenching of the CoPd film, as it is the case in Ref. [38].

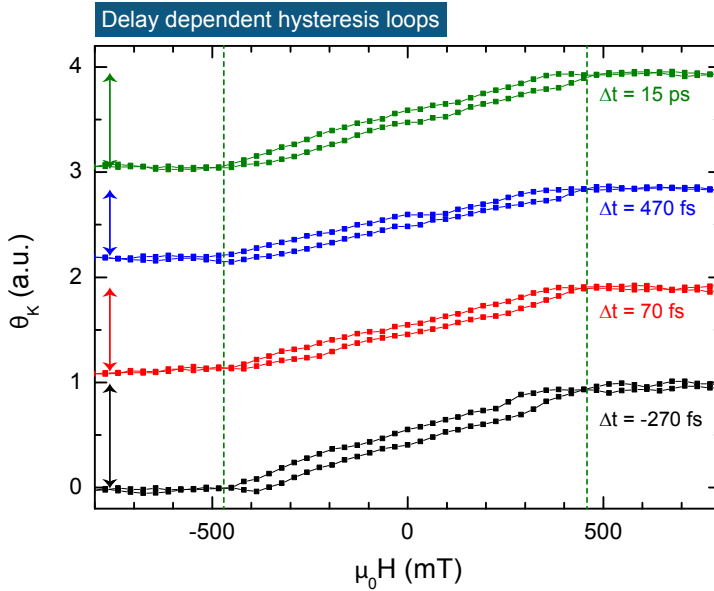


Figure 4.5: Hysteresis loops for different delays, normalized to the amplitude of the loop taken at $\Delta t = -270\text{ fs}$. The amplitudes of the individual loops are indicated by the arrows. The dashed lines mark the saturation fields of 460 mT.

In order to analyze, if the magnetic films in the bilayer decouple temporally due to the laser exposure, hysteresis loops for different delays Δt have been recorded (see Fig. 4.5). All curves are normalized to the amplitude of the hysteresis loop measured for $\Delta t = -270$ fs, *i.e.*, the probe pulse arrives before the pump pulse. For increasing delay ($\Delta t = 70$ fs and $\Delta t = 470$ fs) the amplitude of the hysteresis loop decreases and increases again (for $\Delta t = 15$ ps), which is indicated by the length of the arrows in Fig. 4.5. This behavior reflects the quenching and the recovery of the magnetization, which was already shown in Fig. 4.4. If the layers decouple, a reduction of the saturation field is expected, according to the static PMOKE analysis (Fig. 4.3). However, the hysteresis loops shown in Fig. 4.5 do not reveal any influence of the pump beam on the saturation field (indicated by the dashed lines) or on the shape of the loop for different delays. In conclusion, the CoPd magnetization quenches, but the coupling to the FePd film seems to be unaffected.

Another way to examine, whether the FePd magnetization is influenced by the demagnetization of the CoPd, involves pumping of CoPd from the front side and probing FePd through a transparent substrate from the back side. The general feasibility of the such experiments is demonstrated in Fig. 4.6, where a CoPd film was probed from the front side and pumped from the back side through a Au layer. The pump-probe geometry is schematically illustrated in (a) and the obtained time-resolved PMOKE signal is shown in (b). As indicated in the drawing, the sample is grown in the composition MgO (substrate) /Cr(1 nm)/Au(40 nm)/Co₃₅Pd₆₅(30 nm)/Au(2 nm), where MgO is used as transparent substrate, Cr as sticking layer, Au as reflector for the pump laser light and the thin Au layer grown on the top of the CoPd alloy serves as capping layer to protect the sample from oxidation. This sample system has been chosen for two reasons. First, it is an ideal candidate to test the above described pump-probe geometry, because the substrate is transparent for visible light and the Co₃₅Pd₆₅ alloy has been thoroughly studied in the pump-probe arrangement, where both beams impinge from the front side. Second, this sample provides the possibility to investigate the influence of hot electrons, excited by the pump pulse within the Au layer. The hot electrons may enter the CoPd layer and cause an ultrafast change of the magnetization, as it has been described in Ref. [28]. In the measurements shown in Fig. 4.6(b) the pump beam reaches a fluence of 15.5 mJ/cm² and the observed quenching of the magnetization is about 24%. Strikingly, τ_m amounts to 530 fs and thus the demagnetization process seems to be slower compared to case when a CoPd film is pumped and probed from the front side [Fig. 4.4(b)]. However, τ_m is known to depend on the quenching, which is very different in both measurements [121].

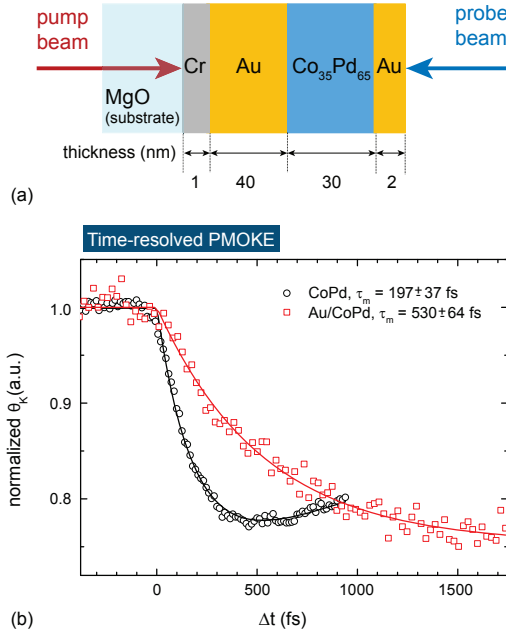


Figure 4.6: The pump-probe geometry is illustrated in (a). The pump laser illuminates the sample from the back side and is strongly suppressed by a 40 nm thick Au layer, while the CoPd magnetization is probed from the front side. The time-resolved PMOKE signal of a Au/CoPd sample, which is pumped from the back side with a fluence of 15.5 mJ/cm^2 , is shown in (b). A comparison with a CoPd reference sample pumped from the back side with 2.2 mJ/cm^2 reveals a very similar quenching of the magnetization by 24%.

Nevertheless, the study shown here demonstrates the possibility to demagnetize the CoPd layer through a 40 nm thick Au layer, which suppresses the infrared pump laser very efficiently. In detail, the transmission of a 40 nm thick Au film for infrared light with a wavelength of 800 nm is about 4%. In order to evaluate the influence of the Au layer quantitatively, a careful pump-fluence dependent analysis and a comparison with a CoPd reference sample [MgO/Co₃₅Pd₆₅(30 nm)/Au(2 nm)], measured in the same pump-probe geometry, are required. This comparison reveals for both samples (Au/CoPd and CoPd reference) a very similar quenching of the magnetization of about 24%, when using a pump fluence of 15.5 mJ/cm^2 and 2.2 mJ/cm^2 , respectively. Assuming that 4% of the infrared light are transmitted through the Au film, the fluence of the residual pump beam

is about 0.62 mJ/cm^2 . Consequently, a much lower quenching is expected for the Au/CoPd sample, because the pump fluence is about 3.5 times lower compared to the CoPd reference sample. This factor probably underestimates the relative difference in the absorbed pump fluence, because reflections at surfaces and interfaces should be taken into account for both samples. In this case, it is expected that the CoPd layer absorbs about 41 % of the incident light for the CoPd reference sample and less than 1 % for the Au/CoPd sample, corresponding to a relative difference in the absorbed pump light of approximately a factor of 6. Thus, the comparison of the two samples gives a strong indication that the ultrafast quenching observed for the Au/CoPd sample cannot be explained by considering exclusively the residual light transmitted through the Au layer. Instead, laser-excited hot electrons potentially contribute to the demagnetization process. This is also supported by the strong differences in τ_m observed for the two samples. The CoPd reference sample quenches much faster compared to the Au/CoPd, which agrees qualitatively with Ref. [28]. Finally, it is remarkable that the presented results seem to exclude that the direct spin-laser field interaction induces the ultrafast demagnetization [114].

4.4 Conclusion

The pump-probe experiments on CoPd alloys and FePd/CoPd bilayers reveal the ultrafast response of the magnetization upon pumping with femtosecond laser pulses. The comparison of both samples shows a very similar behavior regarding the ultrafast demagnetization dynamics. A laser-induced decoupling of the magnetic layers, as presented in [96], has not been observed, suggesting that the illumination of both layers could be necessary for a decoupling. Considering the FePd/CoPd bilayers, the results obtained raise the interesting question, whether the FePd magnetization is affected by the quenching of the CoPd. The answer to this question can potentially be delivered by pump-probe experiments using XUV light or soft X-rays, because the magnetic signals from certain layers can be distinguished by employing element-selective measurement techniques. This is a strong advantage compared to time-resolved experiments based on visible laser radiation, where the magnetic response of individual layers is estimated by calculating the penetration depth of the light. Thus, an element-selective photon-in-photon-out technique is a promising approach to clarify, if the FePd magnetization and especially the magnetic domains in both layers are influenced by the laser illumination. Such time-resolved examinations of the ultrafast evolution of the domain patterns can be accomplished in a sophisticated approach, using resonant magnetic scattering (RMS). Nevertheless, the presented analysis of the

magnetic coupling in FePd/CoPd bilayers, which is based on infrared and visible laser pulses, provides important information for future RMS studies, because ultrafast changes of the magnetic coupling could significantly influence the domain pattern of the individual layers.

In addition, first experiments of front-side probing and back-side pumping of Au/CoPd samples have been shown. The experimental results demonstrate the possibility of quenching the CoPd magnetization, while pumping through a 40 nm thick Au layer, which suppresses the pump laser light. The experimental findings support the idea that laser-generated superdiffusive spin currents contribute to the ultrafast demagnetization process.

Due to the promising opportunities of time-resolved RMS studies, the following chapter discusses the realization of RMS experiments using a tabletop XUV source, driven by femtosecond laser pulses.

5 Resonant Magnetic Scattering with Tabletop XUV Radiation

5.1 Introduction

This chapter describes RMS studies with XUV light, which has been created by HHG using femtosecond laser pulses. After the introduction of the laser setup, the generated XUV light is characterized in terms of photon energy and XUV flux. The characterization allows an estimation of the expected RMS signal, caused by the light scattering at the magnetic domain pattern. The feasibility of RMS experiments is demonstrated and the results are compared with MFM measurements. Furthermore, the pronounced influence of intense laser exposures on both the domain pattern and the sample morphology is studied with AFM, MFM and RMS.

5.1.1 Laser Amplifier System

The most important device for this experiment is a multipass laser amplifier system (Dragon, *KMLabs*). Although a detail description of such powerful laser systems is beyond the scope of this thesis and can be found elsewhere [122], the main principle of this laser is described in the following. The aim of this amplifier system is to transfer the pulse energy of an intense and "long" pump pulse of a Nd:YAG laser (LDP200, *Lee Laser*, $P = 70$ W, $T_{Rep} = 3$ kHz, $\Delta t < 120$ ns, $\lambda = 532$ nm) to a much weaker but also orders of magnitude shorter seed pulse of a Ti:Sapphire laser (Griffin3, *KMLabs*, $P = 200$ mW, $T_{Rep} = 80$ MHz, $\Delta t = 20$ –30 fs, $\lambda = 800$ nm). Seed and pump pulses overlap spatially and temporally in a Ti:Sapphire crystal, which is cooled to 40 K with a closed-loop He refrigerator and is mounted inside a vacuum chamber evacuated to 10^{-9} mbar. The cooling is required to reduce the thermal load and it minimizes the thermal lens effect for any average pump intensity, providing the option to change easily the repetition rate of the system. Due to the long duration of the pump pulses one can repeat this amplification process by using an unstable resonator, which guides the seed laser many times through the same position on the Ti:Sapphire

crystal (therefore such lasers are called "multipass amplifiers"). After 13 to 15 passes the gain is maximum and the amplified seed pulse is steered out of the resonator (see Fig. 5.1). The high peak intensity during the amplification can result in nonlinear optical effects or even damages of the Ti:Sapphire crystal, when femtoseconds long pulses are seeded. Therefore, a certain combination of mirrors and a grating (the so-called "stretcher") is placed into the seed path before the crystal to elongate the seed pulses to picoseconds. The optical path of the bluish and reddish part of the seed laser spectrum differs inside the stretcher and the resulting positive chirp stretches the pulses temporally. The peak intensity of these stretched pulses can be kept below the destruction threshold during the amplification. The stretched amplified pulses are compressed again to femtoseconds, using another set of two gratings and a retroreflector, forming the so-called "compressor". The advantage of using two gratings for the compressor (in general it is feasible to design a compressor with only one grating) is the possibility to control the group velocity dispersion (GVD) and the third order dispersion (TOD) by optimizing the distance and the angle between the gratings. The positive chirp induced by the stretcher on the seed pulses and addition dispersion originating from the remaining optical elements are removed by the compressor. Laser systems using this very successful technique for creating high power, ultrashort laser pulses are also called chirped pulse amplifiers (CPA). In total, the pulse energy of the seed laser is increased from 2.5 nJ to 2.2 mJ. Of course, the repetition rate is reduced from 80 MHz to 3 kHz, but the pulse duration is still in the femtosecond regime (about 35 fs).

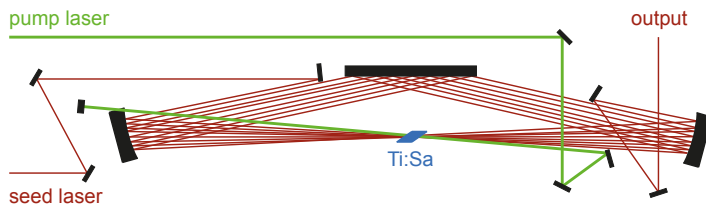


Figure 5.1: Schematic drawing of the cavity of the laser amplifier system (adapted from [122]). The pump laser (green) and seed laser (red) overlap in a strongly cooled Ti:Sapphire crystal.

One can make a comparison with a continuous wave (CW) light source to get a better understanding for the power delivered by a CPA. CW lasers with a radiant power of 2 kW are used in many applications, including applications like cutting of thick steel plates. The radiant power of an amplified ultrashort pulse can be estimated by $P = \frac{E}{\Delta t}$, where E is the

pulse energy and Δt the pulse duration. Thus, a 35 fs long, 2 mJ pulse leads to a power of about 60 GW. When both types of lasers are focused to a spot with a diameter of 50 μm , the 2 kW CW laser reaches a flux density of $10^8 \frac{\text{W}}{\text{cm}^2}$, whereas the intensity of a CPA pulse is about $3 \cdot 10^{15} \frac{\text{W}}{\text{cm}^2}$. The threshold for generating high harmonic orders of ultrashort laser pulses in noble gases, which is explained in the following section, is about $10^{13} \frac{\text{W}}{\text{cm}^2}$ and can thus only be reached with the CPA pulse.

5.1.2 High-order Harmonic Generation

HHG using noble gases is a very elegant way of up-converting the photon energy of a visible laser to the XUV spectral range, while many advantages of the laser are preserved or even improved [34]. XUV pulses created with HHG exhibit only a small divergence (typically a few milliradians), they are highly coherent and the pulse duration can be reduced to attoseconds. The polarization of the XUV light is in general linear, but it has been demonstrated recently that it is also possible to create circularly polarized HHG radiation [123]. The HHG process can be explained with a three-step model, if the laser pulse is described by an electromagnetic field $\mathbf{E}(t)$, oscillating with the frequency ω inside an envelope given by a Gaussian function. A detailed description of this model is given in [124] and an illustration is plotted in Fig. 5.2. The model describes an electron, which is bound to a gas atom by a Coulomb potential and is additionally influenced by an external laser field, which can be expressed by

$$V(\mathbf{r}, t) = -\frac{e^2}{4\pi\epsilon_0 r} + e\mathbf{E}(t)\mathbf{r}.$$

\mathbf{r} is the distance to the atomic core, $\mathbf{E}(t)$ is a time-dependent field of the laser pulse and the other constants have their common meaning.

If the amplitude of $\mathbf{E}(t)$ and the frequency ω are in a certain regime, the potential barrier for an electron bound to the core of the gas atom is reduced and a tunneling process becomes probable. The "tunneling ionization" is the first step of the model. In the second step, the "propagation", the released electron follows the oscillation of the electromagnetic field. On certain trajectories the electron hits again the gas ion and "recombines", which is the third step of the model. In the recombination step the electron can release its gain in energy by emitting a photon. One important parameter used for a theoretical analysis is the so-called "Keldysh parameter" γ given by

$$\gamma = \sqrt{\frac{I_p}{2U_p}}, \quad U_p = e^2 E_0^2 / (4m_e \omega^2),$$

where I_p denotes the ionization potential of the atom, U_p the ponderomotive potential, E_0 the amplitude of the electromagnetic field and ω its frequency. For $\gamma < 1$ tunneling can occur, whereas the extreme cases, *i.e.*, $\gamma \gg 1$ or $\gamma \ll 1$, lead to multiphoton absorption (for a large ω) or barrier-suppressed emission (for a large E_0). Moreover, the three-step model predicts the highest possible photon energy (cutoff energy, $\hbar\omega_c$) which can be created by the recombination of the accelerated electron. According to the relation

$$\hbar\omega_c \sim 3.17U_p + I_p, \quad (5.1)$$

the cutoff energy is proportional to U_p and I_p . Depending on the employed gas and the laser power, $\hbar\omega_c$ is typically in the order of 100 eV. It has been demonstrated that cutoff energies in the keV regime can be reached either by using a gas with a high ionization potential (like He) or by increasing the laser wavelength, which in turn raises U_p [125, 126].

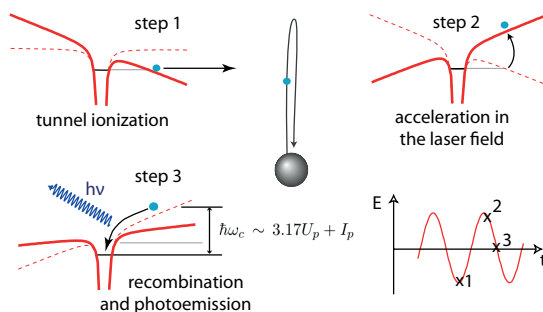


Figure 5.2: Sketch of the three-step model for generating high harmonic orders of a visible laser. After the ionization (step 1), the electron gets accelerated (step 2) and recombines with the atom (step 3). The occurrence of the different events with respect to the laser cycle is marked in the right, lower corner (taken from [124]).

Another very important ingredient for a high XUV flux is the phase-matching between the fundamental laser light and the harmonic order. For second harmonic generation (SHG) a known method to achieve phase-matching is based on rotating a frequency doubling crystal with respect to the incoming electric field vector, which equalizes the phase velocities of the fundamental laser light and its second harmonic. When the nonlinear medium is a gas, a different solution is required. In our experimental setup, a gas-filled capillary (serving as an optical waveguide) is used for HHG and consequently three different contributions of the frequency-dependent wave vector have to balance each other for phase-matching: the neutral

dispersion of the noble gas, the plasma dispersion and a geometric dispersion originating from the waveguide approach. The plasma is formed due to the large number of laser-ionized electrons, which do not recombine with the parent atom during the field oscillation. The resulting plasma density depends on the laser flux and pulse duration. The neutral dispersion has the opposite sign of the two other contributions and thus phase-matching can be achieved by optimizing the gas pressure. As the total dispersion strongly depends on the density of the laser-induced plasma, the phase-matching process is only possible up to a certain laser intensity threshold. Therefore, higher intensities of the fundamental laser do not necessarily result in a higher XUV flux. On the other hand, the wavelength of the driving laser is a very useful parameter for producing intense HHG radiation. Frolov *et al.* demonstrated that the efficiency of the photon conversion in HHG scales with λ^{-x} , where x is between 5 and 6 [127]. Thus, a shorter wavelength of the driving laser yields a pronounced increase of the XUV flux, but accordingly to equation 5.1 this limits the maximum photon energy. Nevertheless, the measured efficiencies can be improved from 10^{-5} ($\lambda = 800$ nm) to 10^{-4} for frequency doubled light pulses from a Ti:Sapphire laser ($\lambda = 400$ nm) or even to 10^{-3} , when UV laser pulses ($\lambda = 270$ nm) drive the HHG source [128, 129].

Furthermore, HHG delivers a remarkable temporal resolution, because experimental and theoretical studies point out that the generated light pulses can be as short as a few attoseconds (10^{-18} s) or even reach the zeptosecond (10^{-21} s) regime [130, 131]. As the XUV light is created many times within one laser pulse, a train of XUV pulses is typically observed. In this case, the duration of a single XUV pulse is about a few hundred attoseconds (Fig. 5.3, bottom).

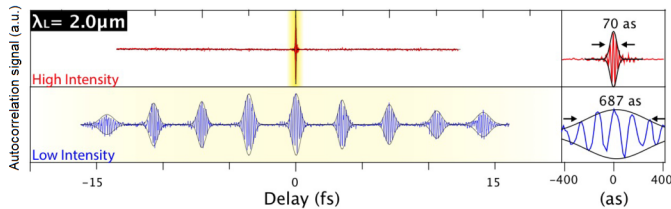


Figure 5.3: Autocorrelation signal from a single attosecond XUV pulse (top) and a pulse train (bottom) obtained with different intensities of the infrared laser ($\lambda = 2 \mu\text{m}$) driving the HHG source (adapted from [132]).

For pump-probe experiments in the attosecond regime it is necessary to generate single XUV pulses. A single-pulse train has been recently created by using infrared lasers ($\lambda = 2 \mu\text{m}$) for HHG and optimizing carefully the laser intensity (Fig. 5.3, top) [132]. In this way the temporal window for phase-matching can be narrowed, resulting in single pulses with a width of 70 as.

Fig. 5.4 shows a typical HHG spectrum, which illustrates several properties of the HHG process. For example, only odd harmonic orders are created. Due to the symmetry of the oscillating electric field, XUV pulses are generated twice per optical cycle and thus only odd harmonic orders can interfere constructively. It is also possible to create in addition even harmonic orders, if two laser fields, consisting of the fundamental and the second harmonic, are combined for pumping the HHG source [133]. The intensity of the higher harmonics is not decreasing dramatically with increasing harmonic order, as it is observed in other nonlinear photon conversion processes. Instead the intensity of the first harmonic order decreases linearly in the *perturbative regime*, followed by a broad spectral range of almost constant intensity. After this *plateau*, the intensity drops for decreasing wavelength, until it reaches zero at the *cutoff* energy. The broad plateau makes HHG sources very useful for spectral analysis in many applications. In the case of resonant magnetic scattering, it will be important that the tabletop XUV source is capable to reach the M absorption edges of ferromagnets located between 53 eV (23.4 nm) and 66 eV (18.8 nm).

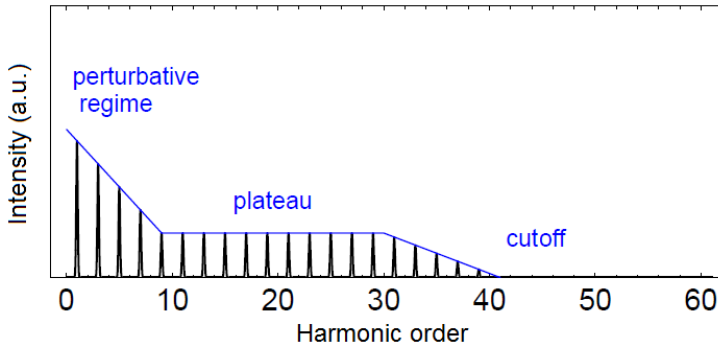


Figure 5.4: Typical HHG spectrum (adapted from [134]).

5.2 Experimental Setup

For the realization of the RMS experiment it is necessary that the laser system fulfills the requirements for HHG. Therefore, the laser alignment has to be optimized such that a radiant power of 6 W (at a repetition rate of 3 kHz) is reached, corresponding to an energy per pulse of 2 mJ. The transverse mode of the laser should be of Gaussian shape and free of spatial chirps. Furthermore, it is desirable to achieve a large bandwidth of the laser spectrum to provide the smallest possible pulse duration, as discussed below. These parameters can be influenced by the number of passes through the Ti:Sapphire-crystal and by using a gain flattening filter inside the amplifier cavity. The pulse duration and the temporal chirp of the laser pulses are analyzed by using frequency-resolved optical gating (FROG). While measuring FROG traces, the compressor of the laser amplifier is adjusted to minimize the pulse duration and the temporal chirp. Details about FROG can be found in [135].

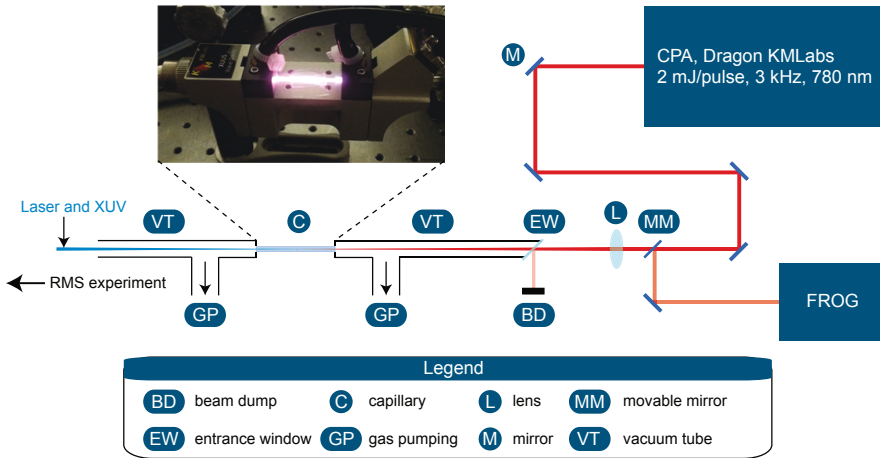


Figure 5.5: Schematic drawing of the experimental setup for HHG. The photograph shows the glass capillary (fiber) while operating the HHG source. The CPA delivers intense ultrashort laser pulses, which are focused into the fiber to generate XUV radiation. A movable mirror can be used to guide the laser beam to a FROG characterization device.

The basic principle of the setup is presented in Fig. 5.5. The laser beam can be redirected with a movable mirror to a FROG characterization device, before it is focused into the gas-filled capillary (also called fiber) which is used for the XUV light generation.

The CPA spectrum is centered at 780 nm and has a bandwidth of 50 nm [see Fig. 5.6(a)]. Assuming Gaussian pulses, the *time-bandwidth product* predicts a minimum pulse duration of 18 fs for this bandwidth [136].

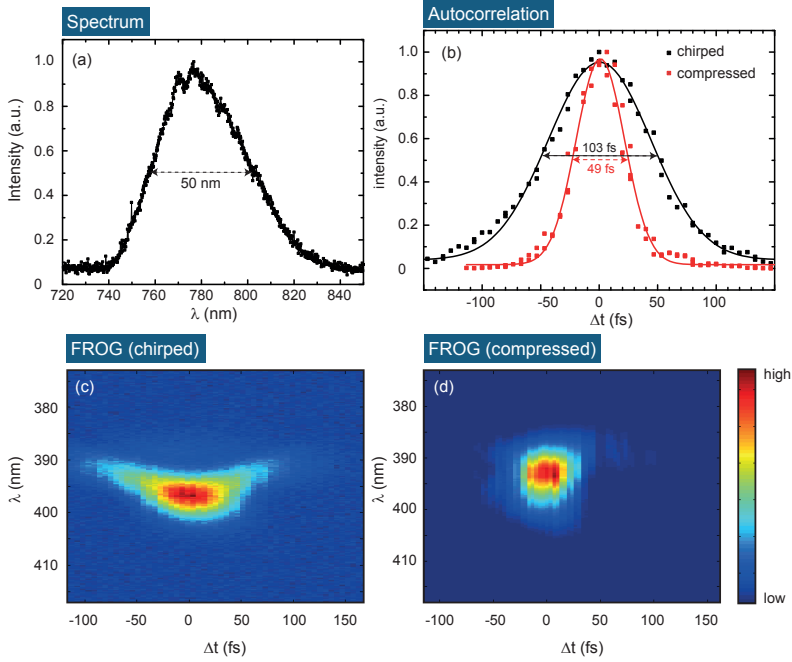


Figure 5.6: (a) shows the spectrum of the laser amplifier and (b) the autocorrelation signals of a chirped (black squares) and a properly compressed pulse (red squares). The solid lines are Gaussian fits and the dashed lines indicate the width of the autocorrelation signals. The corresponding FROG traces of the chirped and compressed pulse are presented in (c) and (d), respectively.

The measured autocorrelation signals for a chirped (black squares) and a properly compressed pulse (red squares) are plotted in Fig. 5.6(b). The corresponding FROG traces are shown in Fig. 5.6(c) and Fig. 5.6(d), respectively. The FWHM overestimates the real pulse width, because the autocorrelation is a convolution of an laser pulse with itself [135]. For Gaussian pulses the pulse width τ_p is related to the width of the autocorrelation τ_A via $\tau_A = 1.41 \tau_p$. Thus, the compressed pulse has a pulse duration of 35 fs.

As mentioned above, for generating high harmonic orders the laser beam is focused into a hollow glass capillary with an inner diameter of $150\ \mu\text{m}$ (XUUS, *KMLabs*). The focus length of the fused silica plano-convex lens is 40 cm and the entrance window of the vacuum tube is mounted at Brewster angle. This prevents that the back reflection from this window travels back to laser amplifier and disturbs the seeding process. The capillary is filled with a noble gas (in this work either Ar or Ne). As the generated XUV radiation is strongly absorbed in air, it is necessary to introduce a suitable vacuum system to conduct the scattering experiment. Sufficient gas pumping is necessary before and after the capillary to introduce a pressure gradient inside the fiber and to remove residual gas from the vacuum chambers.

Figure 5.7 shows a drawing of the experiment, where all components downstream the capillary are mounted inside vacuum chambers evacuated to 10^{-5} mbar. The pressure in the capillary can be adjusted with a mass flow meter (PC99, *mks*) to achieve the best phase matching conditions for the chosen noble gas. A typical value for the gas pressure is about 20 mbar for Ar and about 50 mbar for Ne. The visible laser light is separated from the HHG radiation by two 150 nm thick Al filters (*Luxel corporation*). The XUV radiation is monochromatized and focused by a pair XUV multilayer mirrors (also called Bragg mirrors) consisting of a multilayer structure of Mo and Si layers. These mirrors were produced by the Fraunhofer IWS in Dresden and they are used to select 62 eV photons, matching the Co $M_{2,3}$ edges. The reflectivity at 62 eV is about 35% and thus the total transmission of the mirror pair is 12%. The incident angle of the light is 5° from the surface normal and the first mirror is spherically curved with a radius of 1 m. For very high laser intensities it can become important to reduce the power of the laser before illuminating the Al filters, in order to avoid damages of the sensitive Al foils by the laser. In this case, the filters are placed behind the Bragg mirror pair, because the laser intensity is significantly reduced downstream the monochromator. A different design is utilized, when the entire HHG spectrum is desired for the experiment. In this case, a Si wafer and a Au toroidal mirror are mounted in grazing incidence (about 83° against the surface normal) to maintain a high reflectivity for all generated XUV photons. The flat wafer is used to reduce the laser intensity, because Si absorbs infrared radiation, while it reflects XUV light. The reflectivity depends on the photon energy, the polarization, the incidence angle and the thickness of the SiO_2 layer, which is formed by oxidation on the top of the Si surface. In the best case, the reflectivity for 62 eV photons is about 67% for the Si wafer and about 75% for the Au mirror. The total transmission of both elements at 62 eV is in this best case scenario about 50%, which is four times larger than the transmission of the Bragg mirror

pair (12%). Nevertheless, monochromatizing the HHG radiation makes the interpretation of the scattering results easier due to the precise definition of the photon energy. Furthermore, the Bragg mirrors guarantee better focusing compared to the toroidal mirror.

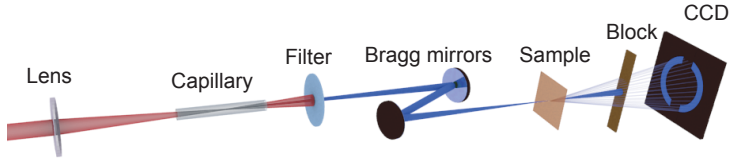


Figure 5.7: A schematic drawing of the RMS experiment with XUV light created by HHG. The generated XUV light is separated from the fundamental laser with thin Al filters. Subsequently the XUV radiation is monochromatized by a Bragg mirror pair and focused onto a transparent sample. The scattered light is recorded with a CCD camera and the direct beam is blocked with a wire.

The transparent sample, which is mounted on a 3D-manipulator driven by piezo motors (SLC-1740, *SmarAct*), is placed in the focal plane of the curved mirror. The focus spot is about $40\ \mu\text{m}$ in diameter and a charge coupled device (CCD) camera (iKon-L, *Andor*) is placed 7 cm behind the sample. The transmitted beam is blocked by a metallic wire (beam block), in order to efficiently use the dynamic range of the detector. The beam block is mounted on a movable stage. This allows the observation of the direct beam on the CCD camera, which is needed for the optimization of the HHG beam alignment. More details about HHG and related applications can be found in Refs. [35, 137, 138].

5.2.1 Considerations for the RMS Intensity

Studies with the introduced HHG source were recently presented by Denis Rudolf [116], where the photon flux of the 39th harmonic order located at 62 eV was estimated to be $6 \cdot 10^6$ photons per second. This value is certainly the lower limit of the XUV flux, because the power of the laser driving the HHG source was smaller (4 W at 2 kHz). Nevertheless, one can make an approximation for the expected RMS intensity. When the transmission of the Al filters (66 %) and the reflectivity of the Bragg mirror pair (12 %) at 62 eV are regarded, a photon flux of about $5 \cdot 10^5$ photons per second is reached at the sample. The typical magnetic scattering efficiency at the Co $M_{2,3}$ absorption edges is 10^{-x} with $x = 5-6$

[41] and, consequently, in the best case 5 scattered photons per second are expected. As the light scattering from randomly oriented magnetic domains results in a ring, the area where the scattering signal is visible, has to be taken into account. Assuming a ring radius of 500 pixels and a ring width of 100 pixels, the RMS signal per pixel is about $1.6 \cdot 10^{-5}$ photons per second. This would require to integrate the scattering signal over 17 hours to reach a statistic of one photon per pixels. Therefore, RMS with a HHG source is still at the experimental limit. Nevertheless, in section 5.3.2 it is demonstrated that this experiment is feasible by improving the photon flux of the HHG source.

5.2.2 Spectrum of the HHG Source

In Chapter 5.1.2 it has been mentioned that the HHG flux and spectrum strongly depend on the laser radiant power, the gas pressure and the capillary alignment. An efficient method for the optimization of the HHG source would demand live monitoring the RMS signal, while changing the external parameters. Such a procedure is not feasible, because the intensity of the scattered light is very weak, as described in section 5.2.1. Therefore, the optimization is accomplished by measuring the XUV spectrum after the Bragg mirrors with a transmission grating. This solution is chosen due to the simple design, which does not require an additional spectrometer with another detector.

The grating has a grating constant of 250 nm and it consists of a 300 nm thick polymethyl methacrylate (PMMA) film, patterned with e-beam lithography. It covers in total an area of $(700 \times 700) \mu\text{m}^2$ and the substrate is a 50 nm thin Si_3N_4 membrane. The use of PMMA structures simplifies the grating fabrication significantly, because the complicated lift-off, which is necessary for metallic gratings, becomes redundant. Furthermore, the PMMA grating can be covered with 20 nm Al to increase the robustness and to protect the grating from laser illuminations. It has been shown that the exposures with XUV and laser light can damage PMMA structures [116]. AFM images of a produced PMMA/Al-grating are shown in Fig. 5.8.

Figure 5.9 shows XUV spectra measured with a Ne-filled capillary. For the spectral analysis the sample is moved out of the XUV beam and the PMMA grating is placed 21 cm in front of the CCD sensor. The full spectrum (red curve) was measured with the Si reflector and the toroidal mirror, while the monochromatized spectrum (blue curve) was taken with the Bragg mirror pair. First, the entire spectrum of the generated XUV light covers all three $M_{2,3}$ absorption edges of the 3d ferromagnets (Fe at 53 eV, Co at 60 eV and Ni at

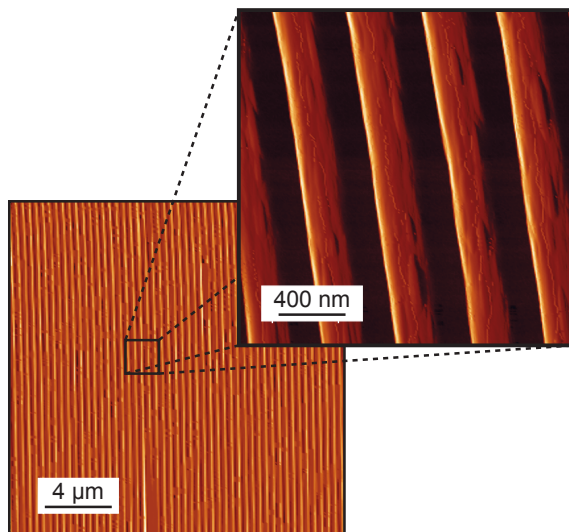


Figure 5.8: AFM pictures of a PMMA transmission grating, fabricated on top of 50 nm thin Si_3N_4 membrane and covered with Al. The left picture shows an area of $(20 \times 20) \mu\text{m}^2$ and the right picture is zoomed by a factor of 10.

68 eV). Second, the Bragg mirror pair selects the 39^{th} harmonic order at 62 eV closely matching with the Co $M_{2,3}$ edges at 60 eV. Studies with synchrotron and HHG radiation demonstrated that the Co resonance is at least 5 eV broad, if the magneto optical constants $\Delta\delta$ and $\Delta\beta$ are taken into account for the RMS signal [95, 139]. The 37^{th} and 39^{th} harmonic orders are both close to the maximum of the resonance at 60 eV, but the Bragg mirror pair suppresses the 37^{th} order by a factor of 10 in intensity relative to the 39^{th} order. Therefore, the RMS pattern is formed by 62 eV photons corresponding to a wavelength of 20 nm.

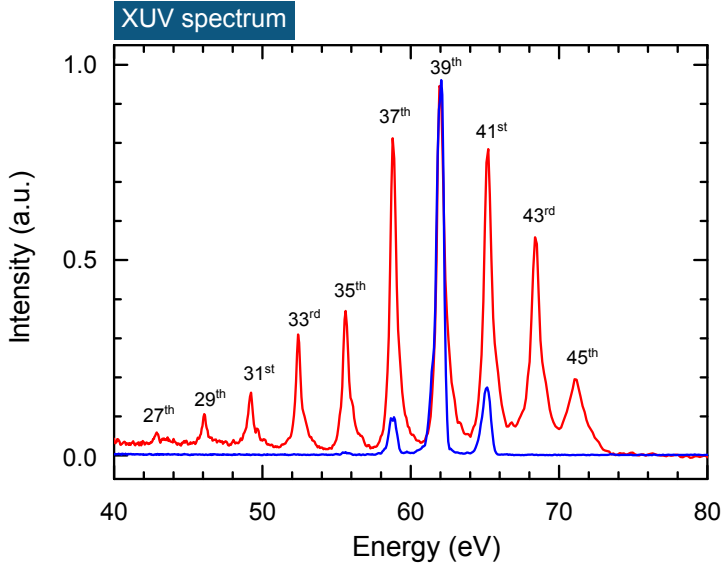


Figure 5.9: Comparison of the full HHG spectrum (red curve), taken with a Au toroidal mirror, and the monochromatized spectrum (blue curve), measured with the Bragg mirror pair. The numbers mark the harmonic orders. In both cases the capillary was filled with Ne for the XUV light generation.

In principle, the energy scale in Fig. 5.9 can be calibrated using the Bragg equation

$$\sin\left(\frac{\lambda}{g}\right) = \tan\left(\frac{0.0135 \cdot r}{D}\right), \quad (5.2)$$

where λ is the wavelength, g the grating constant, r the distance on the detector in pixels between the transmitted and the diffracted beam, 0.0135 is the pixel size in millimeters and D is the distance between the sample and the detector. There are several sources for calibration errors when using equation 5.2. An uncertainty σ_D of 1 mm in the measurement of the distance D (corresponding to relative error of $\sigma_D/D = 0.5\%$) results in an energy uncertainty $\Delta E/E$ of approximately 0.5%. A far larger error is caused by deviations of the grating constant. If the error of the grating constant σ_g is 10 nm (corresponding to relative error of $\sigma_g/g = 2.5\%$), $\Delta E/E$ will be about 4%. This would imply that for 62 eV the error of the energy scale is 2.5 eV.

To improve the precision of the spectrometer two properties can be utilized, when a full

HHG spectrum is recorded additionally. First, the spacing of the harmonic orders is known to be twice the laser energy (*i.e.*, 3.18 eV for $\lambda_{laser} = 780$ nm). Second, the cutoff energy is given by the Al L₃-edge at 72.55 eV. Therefore, recording the full spectrum yields a much smaller energy uncertainty of approximately 0.5 %, which is mainly caused by the uncertainty in the experimentally determined cutoff energy.

5.3 Results and Discussion

5.3.1 Sample Characterization using MOKE and MFM

In the following, the magnetic properties of Co/Pt multilayer films are investigated. Hysteresis loops are recorded by employing the polar magneto-optical Kerr effect (PMOKE) and the magnetic domain pattern is studied by magnetic force microscopy (MFM). The Co/Pt multilayers were fabricated at the University Hamburg using magnetron sputtering. These samples consist of the following composition: Pt(5 nm)/[Co(0.8 nm/ Pt(1.4 nm))]_x/Pt(1.6 nm) with $x = 8$ or $x = 16$.

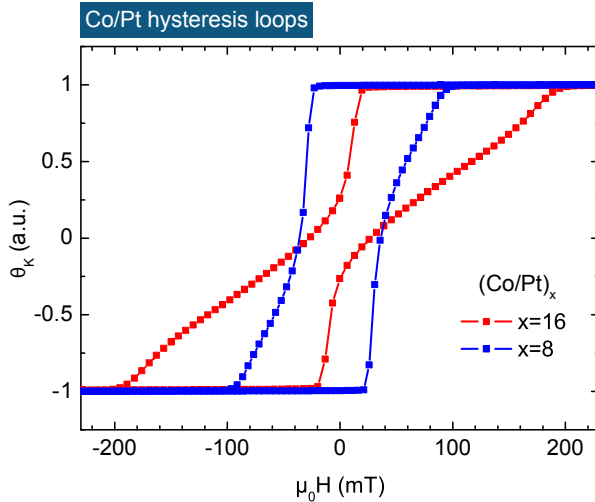


Figure 5.10: Hysteresis loops obtained with PMOKE from Co/Pt multilayer films with 8 (blue) and 16 (red) repetitions.

In both systems the uniaxial anisotropy favors the formation of an out-of-plane domain pattern, but the sample systems differ from each other by the canting angle of the magne-

tization, the coercive field and the saturation magnetization. Details about these very well studied multilayer films can be found elsewhere [7, 140, 141]. The normalized hysteresis loops for 8 and 16 repetitions are presented in Fig. 5.10. Note that an out-of-plane oriented field of 200 mT is sufficient to saturate the samples. Such fields can be applied easily during the RMS measurements by a permanent magnet. The curvature of the hysteresis loops at remanence indicates the formation of a domain pattern, which is different for both samples. Consequently, distinguishable domain structures are observed in MFM measurements of the two samples (Fig. 5.11), where nanometer-sized domains arrange randomly in a maze-like pattern. It is reasonable to keep in mind that the domain pattern at zero field depends on the magnetic history. For instance, highly aligned domain configurations can be formed by applying in-plane fields, whereas random structures are created by saturating the sample in out-of-plane directing. Both cases can result in different domain sizes at remanence.

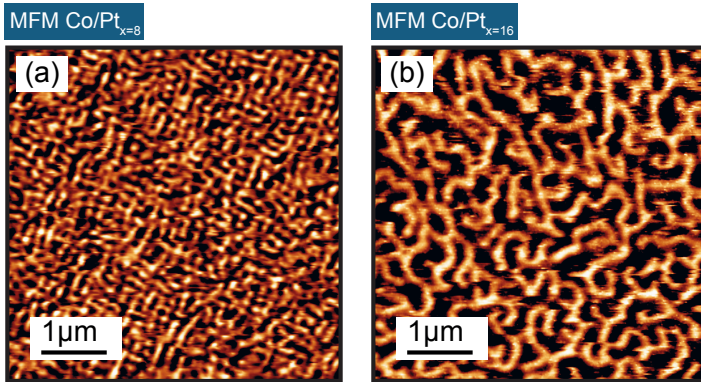


Figure 5.11: MFM images (phase contrast maps) for 8 and 16 repetitions of Co/Pt are shown in (a) and (b), respectively.

In general, both sample systems are suitable for the RMS experiment, but an increased thickness critically effects the transmission at 62 eV. In detail the total transmission, including the substrate, seed and buffer layers, is 2.61 % for $x = 8$ and 0.34 % for $x = 16$, which corresponds to an expected intensity difference of a factor of 7. Therefore, the photon-demanding RMS experiments are conducted with 8 repetitions of Co/Pt layers.

5.3.2 RMS with HHG - The Proof of Principle

In the following, it will be demonstrated that the introduced XUV source is capable to image nanometer sized magnetic structures in reciprocal space with RMS. This measurements can be seen as the first very important step for time-resolved RMS experiments, as mentioned before. To reach a high signal-to-noise ratio is essential that any residual light from the surroundings or from the driving laser is removed, because even a small background will accumulate for long exposure times. Further noise reduction is achieved by subtracting dark images from the data. This dark image contains readout and thermal noise (also called "dark current"), which are strongly suppressed by cooling the CCD sensor to $-60\text{ }^{\circ}\text{C}$. RMS images integrated during a 30 min exposure are shown in Fig. 5.12, where all data are taken from the same sample (named in the following B1). In (a) the out-of-plane magnetic domains are randomly arranged in the sample plane resulting in a scattering ring, whereas in (b) the domains were aligned along the vertical direction by applying an in-plane field of 300 mT for a few seconds. Therefore, the scattering pattern becomes more point-shaped. In (b) the Q -scale of the image is different compared to (a), because the sample-to-detector distance is 1.5 cm shorter [7 cm in (a) and 5.5 cm in (b)]. In general, the alignment of magnetic domains in a stripe pattern can influence the domain width, but a clear change of the associated scattering vectors is not observable in Fig. 5.12. The images in the bottom row [Fig. 5.12(c) and (d)] were obtained by filtering the images in the top row [Fig. 5.12(a) and (b)]. The filter calculates the median of three neighboring pixels, yielding the strong increase of the signal-to-noise ratio.

The intensity of the total scattered light is 580 counts per second, which is used to estimate the photon flux of the source. The specifications of the detector promise a high quantum efficiency in the XUV regime ($> 70\%$), but for the lower limit estimation of the XUV flux a one-to-one relation between the measured counts and the photon number is assumed. The measured ratio of incoming and scattered photons is approximately $2 \cdot 10^{-5}$ (in agreement with other experiments [41, 95]), which implies a photon flux of $3 \cdot 10^7$ photons per second upstream the sample or $3.8 \cdot 10^8$ photons per second (with 62 eV) coming from the gas-filled capillary. This is about two orders of magnitude larger compared to XUV flux presumed in section 5.2.1. This significant improvement was achieved by implementing a stronger pump laser for the amplifier system and a careful optimization of the mentioned parameters that are essential for the XUV light generation.

The comparison of the here presented scattering images with previously published RMS data measured with a similar XUV source [41] leads to the following conclusions: first, the

photon flux is comparable ($4 \cdot 10^7$ photons per second were detected before the sample in [41]) and, second, the scattering efficiency is slightly higher for the Co/Pt multilayer film, which is investigated here ($7 \cdot 10^{-6}$ in [41]). Please note that investigations of the scattering efficiency for varying thickness of Co/Pd multilayer films revealed in the best case a very similar efficiency of $2.5 \cdot 10^{-5}$ at the Co $M_{2,3}$ -edges [95].

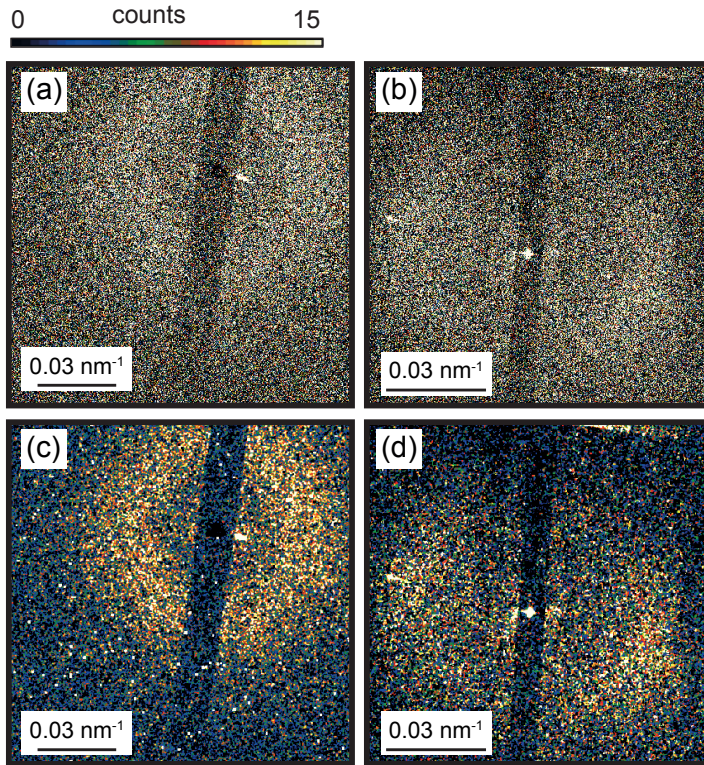


Figure 5.12: RMS images from sample B1 after a 30 min exposure with XUV light are shown in (a) and (b). In (b) the domains were previously aligned by an in-plane field of 300 mT. Both images are background corrected by subtracting a dark image. (c) and (d) show the same images after applying a median filter over 3 neighboring pixels.

5.3.3 Laser-induced Modifications of Co/Pt Multilayers

In the following, sample B1 is compared with an identically synthesized sample (named B2), which was illuminated for 1 min with intense ultrashort laser pulses, reaching a fluence of 0.2 mJ cm^{-2} , in order to study the influence of laser-induced modification on morphology and magnetism. The findings from AFM and MFM investigations are compared with RMS measurements. The pronounced changes, manifesting in different ways in the individual measurements, have not been observed so far and emphasize the impact of intense laser radiation on the nanometer-sized domains.

An optical micrograph image of the laser-illuminated sample B2 is given in Fig. 5.13(a) and energy density profiles of the impinging laser beam are shown in (b). The laser exposure of sample B2 leaves a permanent imprint on the membrane visible in the optical micrograph. Figure 5.14(a) and (c) show AFM images of the samples B1 and B2 and the corresponding MFM phase contrast maps are presented in (b) and (d). Note that the AFM and MFM measurements of sample B2 [Fig. 5.14(c) and (d)] are taken on the frame of the sample close to the laser imprint marked in the inset of (c) with a black cross. At the frame the heat dissipation is improved compared to the window region and the sample degeneration is smaller. As suggested by the pronounced amount of droplets on the sample surface, which are visible in (c), the intense laser pulses have partially ablated the multilayer film and the evaporated material re-deposits again on the surface [142–144].

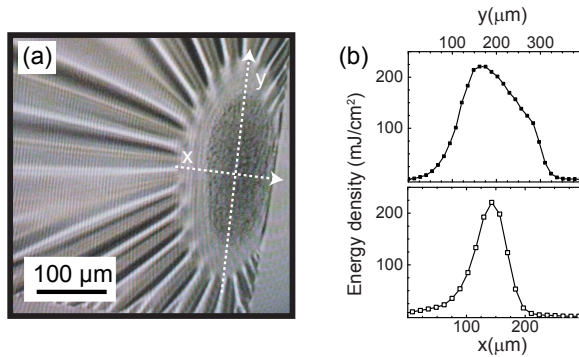


Figure 5.13: An optical micrograph of sample B2 after the laser exposure is shown in (a). Energy density profiles of the impinging laser beam along the dashed lines are presented in (b).

Furthermore, the MFM images indicate a strong permanent modification of the magnetic domain pattern, which shows a mixture of different domain sizes. The different color levels

in the MFM map may be caused by a partial in-plane orientation of magnetization. However, the laser pulses induce a non-equilibrium state during the exposure, which substantially affects the domain pattern, as shown by MFM. The details of the non-equilibrium state and following modifications of the domain pattern are not yet understood.

Figure 5.15(a) and (b) show the scattering images from both samples. The scattering from B2 occurs at much smaller momentum transfer vectors and the scattering intensity is strongly increased. This means that the average distance between the scattering centers is much larger for B2, which would be in agreement with the larger domain size shown in the MFM measurements [Fig. 5.14(d)].

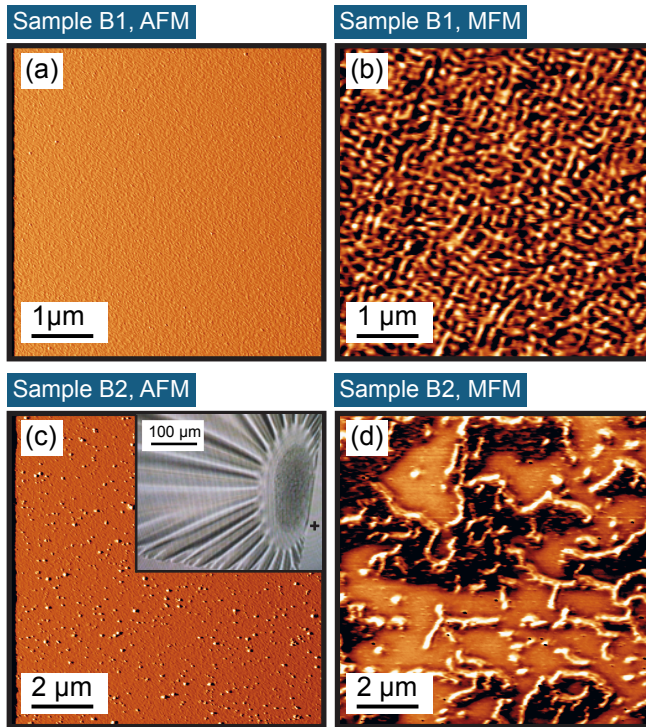


Figure 5.14: AFM amplitude error image and MFM phase contrast maps for sample B1 are shown in (a) and (b). (c) and (d) present the same images for the laser-illuminated sample B2. The inset of (c) shows an optical micrograph of the sample and the black cross mark the position where the AFM and MFM images have been recorded.

The radially integrated scattered intensity of the scattering patterns are given in Fig. 5.15(c), where the momentum transfer vector, Q , was calculated as described in Chapter 3. The RMS signal from B1 (blue curve) exhibits a peak at 0.035 nm^{-1} , corresponding to a domain size of 90 nm, when equal dimensions of "up" and "down" domains are assumed. This is in very good agreement with the radially integrated squared magnitude of the Fourier-transformed MFM image (red curve), yielding a domain size of 92 nm.

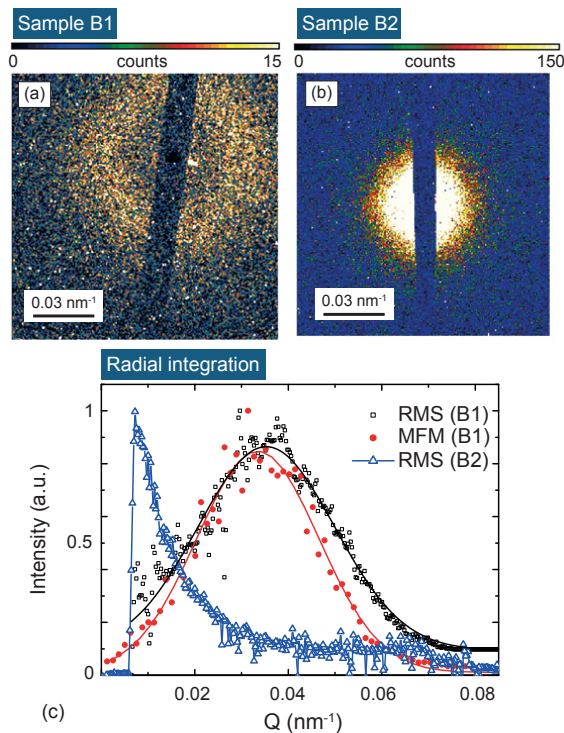


Figure 5.15: RMS images from the as-grown (B1) and laser-illuminated sample (B2) are presented in (a) and (b). The normalized radially integrated intensities are given in (c). The data points marked by the black squares are obtained from (a) and the blue triangles from (b). The red dots are taken from the radial integration of the squared magnitude of the Fourier-transformed MFM image presented in Fig. 5.14(b). The black and red solid lines are Gaussian-fits.

The FWHM, determined with Gaussian-fits, is very similar for both curves, *i.e.*, 0.034 nm^{-1} for the RMS and 0.031 nm^{-1} for the MFM measurement. A theoretical smearing of the ring

introduced by the 37th and 41th harmonic order would broaden the ring by $\Delta Q = 0.002 \text{ nm}^{-1}$, which is certainly far smaller than the actual FWHM of the scattering signal. Conclusively, it is reasonable to assume that the domain size distribution rather than the bandwidth of the XUV light causes the width of the scattering ring.

Remarkably, the maximum of the scattering curve from sample B2 [blue triangles in Fig. 5.15(c)] is probably hidden underneath the beam block and is therefore located at a Q -value smaller than 0.008 nm^{-1} , yielding a minimum real-space distance of 785 nm. Additionally, the scattering intensity is a factor of 10 higher compared to B1. This is an unexpected effect, because for larger domains, the scattering efficiency is expected to reduce, as the number of domains within the probed area decreases. In order to investigate the origin of the scattering signal, the experiment was repeated, while a permanent magnet was used to apply an out-of-plane field of 300 mT. The field saturates the magnetic film and therefore any magnetic scattering is expected to vanish. The scattering images taken at remanence and at saturation are identical, demonstrating that the scattering pattern has a non-magnetic origin. After considering several possible mechanisms, the most probable source for the detected signal are the randomly distributed droplets on the sample surface, which were already observed in the AFM characterization of the sample [Fig. 5.14(c)]. The lower limit of 785 nm for grain distance extracted from the RMS images is in good agreement with the AFM image.

It has been demonstrated that permanent changes of the magnetic anisotropy of magnetic thin films can be created by the exposure with femtosecond laser pulses [145]. Such modifications can be a consequence of laser annealing, which possibly improves the interface quality of a layered system or cause the formation of certain alloys with a different magnetic anisotropy. Therefore, the laser-exposed Co/Pt multilayer (sample B2), which was saturated by an out-of-plane field of 300 mT, is inspected again at remanence with MFM. These measurements are presented in Fig. 5.16 and show laser-induced changes of the domain pattern which are either reversible or permanent. Inside the visible imprint [white cross in Fig. 5.16(a)] no magnetic contrast is detected [Fig. 5.16(b)]. At the fringe of the visible imprint (yellow cross) the domain pattern remains in a modified state with an increased domain size of approximately 300 nm [Fig. 5.16(c)]. The MFM image, given in Fig. 5.16(d), was taken next to the imprint on the frame (black cross) and reveals a domain structure, which is very similar to the as-grown state [Fig. 5.14(b)] with an average domain size of approximately 100 nm. Note that the MFM image of sample B2 [Fig. 5.14(d)], was recorded after the laser-exposure, but before the saturation and it was measured at the same position (black cross), demonstrating the possibility to reverse the laser-induced

modification of the domain pattern with an external field. The permanent changes of the magnetic structures [Fig.5.16(b) and (c)] may be introduced by laser-sputtering, alloying, melting or interdiffusion, but so far it remains open, what causes the reversible domain state presented in Fig. 5.14(d). This issue could be addressed by time-resolved RMS experiments with laser intensities close to the sample ablation threshold, although these studies would require a precise tuning of the laser fluence to avoid the scattering on the laser-induced droplets shown in Fig. 5.15(b).

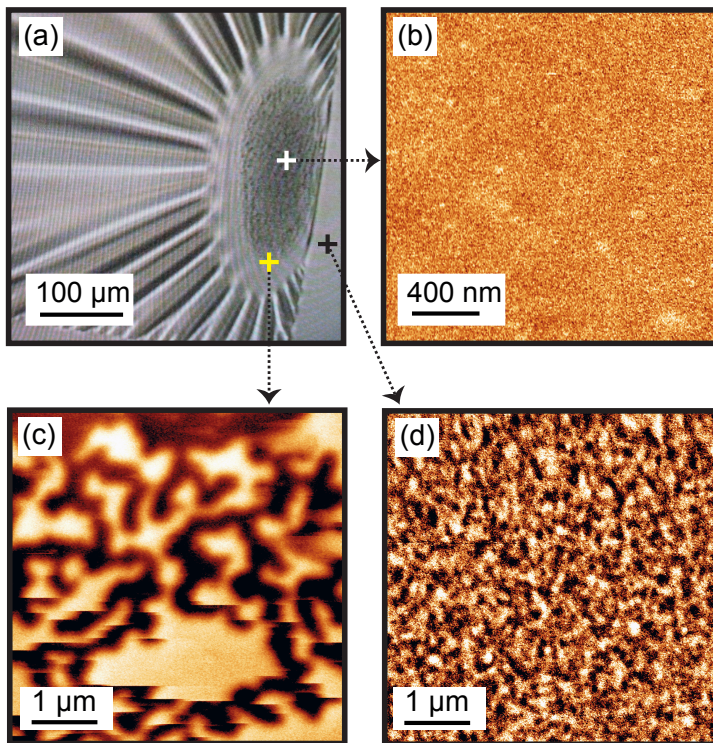


Figure 5.16: An optical micrograph of sample B2 is shown in (a). The MFM images in (b), (c) and (d) were taken after the saturation of the laser-exposed sample in an out-of-plane field. The images shown in (b), (c), (d) are taken at positions marked by the white, yellow and black crosses.

5.4 Conclusion

In this chapter it has been successfully demonstrated that resonant magnetic scattering from out-of-plane domain patterns of Co/Pt multilayer films is feasible using a tabletop HHG source. Consequently, the most important requirement for time-resolved experiments has been accomplished, although even higher XUV intensities are desirable for high quality pump-probe measurements, as shown in [94]. RMS, AFM and MFM studies unveil pronounced changes of the magnetic structure induced by intense femtosecond laser pulses, reaching a fluence of 0.2 J/cm^{-2} . The laser exposure results in permanent and reversible modifications of the sample, regarding morphology and magnetism. The RMS signal is superimposed by a non-magnetic background, originating from laser-ablated material, which is dispersed in the form of droplets over the sample surface. Interestingly, the MFM results show that the laser illumination either causes permanent changes of the magnetic domain pattern or creates a more complex state, which can be reversed to the as-grown configuration by saturating the Co/Pt multilayer. Such states may also be observed in pump-probe experiments and potentially provide new insights into the processes leading to ultrafast magnetization dynamics.

6 SAXS with Coherent XUV Light

6.1 Introduction

In the last years, new techniques using coherent X-ray radiation successfully demonstrated their potential for detailed investigations of structural sample properties. These approaches include for instance coherent X-ray diffraction [146], coherent diffraction imaging [147, 148], holography [149], ptychography [150] or X-ray photon correlation spectroscopy [151]. Recently, imaging experiments employing coherent XUV light from HHG sources have been realized [39, 152], thereby demonstrating the capabilities of laboratory light sources for resolving nanometer-sized objects in real space. This chapter introduces experimental techniques based on coherent diffraction, which provide interesting opportunities to investigate magnetic properties. Therefore, it is discussed whether laser-based HHG radiation can be applied for such studies. In particular, the longitudinal and transverse coherence properties are crucial for the experimental success, because both quantities significantly affect diffraction and imaging experiments. In this context, speckle patterns are examined, which have been obtained by scattering XUV light from Fe and FePd islands. The analysis of the resulting speckle contrast allows one to determine the number of coherent modes of the XUV radiation. Furthermore, diffraction patterns created by illuminating a knife edge are compared with the detected speckle contrast, underlining the influence of the coherence properties in the individual experiments. Moreover, knife-edge diffraction offers an elegant way to study the real part of the refractive index in the XUV spectral regime, as it is explained in the following. The here presented results reveal the potential of table-top HHG sources to examine magnetic thin films by taking advantage of the light coherence.

It has been shown in Chapter 5 that light scattering on randomly distributed magnetic domains leads to a scattering image, which can be related to the average domain size. This is even observable for radiation with a coherence area that is smaller than the beam spot on the sample. The illumination of a disordered system like a random domain structure with coherent radiation results in a specific interference pattern known as "speckle pattern",

caused by the light interference from all illuminated sample regions. Thus, a speckle pattern is a unique fingerprint of the exact arrangement of the scattering centers [153]. Figure 6.1 illustrates the influence of the coherence properties in a small-angle X-ray scattering (SAXS) experiment, where soft X-rays are scattered at magnetic domains. In (a) the sample is located close to the source and the X-ray beam is partially coherent over the illuminated area. The coherent regions within the beam profile are indicated by red circles and are slightly larger than the average domain period, d . The radially symmetric scattering signal occurs in reciprocal space at a certain momentum transfer vector, Q . In (b) the sample is further away from the source and a pinhole selects the coherent fraction of the X-ray radiation. The observed speckle pattern reflects the real-space structure within the beam spot. These speckle patterns can be reconstructed to real-space images using phase-retrieval algorithms [150], but these reconstructions can be time consuming and demand in many cases long exposure times of the original images. However, the speckle pattern itself gives very useful information about the sample structure and the light properties.

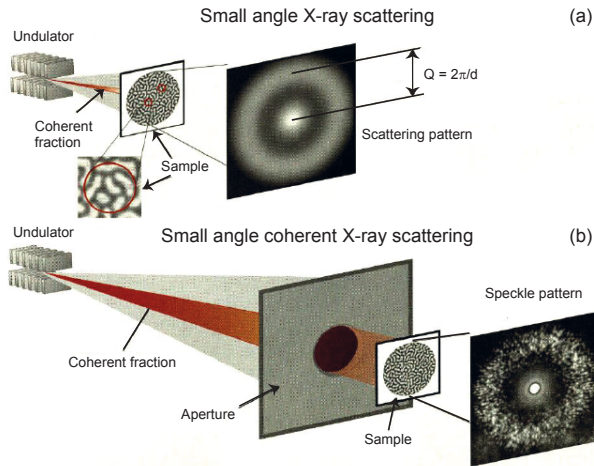


Figure 6.1: The illumination of a magnetic domain pattern with partially coherent radiation results in a SAXS pattern, which provides the momentum transfer vector. When improving the coherence of the radiation a speckle pattern can be observed. The images are adapted from [31].

Moreover, dynamical changes of the scattering centers can be observed in the speckle pattern, as explained in [153]. This technique is known as photon correlation spectroscopy (PCS), also called dynamic light scattering (DLS), where the correlation among the scattered

photons is analyzed in the time-domain. PCS allows studies of dynamical processes over a very broad frequency region, ranging from 10^{-3} Hz to 10^6 Hz (corresponding to a timescale spanning from hours to microseconds). The corresponding technique using coherent X-rays, which is consequently named XPCS, provides the possibility to study intensity fluctuations at large Q -vectors (10^{-3} \AA^{-1} up to several \AA^{-1}), addressing object sizes in the range of several hundreds of nanometers to Ångströms.

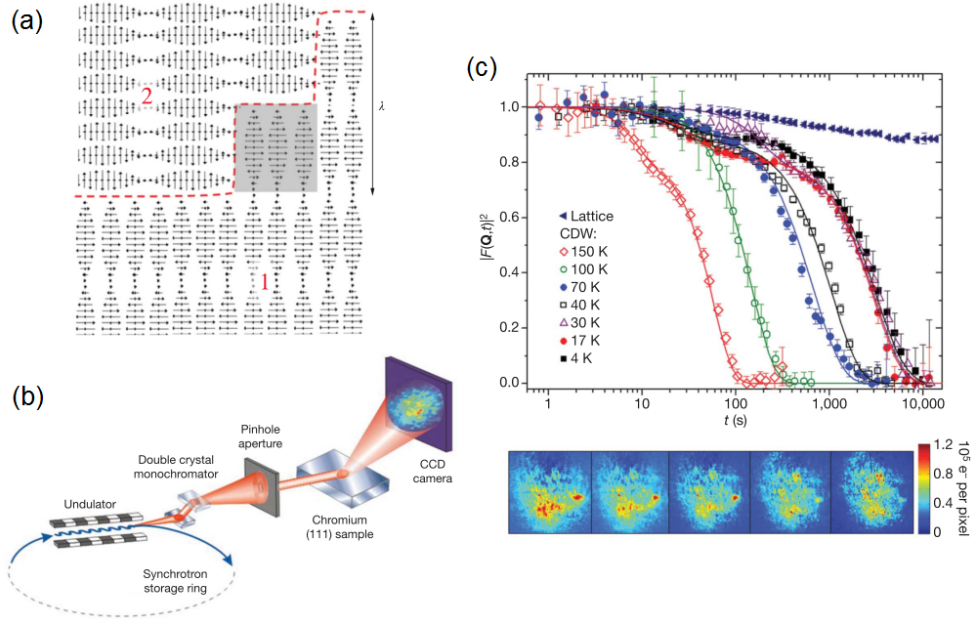


Figure 6.2: Schematic illustration of the magnetic structure in Cr (a). The two regions indicate two perpendicular SDWs and the red dashed line marks the domain wall separating the two regions. The experimental setup is sketched in (b). Speckle images related to the CDW superlattice are shown in (c) for $T = 17$ K and the time-dependent evolution of the autocorrelation intensity $F(Q, t)$ is plotted for various temperatures. All images are taken from [154].

In addition, it has been demonstrated that field-induced changes of magnetic domains can be studied by recording speckle patterns [154–156]. Shpyrko *et al.* presented a very interesting application of XPCS [154] by studying the antiferromagnetic state of Chromium, where the magnetic moment of a certain Cr atom is oriented antiparallel to the magnetic moments of the nearest neighbors. As illustrated in Fig.6.2(a), sinusoidal modulations of

the magnetic structure (with a wavelength of 6–8 nm) occur at temperatures lower than the Néel temperature of bulk Cr, which is about 311 K. They are known as spin density waves (SDW), which are accompanied by charge density waves (CDW).

Figure 6.2(b) shows the experimental setup, where synchrotron radiation is reflected from a Chromium (111) sample. The recorded speckle patterns can be related to the CDW superlattice and dynamical processes are investigated by calculating the (second order) intensity correlation function $g_2(t)$, which is given by

$$g_2(t) = \frac{\langle I(\tau)I(\tau+t) \rangle}{\langle I(\tau) \rangle^2} = 1 + A |F(\mathbf{Q}, t)|^2 = 1 + \beta(\mathbf{Q}) |f(\mathbf{Q}, t)|^2, \quad (6.1)$$

where $f(\mathbf{Q}, t) = F(\mathbf{Q}, t)/F(\mathbf{Q}, 0)$ denotes the normalized intermediate scattering function. The brackets $\langle \rangle$ stand for an ensemble average and $\beta(\mathbf{Q})$ is the speckle contrast, which depends on the light coherence. Figure 6.2(c) shows a time sequence of magnetic speckle patterns recorded at 17 K, where domain fluctuations reduce the correlation between the different images. This corresponds to decrease of $|F(\mathbf{Q}, t)|^2$ for increasing t , as presented in the plot above. Strikingly, the domain fluctuation time increases for lower temperatures. This has been associated to switching processes, which are described by a thermal activation model at elevated temperatures and by quantum tunneling at low temperatures. In addition it is remarkable that the presented XPCS analysis allows to probe the disorder of a magnetic system at fundamental length scales over many decades in time.

Equation 6.1 demonstrates that PCS (and XPCS) studies are only possible if $\beta > 0$. Therefore, it is explained in the following how the properties of the HHG radiation influence the speckle contrast, which is essential for PCS experiments using laboratory XUV light.

6.2 SAXS from Fe and FePd Grains

6.2.1 Sample Fabrication

In order to test the capabilities of the SAXS setup, it is necessary to design samples that contain scattering objects, which have a high scattering probability and a suitable size. For this purpose $\text{Fe}_{50}\text{Pd}_{50}$ and Fe films were annealed in air at 600°C for 4 h. It has been demonstrated elsewhere that the annealing of Fe films results in the formation of isolated iron oxide nanoparticles [157]. Very likely, a similar oxidation effect occurs for the $\text{Fe}_{50}\text{Pd}_{50}$ alloy, which is 20 nm thick and was grown by MBE on a 50 nm thick Si_3N_4 membrane. The 4 nm thin Fe film was evaporated onto an identical substrate. AFM images (Fig. 6.3) of these films reveal a pronounced island formation after the annealing.

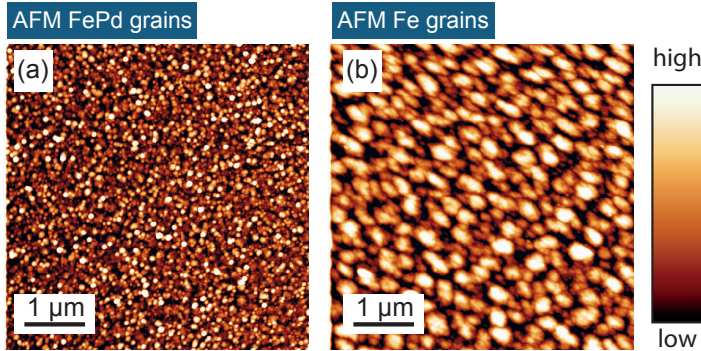


Figure 6.3: AFM images of $\text{Fe}_{50}\text{Pd}_{50}$ (a) and Fe films (b) after annealing in air at 600°C for 4 h.

For both materials, islands on the submicron-scale are observed, where the average size can be influenced by the layer thickness, the annealing time and the temperature. The SAXS measurements presented in the following focus on two samples, which were prepared in the same way as the specimens presented in Fig. 6.3.

6.2.2 Experimental Setup

The scattering images are taken with the tabletop RMS setup introduced in Chapter 5. The sample is placed 7 cm upstream the CCD detector (Andor, Newton 920, 1024×255 pixels of $26 \times 26 \mu\text{m}^2$). The main difference compared to the RMS measurements shown in Chapter 5 is the XUV spectrum, which is centered at lower energies (30–60 eV) for the SAXS measurements of the Fe and FePd grains. There are two reasons for this choice: first,

the charge scattering amplitude for XUV light is far larger than the magnetic scattering amplitude and, consequently, it is redundant to tune the XUV radiation to any particular absorption edge. Second, photons in this energy range can be created more efficiently with argon instead of neon gas, yielding a more than 10 times higher photon flux, originating for instance from the lower ionization potential of the argon atoms and from the achievable phase matching conditions. Figure 6.4 shows XUV spectra, recorded with a transmission grating. The full XUV spectrum (red) was recorded with a toroidal Au mirror at grazing incidence and the monochromatized spectrum (blue) was measured with a Bragg mirror pair, designed to select 42 eV radiation.

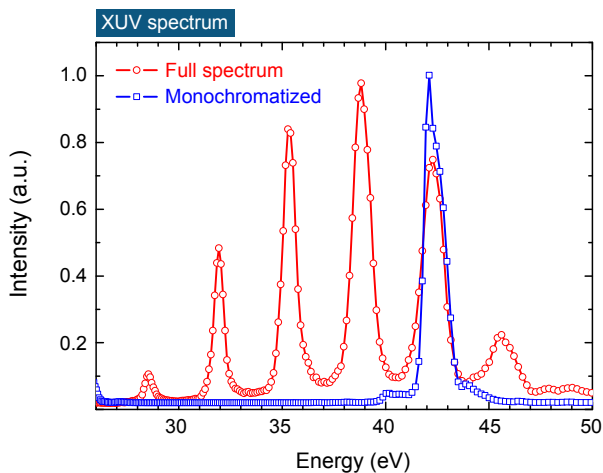


Figure 6.4: Comparison of the full XUV spectrum measured with a toroidal Au mirror (red) and the monochromatized spectrum taken with a Bragg mirror pair (blue).

The Bragg mirror pair selects the 27th harmonic order located at 42.9 eV and the spectral width of a single harmonic is about 1 eV. As the resolution of the spectrometer (introduced in section 5.2.2) is limited, for instance by the size of the XUV spot on the detector, 1 eV is the upper limit of the real bandwidth.

6.2.3 Results and Discussion

SAXS images of the FePd grains taken with the monochromatized radiation (Bragg mirrors) and with the full spectrum (toroidal mirror) are shown in the upper row of Fig. 6.5, while the lower row displays the scattering from the FePd and Fe grains, recorded with the Bragg mirrors. All images reveal scattering rings, reflecting the random distribution of the scattering centers. The diameter of the rings depends on the average distance between the grains and consequently on the grain size. Additionally, the different images show specific speckle patterns, which are analyzed below.

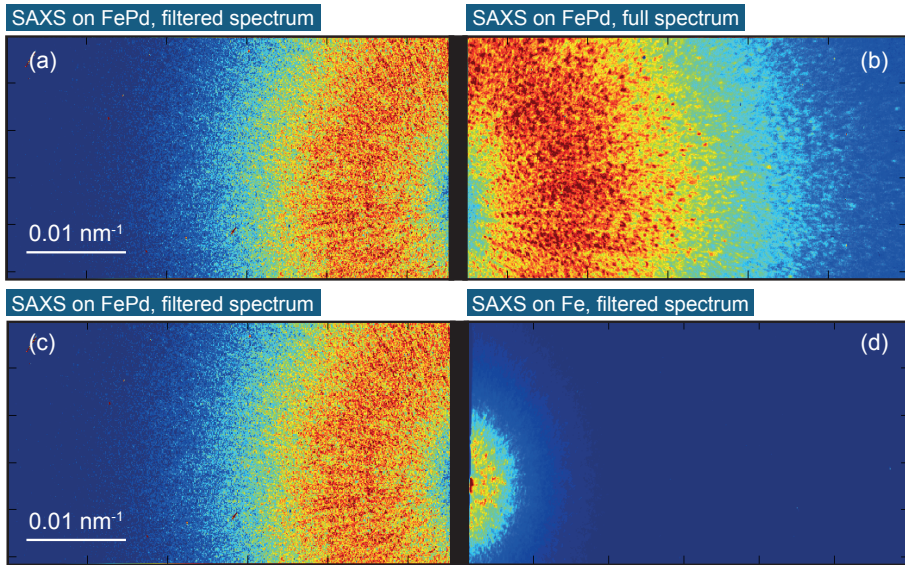


Figure 6.5: The upper row shows the SAXS images from the FePd grains, measured with the Bragg mirrors (a) and with the toroidal Au mirror (b). The lower row contains the scattering pictures for the FePd (c) and Fe grains (d). Both samples were illuminated with monochromatized light filtered with the Bragg mirrors. Note that (a) and (c) show the same image for a better comparison of all measurements and for all images the detector signal was integrated over 15 minutes.

For a comparison of the different scattering image, the corresponding intensity is radially integrated and is plotted against the momentum transfer vector in Fig. 6.6. Q depends on the wavelength, which is not well defined, when the full XUV spectrum is used for the SAXS experiment. Therefore, the Q -axis is identical for both measurements (Bragg mirror pair and

toroidal mirror) to allow an easy comparison. Q is given by $Q = 4\pi/\lambda \sin[0.5 \arctan(r/D)]$, where r is the radial distance to the transmitted beam, $D = 7$ cm and $\lambda = 28.9$ nm. The radial integrations of the scattering data measured with the Bragg mirrors (left graph of Fig. 6.6) shows that the Fe sample (black line) scatters far more efficiently than the FePd layer (blue line). In detail, the total integrated intensity of the light scattered at the FePd grains is about 9% of the Fe scattering signal. This difference is mainly caused by the transmission difference at 43 eV for the 4 nm thick Fe layer ($T_{Fe} = 0.85$) and the 20 nm thick FePd layer ($T_{FePd} = 0.23$), which is approximately 27% (T_{FePd}/T_{Fe}). At the same time, the grain size distribution is narrower for the Fe film, which is reflected by the narrower peak of the normalized scattering curve (right graph of Fig. 6.6). This can strongly increase the scattering efficiency.

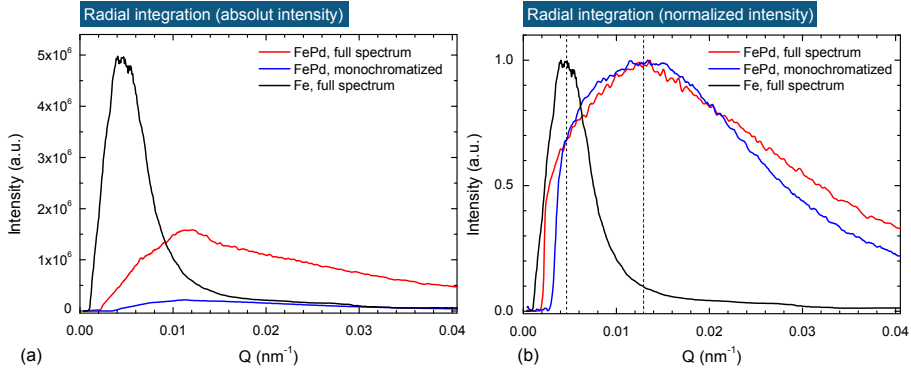


Figure 6.6: Radial integrated intensity of the scattering images shown in Fig. 6.5(a). In (b) the scattering curves are normalized to their maximum and the dashed lines indicate the peak centers at $Q = 0.0045$ nm⁻¹ (black line) and $Q = 0.013$ nm⁻¹ (blue line).

Compared with the scattering of the monochromatized radiation [blue curve in Fig. 6.6(a)], the full spectrum (red curve) yields higher intensities, because the full XUV spectrum contains several harmonic orders and all of them can contribute to the scattering signal. The total intensity difference between both measurements is approximately a factor of 8. The different signal intensities originate from the different XUV spectra (Fig. 6.4) and the transmission difference between the two sets of optics (as described in Chapter 5.2). In total, the expected difference in the intensity is about a factor of 17, which might be overestimated, because any clipping of the XUV beam on the grazing incidence optics is disregarded for the estimation.

The average distance between the scattering centers can be extracted from the position of the peak center, which amounts to 0.0045 nm^{-1} (0.013 nm^{-1}) for the Fe (FePd) film, as shown in Fig. 6.6(b). These values correspond to real-space distances of about $1.4 \mu\text{m}$ and 500 nm , respectively. The average distances between the grains of the Fe and FePd samples which have been investigated by AFM in Fig. 6.3 are slightly smaller. This discrepancy is potentially caused by minor preparation differences and is irrelevant at this point. In general, both measurements AFM and SAXS show that the dimension of the grains is very different for both materials, where the Fe film apparently forms larger islands, which is probably also related to the different thicknesses of the Fe and FePd films.

It is remarkable that the normalized scattering curves obtained with the monochromatized and full spectrum are very similar [Fig. 6.6(b)]. Therefore, the smearing of the radially integrated intensity introduced by the toroidal mirror is relatively small and the width of the scattering curve reflects the size distribution of the grains.

In the following the observed speckle patterns are analyzed in more detail. The illumination of the FePd film with the full XUV spectrum [Fig. 6.5(b)] results in reproductions of the speckle pattern at different Q -values, according to the spacing of the different harmonic orders. However, the high intensity provided by the full XUV spectrum yields a well discernible speckle structure.

In order to give a quantitative analysis and to link the images to the coherence properties of the HHG source, the speckle contrast β is calculated. β is given by the normalized variance of the intensity, *i.e.*, $\beta = \sqrt{\text{Var}(I)} / \langle I \rangle$, and it is analyzed for a region of the diffraction pattern, which exhibits an uniform mean intensity $\langle I \rangle$. This is necessary, because strong variations of the mean intensity (which are not related to the speckle pattern) can also introduce a high variance of the intensity.

β is furthermore connected with the number of modes M via $\beta = 1/\sqrt{M}$. If a sample is illuminated with partially coherent or incoherent radiation, one can divide the illuminated volume into M elements with the size of the coherence volume. The detector measures consequently the sum of M independent speckle patterns [153, 158].

Within the range of $Q = (0.0178 \pm 0.0016) \text{ nm}^{-1}$ the contrast equals 0.16 for the Bragg mirrors. The speckle pattern taken with the toroidal mirror shows a contrast of 0.12 within a range of $Q = (0.0242 \pm 0.0016) \text{ nm}^{-1}$. This region is shaded gray in Fig. 6.7(a), which displays the speckle pattern of the FePd film measured with the toroidal mirror. The analysis of different regions in the Q -space, for example the green square marked in Fig. 6.7(a), yields very similar results, regarding the contrast and the number of modes M .

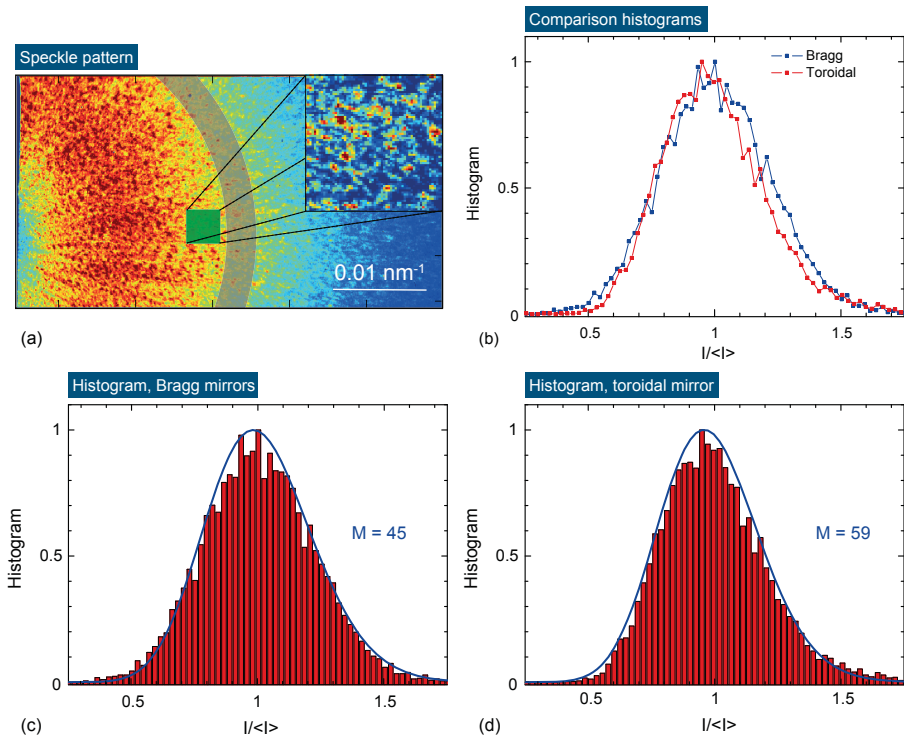


Figure 6.7: The speckle pattern of the FePd film recorded with the toroidal mirror is shown in (a). Note that this is the same image as presented in Fig. 6.5(b). The gray shaded region corresponds to $Q = (0.0243 \pm 0.0016) \text{ nm}^{-1}$. The inset shows a zoom of the green shaded square. In (b) the histograms of the scattering intensity for $Q = (0.0178 \pm 0.0016) \text{ nm}^{-1}$ and $Q = (0.0243 \pm 0.0016) \text{ nm}^{-1}$ are shown, when using the Bragg mirror pair and the toroidal mirror, respectively. In (c) and (d) both histograms are presented separately, where the blue solid lines are fits using equation 6.2.

The low contrast suggests moderate coherence properties of the HHG source, because for a fully coherent light source a contrast of 1 is expected, while the contrast approaches zero, if the light source is incoherent. Detailed considerations related to the speckle contrast are given in section 6.2.4.

Please note that the integration time of 15 min needs to be taken into account for the evaluation of the observed speckle pattern, because 2.7 million exposures with XUV light are averaged during this time period and any movement of the sample (caused by vibrations) will reduce the contrast. In comparison, when studying magnetic speckles with soft X-rays from a free-electron laser a comparable speckle contrast of 0.2 has been reported in [159]. In this case, the speckle pattern was a sum of 1000 pulses with a repetition rate of 10 Hz, corresponding to a total integration time of 100 s.

Further information about the degree of coherence can be obtained by analyzing the histogram of the speckle pattern to link the intensity probability function $p(I)$ with the number of modes M . This function can be expressed by

$$p(I) = \frac{\Gamma(I+M)}{\Gamma(M)\Gamma(I+1)} \left(1 + \frac{M}{I}\right)^{-I} \left(1 + \frac{\langle I \rangle}{M}\right)^{-M}, \quad (6.2)$$

where Γ denotes the gamma function [158]. Figure 6.7(b) shows the histograms for the speckle patterns taken with the monochromatized and full spectrum for the Q -regions mentioned above. In (c) and (d) these histograms are plotted separately, including fits using equation 6.2. The parameter M is extracted from the fit, yielding $M = 45 \pm 3$ for the filtered spectrum and $M = 59 \pm 4$ for the full spectrum. The contrast β can be calculated employing the relation $\beta = 1/\sqrt{M}$. The resulting contrast amounts to 0.149 ± 0.007 and 0.130 ± 0.005 , respectively, which is in agreement with the values mentioned above.

Although sample vibrations influence this experiment, the moderate speckle contrast may be surprising, because very good coherence properties of HHG sources have been reported before [34]. However, it is necessary to distinguish between transverse and longitudinal coherence, because both determine the visibility of an interference pattern. The influence of these quantities depends on the experiment. For instance, in a double-slit experiment mainly the transverse coherence length is important, while the impact of the longitudinal coherence length is comparably small. This changes, when the contrast of a speckle pattern is studied, as it is explained in the following.

6.2.4 Coherence and Speckle Contrast Considerations

To clarify the difference between the transverse and longitudinal coherence in diffraction experiments, interferogram images of an XUV beam diffracted by a Young's double-slit were calculated, depending on the degree of transverse coherence μ_{12} (Fig. 6.8). As described in Ref. [160], the intensity profile $I(x)$ of such interference patterns can be calculated using

$$I(x) = I_0 \left(\frac{\sin(\pi\alpha x/\lambda z)}{\pi\alpha x/\lambda z} \right)^2 \left[1 + \mu_{12} \left(\frac{\sin(\pi\Delta\lambda x/\lambda z)}{\pi\Delta\lambda x/\lambda z} \right) \left(\frac{\sin(\pi\delta\beta/\lambda z)}{\pi\delta\beta/\lambda z} \right) \cos \left(\frac{2\pi\beta x}{\lambda z} \right) \right], \quad (6.3)$$

where I_0 denotes the central intensity, λ the wavelength, $\Delta\lambda$ the spectral bandwidth, α the slit width, β the distance between the two slits, z the distance between slit and detector, and δ the resolution of the detector.

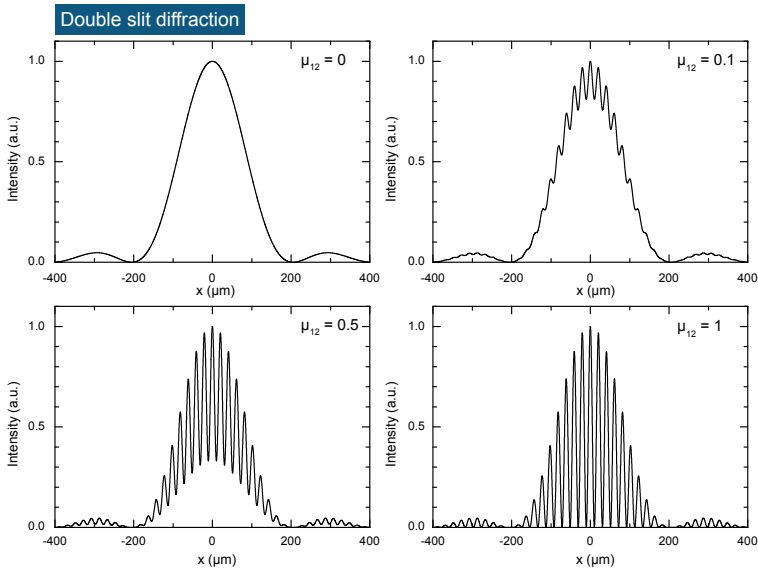


Figure 6.8: Interferogram images calculated for a double slit, while μ_{12} equals 0 in (a), 0.1 in (b), 0.5 in (c) and 1 in (d). The following parameters have been used: $I_0 = 1$, $\lambda = 29.5$ nm, $\Delta\lambda = 0.7$ nm, $\alpha = 100$ nm, $\beta = 1$ μm , $z = 70$ cm and $\delta = 1$ μm .

When the electromagnetic waves emerging from the individual slits have no phase relation ($\mu_{12} = 0$), the intensity profile is determined by the diffraction pattern of a single slit [Fig. 6.8(a)]. For increasing degree of coherence fringes become visible, where the contrast depends on μ_{12} [Figs. 6.8(a), (b) and (c)]. The spectral bandwidth is taken into account by the term

$$\left(\frac{\sin(\pi \Delta \lambda x / \lambda z)}{\pi \Delta \lambda x / \lambda z} \right),$$

which is close to one, as $\Delta \lambda x \ll \lambda z$ and $\lim_{x \rightarrow 0} \{\sin(x)/x\} = 1$. Therefore, the influence of the bandwidth of the XUV spectrum has only little impact on the interference pattern, especially when considering the parameters of the HHG radiation used in our experiment ($\lambda=29.5$ nm, $\Delta\lambda=0.7$ nm). These parameters were also used to calculate the curves in Fig. 6.8.

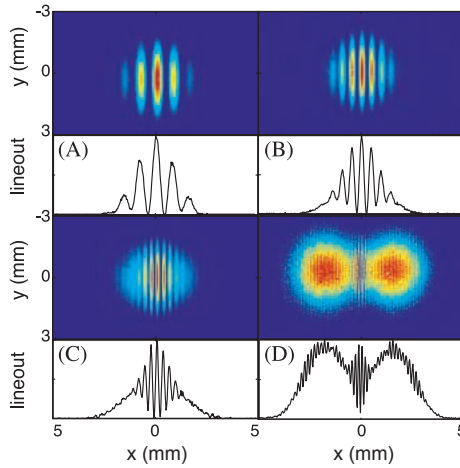


Figure 6.9: Interferogram images measured by diffraction of HHG radiation from a pinhole pair (each with a diameter of $50 \mu\text{m}$) and the corresponding lineouts are presented for different hole separations, *i.e.*, $142 \mu\text{m}$ in (A), $242 \mu\text{m}$ in (B), $384 \mu\text{m}$ in (C) and $779 \mu\text{m}$ in (D). The distance between the pinhole pair and the camera was 2.85 m [161].

Such coherence experiments have been presented by Bartels *et al.* by employing double pinholes [161]. Diffraction patterns for different pinhole separations are given in Fig. 6.9. The XUV radiation used in the latter experiment was centered at 31 eV and in total four harmonic orders separated by 3.2 eV contributed to the spectrum. As mentioned in [161],

the broad spectral bandwidth may reduce the visibility of the fringes, but the high visibility of the diffraction patterns in Fig. 6.9 confirms the negligible influence of the bandwidth, as explained above for the calculated double-slit diffraction.

When analyzing a speckle pattern, the contrast β depends on both the transverse and longitudinal coherence length and is given by $\beta^2 = \beta_z \cdot \beta_r$ [162], where β_z and β_r can be calculated in the Fraunhofer limit by

$$\begin{aligned} \beta_z &= \left(\frac{\epsilon}{\sigma}\right)^2 \left[\frac{\sigma}{\epsilon} \pi^{1/2} \operatorname{erf}\left(\frac{\sigma}{\epsilon}\right) + \exp\left(-\frac{\epsilon^2}{\sigma^2}\right) - 1 \right] \quad \text{and} \\ \beta_r &= \frac{2}{\sigma^2 W^2} \int_0^\sigma dx(\sigma - x) \int_0^W dy(W - y) \exp\left(-\frac{x^2}{\epsilon^2}\right) \\ &\quad \times [\exp(-|Ax + By|) + \exp(-|Ax - By|)]. \end{aligned} \quad (6.4)$$

$k = 2\pi/\lambda$ denotes the wave vector of the incoming light, W the sample thickness, σ the beam diameter and ϵ the transverse coherence length. A and B are given by $A = 2(\Delta\lambda/\lambda)Q(1 - Q^2/(2k)^2)^{1/2}$ and $B = -(\Delta\lambda/\lambda)(Q^2/k)$.

Equation 6.4 is only valid under several assumptions, which are described in detail in [162]. The assumptions demand for instance that the spatial intensity distribution is Gaussian and the spectrum of the radiation is Lorentzian, which is not necessarily fulfilled by the HHG radiation. However, it is reasonable to discuss the impact of the individual parameters affecting the speckle contrast.

The parameters with the strongest influence on β are the beam spot diameter σ , the transverse coherence length ϵ and the longitudinal coherence length l_c , which depends on the bandwidth $\Delta\lambda$ of the radiation and is given by $\lambda^2/(\pi\Delta\lambda)$ for a Lorentzian spectrum. In Table 6.1 these parameters are varied separately, while the rest is kept constant, *i.e.*, $\lambda = 28.9$ nm, $W = 40$ nm. For the generated XUV radiation the following conditions can be assumed: $\sigma = 40$ μ m, $\Delta\lambda = 0.6$ nm, $\lambda = 28.9$ nm, $\epsilon \approx \sigma$ and $Q = 0.024$ nm⁻¹. This situation is presented in the first row of Table 6.1 and yields a contrast of 0.22, which is slightly higher than the experimentally observed value for β (0.16 for the monochromatized XUV light). The contrast is expected to increase, if $\Delta\lambda$ decreases. For $\Delta\lambda = 0.003$ nm, implying that $\Delta\lambda/\lambda$ is 10^{-4} , the contrast is limited by β_z , which mainly depends on the transverse coherence length ϵ , as demonstrated in Table 6.1. A reduction of ϵ below the beam diameter results in a decrease of the contrast.

Furthermore, it becomes clear that a smaller beam diameter σ can significantly improve the contrast. A high contrast ($\beta > 0.7$) can be achieved by focusing to 1 μ m or better.

In conclusion, the experimentally observed speckle contrast is in agreement with the calculations. Moreover, the contrast is limited by the relative bandwidth of the radiation and the spot size on the sample.

Table 6.1: Influence of the bandwidth $\Delta\lambda$, the transverse coherence length ϵ and the beam diameter σ on the speckle contrast $\beta = \sqrt{\beta_z \cdot \beta_r}$.

$\epsilon = \sigma$ $\sigma = 40\mu\text{m}$	$\Delta\lambda(\text{nm})$	β_z	$(\beta_z\beta_r)^{1/2}$
$\Delta\lambda$	0.6	0.86	0.22
	0.2	0.86	0.34
	0.003	0.86	0.84
$\sigma = 40\mu\text{m}$ $\Delta\lambda = 0.6\text{nm}$	ϵ	β_z	$(\beta_z\beta_r)^{1/2}$
ϵ	10σ	1	0.23
	2σ	0.96	0.23
	$\sigma/2$	0.64	0.18
	$\sigma/5$	0.31	0.13
$\sigma = \epsilon$ $\Delta\lambda = 0.6\text{nm}$	$\sigma(\mu\text{m})$	β_z	$(\beta_z\beta_r)^{1/2}$
σ	100	0.86	0.19
	10	0.86	0.39
	1	0.86	0.75

In the following section, a diffraction experiment is presented, which takes advantage of the good transverse coherence properties of the HHG radiation.

6.3 Knife-Edge Diffraction

6.3.1 Experimental Setup

Light diffraction at an edge is an optical effect, which can be employed to determine the real part of the refractive index n of a transparent sample, as described in Ref. [163]. Typically, the imaginary part of n is measured in an absorption experiment and the real part is calculated using the Kramers-Kronig relation. A direct measurement of the real part can be achieved by diffracting the light at a transparent half-plane, as illustrated in Fig. 6.10.

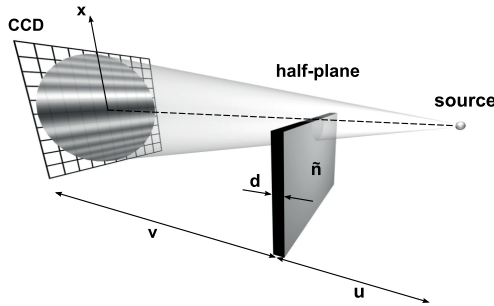


Figure 6.10: Schematics of an edge-diffraction experiment. Soft X-rays from a laser-plasma source illuminates a transparent half-plane and the resulting diffraction pattern is recorded with a CCD camera. The pattern is calculated for a plane with a transmission of 80% and $\Delta\phi = \pi$ [163].

In Ref. [163] soft X-rays from a laser-produced plasma illuminate a transparent sample, which covers partially the beam profile at a distance u behind the source, while a detector (in this case a CCD camera) records the interference pattern at the distance $v+u$. If the half-plane is opaque, the interference pattern in the shadow region ($x < 0$) vanishes. For a transparent half-plane a certain phase shift in the interference pattern can be observed, given by $\Delta\phi = 2\pi\delta d/\lambda$, where δ denotes the real part of the refractive index ($n = 1 - \delta + i\beta$), λ the wavelength and d the sample thickness. This technique is promising for time-resolved measurements, when a ferromagnetic film is pumped with ultrashort intense laser-pulses, triggering a demagnetization process. Ultrafast changes of the refractive index induced by laser exposure have been discussed in [164] and knife-edge diffraction could be employed to address related effects involving the real part of the refractive index.

The visibility of the fringes depends strongly on the degree of transverse coherence, which is very limited for a laser-produced plasma [163, 165]. The longitudinal coherence is far better for a plasma source compared with a HHG source, as $\Delta\lambda/\lambda$ equals 6×10^{-4} for the

Al K_α -radiation created with the plasma source, whereas $\Delta\lambda/\lambda$ is approximately 2.1×10^{-2} for the HHG radiation. Nevertheless, as mentioned in [163], the visibility of the fringes is unaffected by the longitudinal coherence, if $\Delta\lambda/\lambda < 10^{-1}$, which holds for both light sources. In order to study the feasibility of such experiments using a HHG source, interference patterns have been recorded using an opaque knife edge, providing strongest contrast. The HHG beam is focused and monochromatized (42.9 eV) with the Bragg mirrors. The distance between the focal plane and the knife edge u is about 3.8 cm and the distance between the blade and the CCD sensor v is 29.5 cm.

6.3.2 Results and Discussion

Figure 6.11(a) shows the resulting diffraction pattern after averaging 10 images, each integrated for 0.5 s. As the HHG beam is significantly expanded on the CCD sensor (to approximately 1 cm in diameter), the interference pattern is superimposed onto the beam profile. Therefore, an image taken with the full beam (without the knife edge) is subtracted as background (comparable with a flat-field correction) to enhance the visibility of the fringes.

The resulting profiles, summed over the y -axis of the images, are given in Fig. 6.12. The illuminated part of the CCD camera clearly shows fringes modulating the beam profile, visible in both the raw data (a) and the background corrected image (b). In order to remove the residual background modulating the interference pattern, a smoothed trendline [red curve in Fig. 6.12(b)] is subtracted from the profile. This treatment is conducted to allow a better comparison with calculations, as demonstrated in the following, but it is not used for a fit to the data. The obtained data points are shown as open circles in (c) and (d). The intensity of the diffraction pattern can be calculated by

$$I(\omega) = \frac{I_0}{2} [(1/2 + C(\omega))^2 + (1/2 + S(\omega))^2]. \quad (6.5)$$

ω is a dimensionless coordinate given by $\omega = x(u/(u+v))[2/\lambda(1/u + 1/v)]^{1/2}$ [163] and I_0 denotes the incoming light intensity. $C(\omega)$ and $S(\omega)$ are the Fresnel integrals [165, 166], which can be derived by

$$C(\omega) = \int_0^\omega \cos\left(\frac{\pi}{2}s^2\right) ds \quad \text{and} \quad S(\omega) = \int_0^\omega \sin\left(\frac{\pi}{2}s^2\right) ds. \quad (6.6)$$

Figure 6.12(c) compares qualitatively the experimentally observed fringes and the calculated diffracted intensity (red curve). The simulated curve can nicely reproduce the position of

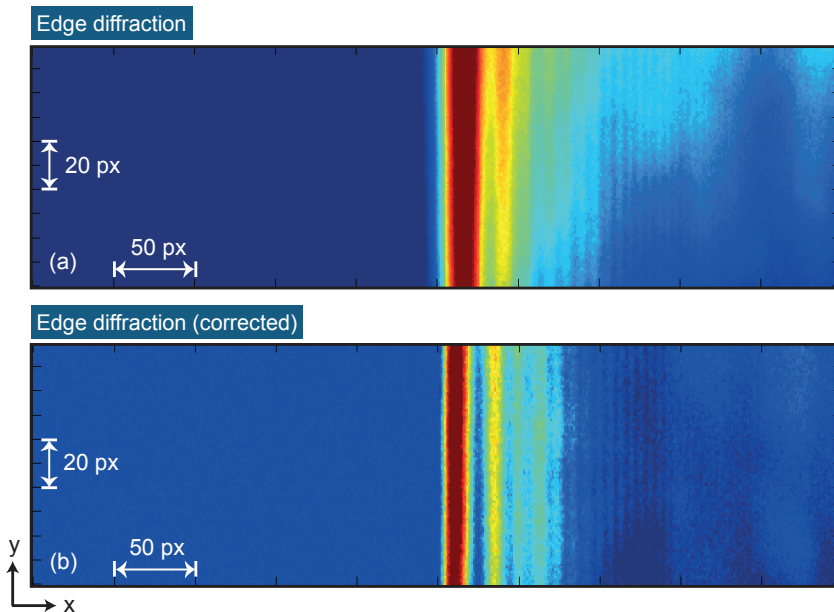


Figure 6.11: Diffraction pattern obtained by diffracting the HHG radiation at a knife edge. The raw image is presented in (a) and a background corrected image in (b).

the individual fringes, which depends strongly on the parameter u , v and λ . For increasing diffraction order the envelope of the measured fringes decreases faster than the simulated intensity. This results from the finite beam size, as equation 6.5 is only valid for a point source. Therefore, the calculated intensity curve is convoluted with a Gaussian function to take into account the beam diameter, which is approximately $90 \mu\text{m}$ for the used mirror pair (determined by moving the knife edge through the focus). The blue curve in (d) is the result of a convolution of the red curve in (c) with a Gaussian function with a FWHM of $90 \mu\text{m}$. The convoluted simulation is in reasonable agreement with the experimentally observed diffraction pattern. Thus, the reduced amplitude of the oscillation amplitude of the fringes is mainly a consequence of the finite beam size. Conclusively, the high transverse coherence of the HHG radiation allows the detection of 14 fringes, which is far more than it has been reported for laser-based plasma sources, *e.g.*, Boschetto *et al.* observed three diffraction fringes [165].

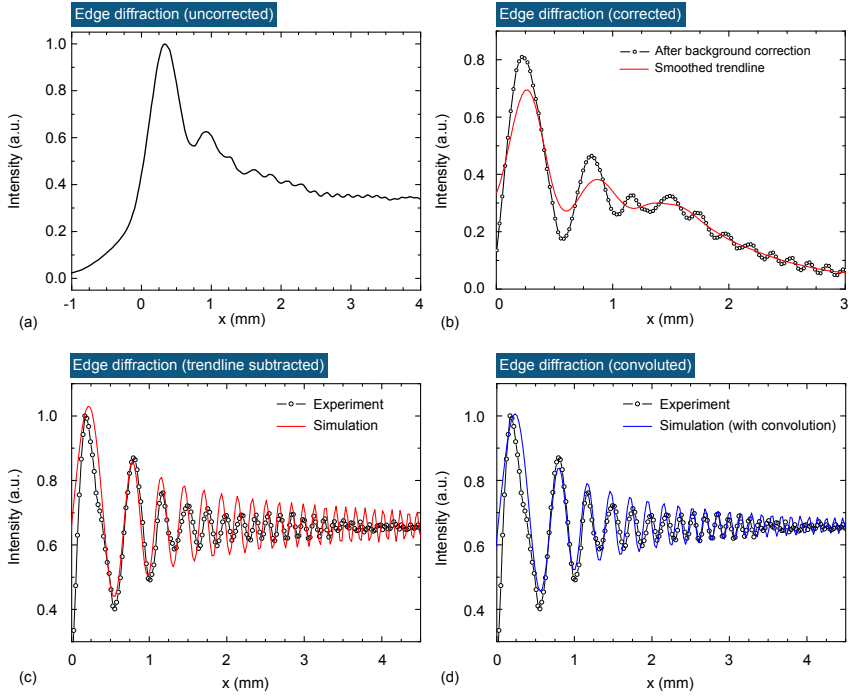


Figure 6.12: Profiles of the diffraction patterns along the x axis are shown in Fig. 6.11. The lineouts given in (a) and (b) are taken from uncorrected and background corrected image, respectively. The red solid curve in (b) is a trendline of the experimental data (open circles), which was obtained by smoothing. The difference between the data points and the smoothed trend line is shown in (c) as open circles and compared with a simulation, which has been calculated by using equation 6.5 with $u = 3.8$ cm and $v = 29.5$ cm. For (d) the simulation has been convolved with a Gaussian function.

6.4 Conclusion

It has been demonstrated that the scattering of HHG radiation is a suitable tool to investigate Fe and FePd grains on the nanometer length scale. In contrast to the resonant magnetic scattering experiment described in Chapter 5, bright XUV radiation has been generated in argon gas and intense scattering images have been recorded within a few minutes. Furthermore, the coherent illumination results in a specific speckle pattern, which has been used to analyze the coherence properties of the generated XUV light. The observed speckle contrast is in agreement with the theoretical prediction, taking into account the radiation properties, especially the spectral bandwidth and the beam spot diameter. Although the contrast is limited, the observation of stable speckle patterns over a long time period potentially allows investigations of dynamical processes by photon correlation spectroscopy.

Solid-edge diffraction of XUV light has been studied by illuminating a knife edge. The recorded interference patterns are very close to the simulated diffraction pattern of a fully coherent beam, reflecting the high degree of transverse coherence of the generated light. Consequently, diffraction at a transparent half-plane is a promising experiment for investigating ultrafast changes of the real part of the refractive index. This method can provide further details about the magneto-optical response of a ferromagnetic film in the XUV spectral regime after the illumination with ultrashort laser pulses.

7 Summary and Outlook

In summary, this thesis shows a detailed analysis of magnetic domain patterns of FePd and CoPd alloys. This survey is carried out with X-ray-based resonant magnetic scattering (RMS), providing information about the field-induced changes of magnetic structures with the nanometer resolution. The RMS analysis takes advantage of the element selectivity, thereby enabling examinations of buried magnetic films. Investigations of FePd/CoPd bilayers reveal individually the domain patterns of both layers, which is difficult to accomplish with other techniques. The experimental findings point out that the CoPd layer determines the domain size of the coupled films. This is very likely caused by a strong canting of the FePd easy axis with respect to the sample surface, which in turn reduces the out-of-plane component of the FePd magnetization. This statement is further supported by field-dependent studies and micromagnetic simulations. Additionally, RMS measurements of CoPd/Pd/NiFe trilayers show that the CoPd film creates an out-of-plane pattern in the NiFe layer, which has a strong in-plane anisotropy. The field-dependent analysis of this trilayer emphasizes to possibility of adjusting the relative angle of magnetization between both layers, while conserving the multidomain state. Consequently, both samples are very promising systems for time-resolved examinations of ultrafast demagnetization, which potentially reveal the influence of superdiffusive spin transport and laser-excited spin transfer torques in coupled domain patterns with canted magnetization [27, 30].

The ultrafast demagnetization of the synthesized FePd/CoPd bilayers is investigated by employing femtosecond laser pulses. The detected demagnetization curves show that the laser-induced quenching of the CoPd magnetization does not affect the magnetic coupling of both films. Moreover, first experiments on MgO/Au/CoPd samples demonstrate the feasibility to demagnetize a CoPd layer, although the laser radiation is strongly absorbed by the Au layer. This would be in agreement with the previously published observations involving laser-excited hot electrons [28], but a clear conclusion certainly requires further investigations. Considering the FePd/CoPd bilayer, it would be very interesting to address the question, how the FePd magnetization, the magnetic coupling and the magnetic domains are modified by the optical excitation of the CoPd film.

Such time-resolved studies of the domain evolution triggered by an intense laser pulse demand an ultrashort light source with a sufficiently small wavelength. In this context it is demonstrated that a laser-driven extreme ultraviolet (XUV) light source based on high-order harmonic generation (HHG) is capable to investigate the magnetic domains of Co/Pt multilayer films with RMS at the Co M-edges ($\hbar\omega \approx 60$ eV). Employing this tabletop RMS setup, laser-induced modifications of both the magnetic domain pattern and the sample morphology are compared to atomic and magnetic force microscopy measurements (AFM and MFM). Remarkably, the domain pattern is strongly influenced by intense laser pulses, resulting in permanent and reversible changes of the magnetic structure. The RMS patterns of the laser-exposed sample are dominated by charge scattering originating from laser ablated material. Consequently, the intense laser illumination leads to significant magnetic modifications, which may be investigated in future experiments with femtosecond resolution.

Finally, XUV light is scattered on Fe and FePd grains, demonstrating the possibility to examine nanometer-sized grains with a HHG source in a small-angle X-ray scattering (SAXS) experiment. The scattering images exhibit a substructure, known as speckle pattern, which is linked to the coherence properties of the HHG source. The obtained results show that the speckle contrast, which is essential for applications like photon correlation spectroscopy, is mainly limited by the longitudinal coherence of the XUV radiation. On the other hand, the high transverse coherence of HHG radiation allows a variety of diffraction experiments, as demonstrated in other publications [39, 161]. Thus, solid-edge diffraction of HHG light is presented to investigate the coherence properties of the HHG radiation. Compared with the diffraction experiments conducted with laser-driven plasma sources [163], the HHG source yields far better diffraction patterns due to the high degree of transverse coherence. This thesis should motivate future work which involves time-resolved and element-selective studies of ultrafast demagnetization of coupled magnetic domain patterns. The RMS experiment using a laser-based HHG source is certainly a very challenging task, but the ongoing improvement of these XUV sources will potentially permit to record RMS patterns at different resonance edges within small exposure times. Furthermore, HHG sources may be used for imaging or diffraction experiments like photon correlation spectroscopy, magnetic holography or diffraction at a transparent half-plane to improve our knowledge about magnetization dynamics and laser-induced modifications of magnetic domains.

Bibliography

- [1] C. Chappert, A. Fert, and F. N. Van Dau, “The emergence of spin electronics in data storage.”, *Nat. Mater.* **6**, 813 (2007).
- [2] M. N. Baibich, J. M. Broto, A. Fert, F. N. Van Dau, F. Petroff, P. Etienne, G. Creuzet, A. Friederich, and J. Chazelas, “Giant Magnetoresistance of (001)Fe/(001)Cr Magnetic Superlattices”, *Phys. Rev. Lett.* **61**, 2472 (1988).
- [3] G. Binasch, P. Grünberg, F. Saurenbach, and W. Zinn, “Enhanced magnetoresistance in layered magnetic structures with antiferromagnetic interlayer exchange”, *Phys. Rev. B* **39**, 4828(R) (1989).
- [4] D. Weller and A. Moser, “Thermal Effect Limits in Ultrahigh-Density Magnetic Recording”, *IEEE T. Magn.* **35**, 4423 (1999).
- [5] G. W. Fernando, *Metallic Multilayers and their Applications*, (Elsevier Science 2008).
- [6] O. Hellwig, G. Denbeaux, J. Kortright, and E. E. Fullerton, “X-ray studies of aligned magnetic stripe domains in perpendicular multilayers”, *Physica B* **336**, 136 (2003).
- [7] D. Stickler, R. Frömter, H. Stillrich, C. Menk, H. P. Oepen, C. Gutt, S. Streit-Nierobisch, L.-M. Stadler, G. Grübel, C. Tieg, and F. Yakhou-Harris, “Domain size in systems with canted magnetization”, *Phys. Rev. B* **84**, 104412 (2011).
- [8] R. Frömter, H. Stillrich, C. Menk, and H. P. Oepen, “Imaging the Cone State of the Spin Reorientation Transition”, *Phys. Rev. Lett.* **100**, 207202 (2008).
- [9] J. R. Childress, J. L. Duvail, S. Jasmin, A. Barthélémy, A. Fert, A. Schuhl, O. Durand, and P. Galtier, “Perpendicular magnetic anisotropy in $\text{Co}_x\text{Pd}_{1-x}$ alloy films grown by molecular beam epitaxy”, *J. Appl. Phys.* **75**, 6412 (1994).
- [10] C. Morgan, K. Schmalbuch, F. García-Sánchez, C. M. Schneider, and C. Meyer, “Structure and magnetization in CoPd thin films and nanocontacts”, *J. Magn. Magn. Mater.* **325**, 112 (2013).

- [11] A. Moser, K. Takano, D. T. Margulies, M. Albrecht, Y. Sonobe, Y. Ikeda, S. Sun, and E. E. Fullerton, “Magnetic recording: advancing into the future”, *J. Phys. D: Appl. Phys.* **35**, R157 (2002).
- [12] B. Terris, T. Thomson, and G. Hu, “Patterned media for future magnetic data storage”, *Microsyst. Technol.* **13**, 189 (2007).
- [13] P. Grünberg, R. Schreiber, Y. Pang, M. B. Brodsky, and H. Sowers, “Layered Magnetic Structures: Evidence for Antiferromagnetic Coupling of Fe Layers across Cr Interlayers”, *Phys. Rev. Lett.* **57**, 2442 (1986).
- [14] J. S. Moodera, L. R. Kinder, T. M. Wong, and R. Meservey, “Large Magnetoresistance at Room Temperature in Ferromagnetic Thin Film Tunnel Junctions”, *Phys. Rev. Lett.* **74**, 3273 (1995).
- [15] F. J. Albert, J. A. Katine, R. A. Buhrman, and D. C. Ralph, “Spin-polarized current switching of a Co thin film nanomagnet”, *Appl. Phys. Lett.* **77**, 3809 (2000).
- [16] Y. K. Kato, R. C. Myers, A. C. Gossard, and D. D. Awschalom, “Observation of the Spin Hall Effect in Semiconductors”, *Science* **306**, 1910 (2004).
- [17] K. Uchida, S. Takahashi, K. Harii, J. Ieda, W. Koshibae, K. Ando, S. Maekawa, and E. Saitoh, “Observation of the spin Seebeck Effect”, *Nature* **455**, 778 (2008).
- [18] D. A. Allwood, G. Xiong, and R. P. Cowburn, “Writing and erasing data in magnetic domain wall logic systems”, *J. Appl. Phys.* **100**, 123908 (2006).
- [19] M. Levitt, *Spin Dynamics: Basics of Nuclear Magnetic Resonance*, (Wiley 2001).
- [20] A. Kirilyuk, A. V. Kimel, and T. Rasing, “Ultrafast optical manipulation of magnetic order”, *Rev. Mod. Phys.* **82**, 2731 (2010).
- [21] B. Koopmans, J. Ruigrok, F. Dalla Longa, and W. de Jonge, “Unifying Ultrafast Magnetization Dynamics”, *Phys. Rev. Lett.* **95**, 267207 (2005).
- [22] E. Beaupaire, J. Merle, A. Daunois, and J. Bigot, “Ultrafast spin dynamics in ferromagnetic nickel”, *Phys. Rev. Lett.* **76**, 4250 (1996).
- [23] G. M. Müller, J. Walowski, M. Djordjevic, G.-X. Miao, A. Gupta, A. V. Ramos, K. Gehrke, V. Moshnyaga, K. Samwer, J. Schmalhorst, A. Thomas, A. Hütten,

-
- G. Reiss, J. S. Moodera, and M. Münzenberg, “Spin polarization in half-metals probed by femtosecond spin excitation.”, *Nat. Mater.* **8**, 56 (2009).
- [24] G. Malinowski, F. Dalla Longa, J. H. H. Rietjens, P. V. Paluskar, R. Huijink, H. J. M. Swagten, and B. Koopmans, “Control of speed and efficiency of ultrafast demagnetization by direct transfer of spin angular momentum”, *Nat. Phys.* **4**, 855 (2008).
- [25] D. Rudolf, C. La-O-Vorakiat, M. Battiato, R. Adam, J. M. Shaw, E. Turgut, P. Maldonado, S. Mathias, P. Grychtol, H. T. Nembach, T. J. Silva, M. Aeschlimann, H. C. Kapteyn, M. M. Murnane, C. M. Schneider, and P. M. Oppeneer, “Ultrafast magnetization enhancement in metallic multilayers driven by superdiffusive spin current.”, *Nat. Commun.* **3**, 1037 (2012).
- [26] M. Battiato, K. Carva, and P. Oppeneer, “Superdiffusive Spin Transport as a Mechanism of Ultrafast Demagnetization”, *Phys. Rev. Lett.* **105**, 027203 (2010).
- [27] B. Pfau, S. Schaffert, L. Müller, C. Gutt, A. Al-Shemmary, F. Büttner, R. Delaunay, S. Düsterer, S. Flewett, R. Frömter, J. Geilhufe, E. Guehrs, C. Günther, R. Hawaldar, M. Hille, N. Jaouen, A. Kobs, K. Li, J. Mohanty, H. Redlin, W. Schlotter, D. Stickler, R. Treusch, B. Vodungbo, M. Kläui, H. Oepen, J. Lüning, G. Grübel, and S. Eisebitt, “Ultrafast optical demagnetization manipulates nanoscale spin structure in domain walls”, *Nat. Commun.* **3**, 1100 (2012).
- [28] A. Eschenlohr, M. Battiato, P. Maldonado, N. Pontius, T. Kachel, K. Holldack, R. Mitzner, A. Föhlisch, P. M. Oppeneer, and C. Stamm, “Ultrafast spin transport as key to femtosecond demagnetization.”, *Nat. Mater.* **12**, 332 (2013).
- [29] C. E. Graves, A. Reid, T. Wang, B. Wu, S. de Jong, K. Vahaplar, I. Radu, D. P. Bernstein, M. Messerschmidt, L. Müller, R. Coffee, M. Bionta, S. W. Epp, R. Hartmann, N. Kimmel, G. Hauser, A. Hartmann, P. Holl, H. Gorke, J. H. Mentink, A. Tsukamoto, A. Fognini, J. J. Turner, W. F. Schlotter, D. Rolles, H. Soltau, L. Strüder, Y. Acremann, A. V. Kimel, A. Kirilyuk, T. Rasing, J. Stöhr, A. O. Scherz, and H. A. Dürr, “Nanoscale spin reversal by non-local angular momentum transfer following ultrafast laser excitation in ferrimagnetic GdFeCo.”, *Nat. Mater.* **12**, 293 (2013).
- [30] A. J. Schellekens, K. C. Kuiper, R. de Wit, and B. Koopmans, “Ultrafast spin-transfer torque driven by femtosecond pulsed-laser excitation”, *Nat. Commun.* **5**, 4333 (2014).

- [31] J. Stöhr and H. Siegmann, *Magnetism: From Fundamentals to Nanoscale Dynamics*, (Springer 2006).
- [32] J. Kuneš, P. M. Oppeneer, H.-C. Mertins, F. Schäfers, A. Gaupp, W. Gudat, and P. Novák, “X-ray Faraday effect at the $L_{2,3}$ edges of Fe, Co, and Ni: Theory and experiment”, *Phys. Rev. B* **64**, 174417 (2001).
- [33] C. Stamm, T. Kachel, N. Pontius, R. Mitzner, T. Quast, K. Holldack, S. Khan, C. Lupulescu, E. Aziz, M. Wietstruk, H. Dürr, and W. Eberhardt, “Femtosecond modification of electron localization and transfer of angular momentum in nickel”, *Nat. Mater.* **6**, 740 (2007).
- [34] H. C. Kapteyn, M. M. Murnane, and I. P. Christov, “Extreme Nonlinear Optics: Coherent X Rays from Lasers”, *Physics Today* **58** (2005).
- [35] P. Grychtol, *Element-selective and time-resolved magnetic investigations in the extreme ultraviolet range*, Ph.D. thesis, Universität Duisburg-Essen (2011).
- [36] C. La-O-Vorakiat, M. Siemens, M. M. Murnane, H. C. Kapteyn, S. Mathias, M. Aeschlimann, P. Grychtol, R. Adam, C. M. Schneider, J. M. Shaw, H. Nembach, and T. J. Silva, “Ultrafast Demagnetization Dynamics at the M Edges of Magnetic Elements Observed Using a Tabletop High-Harmonic Soft X-Ray Source”, *Phys. Rev. Lett.* **103**, 257402 (2009).
- [37] S. Mathias, C. La-O-Vorakiat, P. Grychtol, P. Granitzka, E. Turgut, J. M. Shaw, R. Adam, H. T. Nembach, M. E. Siemens, S. Eich, C. M. Schneider, T. J. Silva, M. Aeschlimann, M. M. Murnane, and H. C. Kapteyn, “Probing the timescale of the exchange interaction in a ferromagnetic alloy.”, *Proc. Natl. Acad. Sci. USA* **109**, 4792 (2012).
- [38] E. Turgut, C. La-O-Vorakiat, J. M. Shaw, P. Grychtol, H. T. Nembach, D. Rudolf, R. Adam, M. Aeschlimann, C. M. Schneider, T. J. Silva, M. M. Murnane, H. C. Kapteyn, and S. Mathias, “Controlling the Competition between Optically Induced Ultrafast Spin-Flip Scattering and Spin Transport in Magnetic Multilayers”, *Phys. Rev. Lett.* **110**, 197201 (2013).
- [39] M. D. Seaberg, B. Zhang, D. F. Gardner, E. R. Shanblatt, M. M. Murnane, H. C. Kapteyn, and D. E. Adams, “Tabletop nanometer extreme ultraviolet imaging in an extended reflection mode using coherent Fresnel ptychography”, *Optica* **1**, 39 (2014).

-
- [40] C. Gutt, S. Streit-Nierobisch, L.-M. Stadler, B. Pfau, C. M. Günther, R. Könnecke, R. Frömter, A. Kobs, D. Stickler, H. P. Oepen, R. R. Fäustlin, R. Treusch, J. Feldhaus, E. Weckert, I. A. Vartanyants, M. Grunze, A. Rosenhahn, T. Wilhein, S. Eisebitt, and G. Grübel, “Single-pulse resonant magnetic scattering using a soft x-ray free-electron laser”, *Phys. Rev. B* **81**, 100401(R) (2010).
- [41] B. Vodungbo, A. Barszczak Sardinha, J. Gautier, G. Lambert, M. Lozano, S. Sebban, E. Meltchakov, F. Delmotte, V. Lopez-Flores, J. Arabski, C. Boeglin, E. Beaurepaire, R. Delaunay, J. Lüning, and P. Zeitoun, “Table-top resonant magnetic scattering with extreme ultraviolet light from high-order harmonic generation”, *Europhys. Lett.* **94**, 54003 (2011).
- [42] H. Ibach and H. Lüth, *Festkörperphysik: Einführung in die Grundlagen*, (Springer 2002).
- [43] A. Hubert and R. Schäfer, *Magnetic Domains: The Analysis of Magnetic Microstructures*, (Springer 1998).
- [44] R. Gross and A. Marx, *Festkörperphysik*, (Oldenbourg Verlag 2011).
- [45] E. C. Stoner, “Collective Electron Ferromagnetism”, *Proc. R. Soc. London Ser-A* **165**, 372 (1938).
- [46] J. A. Paulus and R. D. Tucker, “Cobalt palladium seeds for thermal treatment of tumors”, *United states patent* 5429583 (1995).
- [47] W. F. Brown, *Magnetostatic Principles in Ferromagnetism*, (North-Holland Publishing Company 1962).
- [48] R. C. O’Handley, *Modern Magnetic Materials: Principles and Applications*, (Wiley-Interscience 1999).
- [49] F. J. A. den Broeder, W. Hoving, and P. J. H. Bloemen, “Magnetic anisotropy of multilayers”, *J. Magn. Magn. Mater.* **93**, 562 (1991).
- [50] Y. Millev and J. Kirschner, “Reorientation transitions in ultrathin ferromagnetic films by thickness- and temperature-driven anisotropy flows”, *Phys. Rev. B* **54**, 4137 (1996).
- [51] H. P. Oepen, Y. T. Millev, and J. Kirschner, “The reorientation transition in Co/Au(111)”, *J. Appl. Phys.* **81**, 5044 (1997).

- [52] H. P. Oepen, M. Speckmann, Y. Millev, and J. Kirschner, “Unified approach to thickness-driven magnetic reorientation transitions”, *Phys. Rev. B* **55**, 2752 (1997).
- [53] H. Stillrich, C. Menk, R. Frömter, and H. P. Oepen, “Magnetic anisotropy and the cone state in Co/Pt multilayer films”, *J. Appl. Phys.* **105**, 07C308 (2009).
- [54] J. A. C. Bland and B. Heinrich, *Ultrathin Magnetic Structures I*, (Springer 1994).
- [55] H. J. G. Draaisma, F. J. A. den Broeder, and W. J. M. de Jonge, “Perpendicular anisotropy in Pd/Co multilayers”, *J. Appl. Phys.* **63**, 3479 (1988).
- [56] C. H. Lee, R. F. C. Farrow, C. J. Lin, E. E. Marinero, and C. J. Chien, “Molecular-beam-epitaxial growth and magnetic properties of Co-Pt superlattices oriented along the [001], [110], and [111] axes of Pt”, *Phys. Rev. B* **42**, 11384(R) (1990).
- [57] S. U. Jen and B. L. Chao, “Magnetostriction of polycrystalline Co-Pd alloys”, *J. Appl. Phys.* **75**, 5667 (1994).
- [58] S. Hashimoto, Y. Ochiai, and K. Aso, “Perpendicular Magnetic Anisotropy in Sputtered CoPd Alloy Films”, *Jpn. J. Appl. Phys.* **28**, 1596 (1989).
- [59] H. Takahashi, S. Tsunashima, S. Iwata, and S. Uchiyama, “Measurement of Magnetostriction Constants in (111)-Oriented Polycrystalline PdCo Alloy and Multilayered Films”, *Jpn. J. Appl. Phys.* **32**, L1328 (1993).
- [60] Y. Matsuo, “Ordered Alloys in the Cobalt-Palladium System”, *J. Phys. Soc. Jpn.* **32**, 972 (1972).
- [61] C. J. Chien, R. F. C. Farrow, C. H. Lee, C. J. Lin, and E. E. Marinero, “High-resolution transmission electron microscopy studies of seeded epitaxial Co/Pt superlattices”, *J. Magn. Magn. Mater.* **93**, 47 (1991).
- [62] R. F. C. Farrow, R. H. Geiss, G. L. Gorman, G. R. Harp, R. F. Marks, and E. E. Marinero, “Large perpendicular-anisotropy, high-coercivity Co-Pt alloys for magneto-optical recording”, *J. Magn. Soc. Jpn.* **17**, Sup. S1 (1993).
- [63] D. Weller, H. Brändle, and C. Chappert, “Relationship between Kerr effect and perpendicular magnetic anisotropy in $\text{Co}_{1-x}\text{Pt}_x$ and $\text{Co}_{1-x}\text{Pd}_x$ alloys”, *J. Magn. Magn. Mater.* **121**, 461 (1993).

-
- [64] D. E. Laughlin, K. Srinivasan, M. Tanase, and L. Wang, “Crystallographic aspects of $L1_0$ magnetic materials”, *Scripta Materialia* **53**, 383 (2005).
- [65] P. Kamp, A. Marty, B. Gilles, R. Hoffmann, S. Marchesini, M. Belakhovsky, C. Boeglin, H. A. Dürr, S. S. Dhesi, G. van der Laan, and A. Rogalev, “Correlation of spin and orbital anisotropies with chemical order in $Fe_{0.5}Pd_{0.5}$ alloy films using magnetic circular x-ray dichroism”, *Phys. Rev. B* **59**, 1105 (1999).
- [66] V. Gehanno, A. Marty, B. Gilles, and Y. Samson, “Magnetic domains in epitaxial ordered $FePd(001)$ thin films with perpendicular magnetic anisotropy”, *Phys. Rev. B* **55**, 12552 (1997).
- [67] V. Gehanno, R. Hoffmann, Y. Samson, A. Marty, and S. Auffret, “In plane to out of plane magnetic reorientation transition in partially ordered $FePd$ thin films”, *Euro. Phys. J. B* **10**, 457 (1999).
- [68] O. Yabuhara, M. Ohtake, K. Tobar, T. Nishiyama, F. Kirino, and M. Futamoto, “Structural and magnetic properties of $FePd$ and $CoPd$ alloy epitaxial thin films grown on MgO single-crystal substrates with different orientations”, *Thin Solid Films* **519**, 8359 (2011).
- [69] M. Ohtake, S. Ouchi, F. Kirino, and M. Futamoto, “Structure and Magnetic Properties of $CoPt$, $CoPd$, $FePt$, and $FePd$ Alloy Thin Films Formed on $MgO(111)$ Substrates”, *IEEE T. Magn.* **48**, 3595 (2012).
- [70] M. Ohtake, S. Ouchi, F. Kirino, and M. Futamoto, “ $L1_0$ ordered phase formation in $FePt$, $FePd$, $CoPt$, and $CoPd$ alloy thin films epitaxially grown on $MgO(001)$ single-crystal substrates”, *J. Appl. Phys.* **111**, 07A708 (2012).
- [71] K. M. Seemann, F. Garcia-Sanchez, F. Kronast, J. Miguel, A. Kákay, C. M. Schneider, R. Hertel, F. Freimuth, Y. Mokrousov, and S. Blügel, “Disentangling the Physical Contributions to the Electrical Resistance in Magnetic Domain Walls: A Multiscale Study”, *Phys. Rev. Lett.* **108**, 077201 (2012).
- [72] J. Miguel, J. F. Peters, O. M. Toulemonde, S. S. Dhesi, N. B. Brookes, and J. B. Goedkoop, “X-ray resonant magnetic scattering study of magnetic stripe domains in a - $GdFe$ thin films”, *Phys. Rev. B* **74**, 094437 (2006).
- [73] C. Kooy and U. Enz, “Experimental and theoretical study of the domain configuration in thin layers of $BaFe_{12}O_{19}$ ”, *Philips Res. Rep.* **15**, 7 (1960).

- [74] J. Cape and G. Lehman, “Magnetic Domain Structures in Thin Uniaxial Plates with Perpendicular Easy Axis”, *J. Appl. Phys.* **42**, 5732 (1971).
- [75] J. Camarero, J. Miguel, J. B. Goedkoop, J. Vogel, F. Romanens, S. Pizzini, F. Garcia, J. Sort, B. Dieny, and N. B. Brookes, “Magnetization reversal, asymmetry, and role of uncompensated spins in perpendicular exchange coupled systems”, *Appl. Phys. Lett.* **89**, 232507 (2006).
- [76] M. W. Muller, “Distribution of the Magnetization in a Ferromagnet”, *Phys. Rev.* **122**, 1485 (1961).
- [77] A. Marty, Y. Samson, B. Gilles, M. Belakhovsky, E. Dudzik, H. Dürr, S. Dhesi, G. van der Laan, and J. B. Goedkoop, “Weak-stripe magnetic domain evolution with an in-plane field in epitaxial FePd thin films: Model versus experimental results”, *J. Appl. Phys.* **87**, 5472 (2000).
- [78] J. Peters, *Resonant soft x-ray scattering studies of the magnetic nanostructure of stripe domains*, Ph.D. thesis, Universiteit van Amsterdam (2003).
- [79] J. Jackson, *Classical Electrodynamics*, (Wiley 1998).
- [80] L. Landau, E. Lifshitz, and L. Pitaevskii, *Electrodynamics of Continuous Media*, (Pergamon Press 1984).
- [81] D. Y. Smith, “Dispersion relations and sum rules for magnetorefectivity”, *J. Opt. Soc. Am.* **66**, 547 (1976).
- [82] D. Y. Smith, “Superconvergence and sum rules for the optical constants: Natural and magneto-optical activity”, *Phys. Rev. B* **13**, 5303 (1976).
- [83] J. Miguel, *Static and dynamic X-ray resonant magnetic scattering studies on magnetic domains*, Ph.D. thesis, Universiteit van Amsterdam (2005).
- [84] J. P. Hill and D. F. McMorrow, “X-ray Resonant Exchange Scattering: Polarization Dependence and Correlation Function”, *Acta Cryst. A* **52**, 236 (1996).
- [85] P. A. M. Dirac, “The Quantum Theory of Dispersion”, *Proc. R. Soc. London Ser-A* **114**, 710 (1927).
- [86] H. Kramers and W. Heisenberg, “Über die Streuung von Strahlung durch Atome”, *Zeitschrift für Physik* **31**, 681 (1925).

-
- [87] E. Fermi, *Nuclear Physics*, (University of Chicago Press 1950).
- [88] J. Hannon, G. Trammell, M. Blume, and D. Gibbs, “X-ray resonance exchange scattering”, *Phys. Rev. Lett.* **61**, 1245 (1988).
- [89] J. B. Kortright, “Resonant soft X-ray and extreme ultraviolet magnetic scattering in nanostructured magnetic materials: Fundamentals and directions”, *J. Electron. Spectrosc. Relat. Phenom.* **189**, 178 (2013).
- [90] S. Eisebitt, M. Lörngen, W. Eberhardt, J. Lüning, and J. Stöhr, “Lensless X-ray imaging of magnetic materials: basic considerations”, *Appl. Phys. A* **80**, 921 (2005).
- [91] J. Kortright, S.-K. Kim, G. Denbeaux, G. Zeltzer, K. Takano, and E. Fullerton, “Soft-x-ray small-angle scattering as a sensitive probe of magnetic and charge heterogeneity”, *Phys. Rev. B* **64**, 092401 (2001).
- [92] J. F. Peters, J. Miguel, M. A. de Vries, O. M. Toulemonde, J. B. Goedkoop, S. S. Dhesi, and N. B. Brookes, “Soft x-ray resonant magneto-optical constants at the Gd $M_{4,5}$ and Fe $L_{2,3}$ edges”, *Phys. Rev. B* **70**, 224417 (2004).
- [93] H. Mertins, S. Valencia, D. Abramssohn, A. Gaupp, W. Gudat, and P. Oppeneer, “X-ray Kerr rotation and ellipticity spectra at the 2p edges of Fe, Co, and Ni”, *Phys. Rev. B* **69**, 064407 (2004).
- [94] B. Vodungbo, J. Gautier, G. Lambert, A. B. Sardinha, M. Lozano, S. Sebban, M. Ducouso, W. Boutu, K. Li, B. Tudu, M. Tortarolo, R. Hawaldar, R. Delaunay, V. López-Flores, J. Arabski, C. Boeglin, H. Merdji, P. Zeitoun, and J. Lüning, “Laser-induced ultrafast demagnetization in the presence of a nanoscale magnetic domain network.”, *Nat. Commun.* **3**, 999 (2012).
- [95] X. Ge, M. Ducouso, W. Boutu, B. Tudu, B. Barbrel, D. Gauthier, A. Borta, A.-I. Gonzalez, F. Wang, B. Iwan, M. Billon, M. Perdrix, D. Guillaumet, F. Lepetit, B. Vodungbo, J. Gautier, R. Hawaldar, M. Tortarolo, R. Delaunay, P. Zeitoun, J. Lüning, and H. Merdji, “Sub-100 nanometer lensless probing of Co/Pd magnetic nanodomains using a table-top femtosecond soft X-ray harmonic source”, *J. Mod. Opt.* **60**, 1475 (2013).
- [96] Y. Ren, H. Zhao, Z. Zhang, and Q. Y. Jin, “Ultrafast optical modulation of exchange coupling in FePt/CoFe composite structure”, *Appl. Phys. Lett.* **92**, 162513 (2008).

- [97] J.-U. Thiele, S. Maat, and E. E. Fullerton, “FeRh/FePt exchange spring films for thermally assisted magnetic recording media”, *Appl. Phys. Lett.* **82**, 2859 (2003).
- [98] J. Viehhaus, F. Scholz, S. Deinert, L. Glaser, M. Ilchen, J. Seltmann, P. Walter, and F. Siewert, “The Variable Polarization XUV Beamline P04 at PETRA III : Optics, mechanics and their performance”, *Nucl. Instrum. Methods Phys. Res., Sect. A* **710**, 151 (2013).
- [99] M. Gilbert, H.-C. Mertins, M. Tesch, O. Berges, H. Feilbach, and C. M. Schneider, “TetraMag: a compact magnetizing device based on eight rotating permanent magnets.”, *Rev. Sci. Instrum.* **83**, 025109 (2012).
- [100] D. Nolle, M. Weigand, P. Audehm, E. Goering, U. Wiesemann, C. Wolter, E. Nolle, and G. Schütz, “Note: unique characterization possibilities in the ultra high vacuum scanning transmission x-ray microscope (UHV-STXM) ”MAXYMUS” using a rotatable permanent magnetic field up to 0.22 T.”, *Rev. Sci. Instrum.* **83**, 046112 (2012).
- [101] W. Demtröder, *Experimentalphysik 2*, (Springer 2004).
- [102] A. Kákay, E. Westphal, and R. Hertel, “Speedup of FEM Micromagnetic Simulations With Graphical Processing Units”, *IEEE T. Magn.* **46**, 2303 (2010).
- [103] T. A. Duckworth, F. Ogrin, S. S. Dhesi, S. Langridge, A. Whiteside, T. Moore, G. Beutier, and G. van der Laan, “Magnetic imaging by x-ray holography using extended references”, *Opt. Express* **19**, 16223 (2011).
- [104] G. Heldt, M. T. Bryan, G. Hrkac, S. E. Stevenson, R. V. Chopdekar, J. Raabe, T. Thomson, and L. J. Heyderman, “Topologically confined vortex oscillations in hybrid [Co/Pd]8-Permalloy structures”, *Appl. Phys. Lett.* **104**, 182401 (2014).
- [105] M. Kiwi, “Origin of the magnetic proximity effect”, *Mat. Res. Soc. Symp. Proc.* **746**, Q5.2.1 (2003).
- [106] G.-M. Choi, B.-C. Min, K.-J. Lee, and D. G. Cahill, “Spin current generated by thermally driven ultrafast demagnetization”, *Nat. Commun.* **5**, 4334 (2014).
- [107] C. Chen, Y. Idzerda, H.-J. Lin, N. Smith, G. Meigs, E. Chaban, G. Ho, E. Pellegrin, and F. Sette, “Experimental confirmation of the X-ray magnetic circular dichroism sum rules for iron and cobalt”, *Phys. Rev. Lett.* **75**, 152 (1995).

-
- [108] Y. Oba, H. Okamoto, T. Sato, T. Shinohara, J. Suzuki, T. Nakamura, T. Muro, and H. Osawa, “X-ray magnetic circular dichroism study on ferromagnetic Pd nanoparticles”, *J. Phys. D: Appl. Phys.* **41**, 134024 (2008).
- [109] M. A. Tomaz, T. Lin, G. Harp, E. Hallin, T. Sham, and W. O’Brien, “Comparison of x-ray magnetic circular dichroism at the L and M edges of Mo, Ru, Rh, and Pd”, *J. Vac. Sci. Technol. A* **16**, 1359 (1998).
- [110] R. Chimata, A. Bergman, L. Bergqvist, B. Sanyal, and O. Eriksson, “Microscopic Model for Ultrafast Remagnetization Dynamics”, *Phys. Rev. Lett.* **109**, 157201 (2012).
- [111] N. Kazantseva, U. Nowak, R. W. Chantrell, J. Hohlfeld, and A. Rebei, “Slow recovery of the magnetisation after a sub-picosecond heat pulse”, *Europhys. Lett.* **81**, 27004 (2008).
- [112] U. Atxitia, O. Chubykalo-Fesenko, N. Kazantseva, D. Hinzke, U. Nowak, and R. W. Chantrell, “Micromagnetic modeling of laser-induced magnetization dynamics using the Landau-Lifshitz-Bloch equation”, *Appl. Phys. Lett.* **91**, 232507 (2007).
- [113] G. P. Zhang, W. Hübner, G. Lefkidis, Y. Bai, and T. F. George, “Paradigm of the time-resolved magneto-optical Kerr effect for femtosecond magnetism”, *Nat. Phys.* **5**, 499 (2009).
- [114] J.-Y. Bigot, M. Vomir, and E. Beaurepaire, “Coherent ultrafast magnetism induced by femtosecond laser pulses”, *Nat. Phys.* **5**, 515 (2009).
- [115] E. Carpena, E. Mancini, C. Dallera, M. Brenna, E. Puppini, and S. De Silvestri, “Dynamics of electron-magnon interaction and ultrafast demagnetization in thin iron films”, *Phys. Rev. B* **78**, 174422 (2008).
- [116] D. Rudolf, *Femtosecond Spin Dynamics in Magnetic Multilayers Employing High Harmonics of Laser Radiation*, Ph.D. thesis, Universität Duisburg-Essen (2013).
- [117] T. Roth, *The Phenomenon of Laser-Induced Femtosecond Magnetism*, Ph.D. thesis, Technische Universität Kaiserslautern (2011).
- [118] A. Melnikov, I. Razdolski, T. O. Wehling, E. T. Papaioannou, V. Roddatis, P. Fumagalli, O. Aktsipetrov, A. I. Lichtenstein, and U. Bovensiepen, “Ultrafast Transport of Laser-Excited Spin-Polarized Carriers in Au/Fe/MgO(001)”, *Phys. Rev. Lett.* **107**, 076601 (2011).

- [119] M. A. Plötzing, *Ultrafast Demagnetization Dynamics in Ni_xPd_{1-x} alloys*, Diplomarbeit, RWTH Aachen (2011).
- [120] L. Guidoni, E. Beaurepaire, and J.-Y. Bigot, “Magneto-optics in the Ultrafast Regime: Thermalization of Spin Populations in Ferromagnetic Films”, *Phys. Rev. Lett.* **89**, 017401 (2002).
- [121] B. Koopmans, G. Malinowski, F. Dalla Longa, D. Steiauf, M. Fähnle, T. Roth, M. Cinchetti, and M. Aeschlimann, “Explaining the paradoxical diversity of ultrafast laser-induced demagnetization.”, *Nat.Mater.* **9**, 259 (2010).
- [122] S. Backus, C. G. Durfee III, M. M. Murnane, and H. C. Kapteyn, “High power ultrafast lasers”, *Rev. Sci. Instrum.* **69**, 1207 (1998).
- [123] O. Kfir, P. Grychtol, E. Turgut, R. Knut, D. Zusin, D. Popmintchev, T. Popmintchev, H. Nembach, J. M. Shaw, A. Fleischer, H. Kapteyn, M. Murnane, and O. Cohen, “Generation of phase-matched circularly-polarized extreme ultraviolet high harmonics for magnetic circular dichroism spectroscopy”, *ArXiv e-prints 1401.4101* (2014).
- [124] T. Pfeifer, C. Spielmann, and G. Gerber, “Femtosecond x-ray science”, *Rep. Prog. Phys.* **69**, 443 (2006).
- [125] E. Seres, J. Seres, F. Krausz, and C. Spielmann, “Generation of Coherent Soft-X-Ray Radiation Extending Far Beyond the Titanium L Edge”, *Phys. Rev. Lett.* **92**, 163002 (2004).
- [126] T. Popmintchev, M.-C. Chen, D. Popmintchev, P. Arpin, S. Brown, S. Alisauskas, G. Andriukaitis, T. Balciunas, O. D. Mücke, A. Pugzlys, A. Baltuska, B. Shim, S. E. Schrauth, A. Gaeta, C. Hernández-García, L. Plaja, A. Becker, A. Jaron-Becker, M. M. Murnane, and H. C. Kapteyn, “Bright coherent ultrahigh harmonics in the keV x-ray regime from mid-infrared femtosecond lasers.”, *Science* **336**, 1287 (2012).
- [127] M. Frolov, N. Manakov, and A. Starace, “Wavelength Scaling of High-Harmonic Yield: Threshold Phenomena and Bound State Symmetry Dependence”, *Phys. Rev. Lett.* **100**, 173001 (2008).
- [128] E. L. Falcão Filho, C.-J. Lai, K.-H. Hong, V.-M. Gkortsas, S.-W. Huang, L.-J. Chen, and F. X. Kärtner, “Scaling of high-order harmonic efficiencies with visible wavelength drivers: A route to efficient extreme ultraviolet sources”, *Appl. Phys. Lett.* **97**, 061107 (2010).

-
- [129] D. Popmintchev, M. Chen, C. H. García, J. A. Perez-Hernández, J. P. Siqueira, S. Brown, F. Dollar, B. C. Walker, P. Grychtol, L. Plaja, M. M. Murnane, H. C. Kapteyn, and T. Popmintchev, “Ultra-high-Efficiency High Harmonic Generation Driven by UV Lasers”, *CLEO: 2013 OSA Technical Digest* (online) (Optical Society of America), paper QW1A.5 (2013).
- [130] C. Hernández-García, J. A. Pérez-Hernández, T. Popmintchev, M. M. Murnane, H. C. Kapteyn, A. Jaron-Becker, A. Becker, and L. Plaja, “Zeptosecond High Harmonic keV X-Ray Waveforms Driven by Midinfrared Laser Pulses”, *Phys. Rev. Lett.* **111**, 033002 (2013).
- [131] T. Popmintchev, M.-C. Chen, P. Arpin, M. M. Murnane, and H. C. Kapteyn, “The attosecond nonlinear optics of bright coherent X-ray generation”, *Nat. Photonics* **4**, 822 (2010).
- [132] M.-C. Chen, C. Hernández-García, C. Mancuso, F. Dollar, B. Galloway, D. Popmintchev, P.-C. Huang, B. Walker, L. Plaja, A. Jaron-Becker, A. Becker, T. Popmintchev, M. M. Murnane, and H. C. Kapteyn, “Generation of Bright Isolated Attosecond Soft X-Ray Pulses Driven by Multi-Cycle Mid-Infrared Lasers”, *arXiv:1401.0240* (2014).
- [133] I. Kim, C. Kim, H. Kim, G. Lee, Y. Lee, J. Park, D. Cho, and C. Nam, “Highly Efficient High-Harmonic Generation in an Orthogonally Polarized Two-Color Laser Field”, *Phys. Rev. Lett.* **94**, 243901 (2005).
- [134] C. Winterfeldt, *Generation and control of high-harmonic radiation*, Ph.D. thesis, Julius-Maximilians-Universität Würzburg (2006).
- [135] R. Trebino, *Frequency-Resolved Optical Gating: The Measurement of Ultrashort Laser Pulses*, (Kluwer Academic 2002).
- [136] J. Diels and W. Rudolph, *Ultrashort laser pulse phenomena*, (Academic Press 2006).
- [137] C. La-O-Vorakiat, *Element-Selective Ultrafast Magnetization Dynamics with a Tabletop Light Source*, Ph.D. thesis, University of Colorado (2011).
- [138] A. J. Paul, *Coherent EUV Light from High-Order Harmonic Generation: Enhancement and Applications to Lensless Diffractive Imaging*, Ph.D. thesis, University of Colorado (2007).

- [139] S. Valencia, A. Gaupp, W. Gudat, H.-C. Mertins, P. M. Oppeneer, D. Abramsohn, and C. M. Schneider, “Faraday rotation spectra at shallow core levels: 3p edges of Fe, Co and Ni”, *New J. Phys.* **8**, 254 (2006).
- [140] Y. Iudin, Y. Kabanov, V. Nikitenko, X. Cheng, C. Chien, A. Shapiro, and R. Shull, “Magnetic field dependence of asymmetry in the magnetization reversal of ultrathin Co films and Co/Pt multilayers with perpendicular anisotropy”, *J. Magn. Magn. Mater.* **320**, 2044 (2008).
- [141] Y. Nie, X. Yang, P. Zhang, and H. Sang, “Magnetization and coercivity in Co/Pt multilayers with constant total Co layer thickness”, *Trans. Nonferrous Met. Soc. China* **20**, 819 (2010).
- [142] K.-H. Leitz, B. Redlingshöfer, Y. Reg, A. Otto, and M. Schmidt, “Metal Ablation with Short and Ultrashort Laser Pulses”, *Physics Procedia* **12**, 230 (2011).
- [143] W.-O. Siew, W.-K. Lee, H.-Y. Wong, T.-K. Yong, S.-S. Yap, and T.-Y. Tou, “Investigation of droplet formation in pulsed Nd:YAG laser deposition of metals and silicon”, *Appl. Phys. A* **101**, 627 (2010).
- [144] Z. Andreić, L. Aschke, and H.-J. Kunze, “The presence of droplets in pulsed laser deposition of aluminum with capillary ablation targets”, *Appl. Surf. Sci.* **153**, 235 (2000).
- [145] J. Kisielewski, W. Dobrogowski, Z. Kurant, A. Stupakiewicz, M. Tekielak, A. Kirilyuk, A. Kimel, T. Rasing, L. T. Baczewski, A. Wawro, K. Balin, J. Szade, and A. Maziewski, “Irreversible modification of magnetic properties of Pt/Co/Pt ultrathin films by femtosecond laser pulses”, *J. Appl. Phys.* **115**, 053906 (2014).
- [146] I. Robinson, I. Vartanyants, G. Williams, M. Pfeifer, and J. Pitney, “Reconstruction of the Shapes of Gold Nanocrystals Using Coherent X-Ray Diffraction”, *Phys. Rev. Lett.* **87**, 195505 (2001).
- [147] A. V. Martin, F. Wang, N. D. Loh, T. Ekeberg, F. R. N. C. Maia, M. Hantke, G. van der Schot, C. Y. Hampton, R. G. Sierra, A. Aquila, S. Bajt, M. Barthelmeß, C. Bostedt, J. D. Bozek, N. Coppola, S. W. Epp, B. Erk, H. Fleckenstein, L. Foucar, M. Frank, H. Graafsma, L. Gumprecht, A. Hartmann, R. Hartmann, G. Hauser, H. Hirsemann, P. Holl, S. Kassemeyer, N. Kimmel, M. Liang, L. Lomb, S. Marchesini, K. Nass, E. Pedersoli, C. Reich, D. Rolles, B. Rudek, A. Rudenko, J. Schulz, R. L.

-
- Shoeman, H. Soltau, D. Starodub, J. Steinbrener, F. Stellato, L. Strüder, J. Ullrich, G. Weidenspointner, T. A. White, C. B. Wunderer, A. Barty, I. Schlichting, M. J. Bogan, and H. N. Chapman, “Noise-robust coherent diffractive imaging with a single diffraction pattern”, *Opt. Express* **20**, 16650 (2012).
- [148] B. Abbey, K. A. Nugent, G. J. Williams, J. N. Clark, A. G. Peele, M. A. Pfeifer, M. de Jonge, and I. McNulty, “Keyhole coherent diffractive imaging”, *Nat. Phys.* **4**, 394 (2008).
- [149] S. Streit-Nierobisch, D. Stickler, C. Gutt, L.-M. Stadler, H. Stillrich, C. Menk, R. Frömter, C. Tieg, O. Leupold, H. P. Oepen, and G. Grübel, “Magnetic soft x-ray holography study of focused ion beam-patterned Co/Pt multilayers”, *J. Appl. Phys.* **106**, 083909 (2009).
- [150] J. Rodenburg, A. Hurst, A. Cullis, B. Dobson, F. Pfeiffer, O. Bunk, C. David, K. Jefimovs, and I. Johnson, “Hard-X-Ray Lensless Imaging of Extended Objects”, *Phys. Rev. Lett.* **98**, 034801 (2007).
- [151] S. Lee, W. Roseker, C. Gutt, B. Fischer, H. Conrad, F. Lehmkuhler, I. Steinke, D. Zhu, H. Lemke, M. Cammarata, D. Fritz, P. Wochner, M. Castro-Colin, S. O. Hruszkewycz, P. Fuoss, G. B. Stephenson, G. Grübel, and A. Robert, “Single shot speckle and coherence analysis of the hard X-ray free electron laser LCLS”, *Opt. Express* **21**, 24647 (2013).
- [152] M. D. Seaberg, D. E. Adams, E. L. Townsend, D. A. Raymondson, W. F. Schlotter, Y. Liu, C. S. Menoni, L. Rong, C.-C. Chen, J. Miao, H. C. Kapteyn, and M. M. Murnane, “Ultrahigh 22 nm resolution coherent diffractive imaging using a desktop 13 nm high harmonic source”, *Opt. Express* **19**, 22470 (2011).
- [153] G. Grübel, A. Madsen, and A. Robert, “X-ray photon correlation spectroscopy”, in R. Borsali and R. Pecora (Editors), “Soft-Matter Characterization”, chap. 18, (Springer, New York 2008).
- [154] O. G. Shpyrko, E. D. Isaacs, J. M. Logan, Y. Feng, G. Aeppli, R. Jaramillo, H. C. Kim, T. F. Rosenbaum, P. Zschack, M. Sprung, S. Narayanan, and A. R. Sandy, “Direct measurement of antiferromagnetic domain fluctuations.”, *Nature* **447**, 68 (2007).

- [155] M. Pierce, R. Moore, L. Sorensen, S. Kevan, O. Hellwig, E. Fullerton, and J. Kortright, “Quasistatic X-Ray Speckle Metrology of Microscopic Magnetic Return-Point Memory”, *Phys. Rev. Lett.* **90**, 175502 (2003).
- [156] M. S. Pierce, C. R. Buechler, L. B. Sorensen, S. D. Kevan, E. A. Jagla, J. M. Deutsch, T. Mai, O. Narayan, J. E. Davies, K. Liu, G. T. Zimanyi, H. G. Katzgraber, O. Hellwig, E. E. Fullerton, P. Fischer, and J. B. Kortright, “Disorder-induced magnetic memory: Experiments and theories”, *Phys. Rev. B* **75**, 144406 (2007).
- [157] C. Kocabas, S. Kang, T. Ozel, M. Shim, and J. Rogers, “Improved Synthesis of Aligned Arrays of Single-Walled Carbon Nanotubes and Their Implementation in Thin Film Type Transistors”, *J. Phys. Chem. C* **111**, 17879 (2007).
- [158] J. Goodman, *Speckle Phenomena in Optics: Theory and Applications*, (Roberts and Company 2006).
- [159] L. Müller, C. Gutt, B. Pfau, S. Schaffert, J. Geilhufe, F. Büttner, J. Mohanty, S. Flewett, R. Treusch, S. Düsterer, L. Mu, H. Redlin, A. Al-Shemmary, M. Hille, A. Kobs, R. Frömter, H. Oepen, B. Ziaja, N. Medvedev, S. Son, R. Thiele, R. Santra, B. Vodungbo, J. Lüning, S. Eisebitt, and G. Grübel, “Breakdown of the X-Ray Resonant Magnetic Scattering Signal during Intense Pulses of Extreme Ultraviolet Free-Electron-Laser Radiation”, *Phys. Rev. Lett.* **110**, 234801 (2013).
- [160] D. Paterson, B. E. Allman, P. J. McMahon, J. Lin, N. Moldovan, K. Nugent, I. McNulty, C. Chantler, C. Retsch, T. Irving, and D. Mancini, “Spatial coherence measurement of X-ray undulator radiation”, *Optics Communications* **195**, 79 (2001).
- [161] R. A. Bartels, A. Paul, H. Green, H. C. Kapteyn, M. M. Murnane, S. Backus, I. P. Christov, Y. Liu, D. Attwood, and C. Jacobsen, “Generation of spatially coherent light at extreme ultraviolet wavelengths.”, *Science* **297**, 376 (2002).
- [162] A. R. Sandy, L. B. Lurio, S. G. J. Mochrie, A. Malik, G. B. Stephenson, J. F. Pelletier, and M. Sutton, “Design and characterization of an undulator beamline optimized for small-angle coherent X-ray scattering at the Advanced Photon Source”, *J. Sync. Rad.* **6**, 1174 (1999).
- [163] C. W. Gayer, D. Hemmers, C. Stelzmann, and G. Pretzler, “Direct measurement of the x-ray refractive index by Fresnel diffraction at a transparent edge”, *Opt. Lett.* **38**, 1563 (2013).

- [164] C. La-O-Vorakiat, E. Turgut, C. A. Teale, H. C. Kapteyn, M. M. Murnane, S. Mathias, M. Aeschlimann, C. M. Schneider, J. M. Shaw, H. T. Nembach, and T. J. Silva, “Ultrafast Demagnetization Measurements Using Extreme Ultraviolet Light: Comparison of Electronic and Magnetic Contributions”, *Phys. Rev. X* **2**, 011005 (2012).
- [165] D. Boschetto, G. Mourou, A. Rouse, A. Mordovanakis, B. Hou, J. Nees, D. Kumah, and R. Clarke, “Spatial coherence properties of a compact and ultrafast laser-produced plasma keV x-ray source”, *Appl. Phys. Lett.* **90**, 011106 (2007).
- [166] M. T. Tavassoly, S. R. Hosseini, A. M. Fard, and R. R. Naraghi, “Applications of Fresnel diffraction from the edge of a transparent plate in transmission”, *Appl. Optics* **51**, 7170 (2012).

Publications

L.R. Schreiber, C. Schwark, S. Richter, C. Weier, G. Güntherodt, C. Adelman, C.J. Palmstrom, X. Lou, P.A. Crowell and B. Beschoten, "Triggering and probing of phase-coherent spin packets by time-resolved spin transport across an Fe/GaAs Schottky barrier", arXiv:1204.4371 (2012)

M. Opel, S.T.B. Goennenwein, M. Althammer, K.-W. Nielsen, E.-M. Karrer-Müller, S. Bauer, K. Senn, C. Schwark, C. Weier, G. Güntherodt, B. Beschoten and R. Gross, "Zinc oxide - From dilute magnetic doping to spin transport", *physica status solidi (b)* **251**, 1700–1709 (2014)

C. Weier, R. Adam, D. Rudolf, A. Kákay, D.E. Bürgler, R. Frömter, J. Bach, B. Beyersdorff, K. Bagschik, G. Winkler, A. Kobs, L. Müller, S. Schleiter, M.H. Berntsen, P. Grychtol, H.P. Oepen, H.C. Kapteyn, M.M. Murnane and C.M. Schneider, "Studying magnetic domains in ferromagnetic alloys and multilayers using soft X-ray scattering", *JARA-FIT Annual Report*, 133–134 (2014)

D. Wilson, D. Rudolf, C. Weier, R. Adam, G. Winkler, R. Frömter, S. Danylyuk, K. Bergmann, D. Grützmacher, C.M. Schneider and L. Juschkin, "Generation of circularly polarized radiation from a compact plasma-based extreme ultraviolet light source for tabletop X-ray magnetic circular dichroism studies" *Rev. Sci. Instrum.* **85**, 103110 (2014)

C. Weier, R. Adam, D. Rudolf, R. Frömter, P. Grychtol, G. Winkler, A. Kobs, H. P. Oepen, H.C. Kapteyn, M.M. Murnane, and C.M. Schneider, "Femtosecond-laser-induced modifications in Co/Pt multilayers studied with tabletop resonant magnetic scattering," *Europhys. Lett.* **109**, 17001 (2015)

Conference Contributions

DPG spring meeting, Berlin, Germany, 2012

"Magnetic resonant scattering with laser generated higher harmonic radiation", **poster**

DPG spring meeting, Regensburg, Germany, 2013

"Resonant magnetic scattering at magnetic domains in Co/Pt multilayers using laser-generated XUV light", **talk**

DPG spring meeting, Dresden, Germany, 2014

"Element-selective investigation of magnetic domain structure in CoPd and FePd alloys using small-angle soft X-ray scattering", **poster**

SNI, Bonn, Germany, 2014

"Investigation of the domain structure in magnetic multilayers and alloys using resonant soft X-ray scattering", **poster**

DPG spring meeting, Berlin, Germany, 2015

"Laser-induced modifications of Co/Pt multilayer films studied with tabletop resonant magnetic scattering", **poster**

XIV. DESY Research Course on X-ray Science, Hamburg, Germany, 2015

"Laser-induced modifications of Co/Pt multilayer films studied with tabletop resonant magnetic scattering", **poster** (awarded with a poster prize)

Danksagung

Ich möchte mich an dieser Stelle bei den Menschen bedanken, die diese Arbeit ermöglicht haben.

Als erstes bedanke ich mich bei **Prof. Claus M. Schneider**, der mir die Möglichkeit gegeben hat im Peter Grünberg Institut zu promovieren und stets eine offene Tür hatte, um wissenschaftliche Probleme zu besprechen.

Außerdem danke ich **Prof. Gerhard Grübel** für seine Bereitschaft die Arbeit als Zweitgutachter zu beurteilen.

Ich bedanke mich bei **Dr. Roman Adam** für die freundliche Aufnahme in die Lasergruppe und für seine motivierende Betreuung während der Arbeit.

Des Weiteren danke ich meinem Vorgänger **Dr. Denis Rudolf** für seine fachkundige Einweisung ins Laserlabor und für seine umfangreiche Hilfe im Verlauf der Arbeit.

Bei **Moritz Plötzing** bedanke ich mich für viele unterhaltsame und wissenschaftliche Diskussionen, für seine tatkräftige Unterstützung im Labor und für die musikalische Begleitung beim Experimentieren.

Dr. Patrik Grychtol sei gedankt für eine gemeinschaftliche Strahlzeit in Boulder und für seine hilfreichen Anregungen bei technischen und wissenschaftlichen Fragestellungen.

Alexander Bauer danke ich für seinen Einsatz bei den zeitaufgelösten Messungen der CoPd Proben.

Danksagung

Ich danke **Dr. Attila Kákay** für seine Einführung im Umgang mit TetraMag und für seine Interpretationen der experimentellen und theoretischen Ergebnissen.

Ganz herzlich bedanke ich mich für die Herstellung der Proben bei **Thomas Jansen**, **Dr. Daniel Bürgler** und **Markus Eschbach**.

Stefan Trellenkamp danke ich für das Elektronenstrahl Schreiben der PMMA-Gitter und **René Borowski** für seine Hilfe im Reinraum.

Außerdem bedanke ich mich für die technische Unterstützung von **Bernd Küpper**, **Heinz Pfeifer** und **Jürgen Lauer**.

Die **restlichen Mitabreiter des PGI-6** haben in den letzten Jahren zu einem sehr angenehmen Institutsklima beigetragen, wofür ich ebenfalls sehr dankbar bin. Dabei meine ich explizit die Teilnehmer der morgendlichen Kaffeerunde, die durch die vielen Erlebnisse abseits der Arbeit zu einem freundschaftlichen Miteinander beigetragen haben.

Des Weiteren möchte ich auch meinen Kollegen aus Hamburg danken, die an der Universität Hamburg oder am DESY arbeiten. In unzähligen, erlebnisreichen Strahlzeiten am PETRA III konnte ich dank dieser Menschen viele neue Erfahrungen sammeln. Besonderer Dank geht dabei an **Prof. Hans Peter Oepen** und **Dr. Robert Frömter**, die diese Zusammenarbeit ermöglicht und unterstützt haben. Die Experimente am Synchrotron wären zudem nicht denkbar gewesen ohne die sorgfältige Arbeit von **Judith Bach**, **Björn Beyersdorff**, **Kai Bagschik**, **Leonard Müller**, **Stefan Schleitzer** und **Magnus H. Berntsen**. Außerdem danke ich **Gerrit Winkler** und **André Kobs** für die Herstellung der Co/Pt-Vielfachschichten.

I deeply acknowledge the collaboration with JILA in Boulder and thank **Prof. Margaret M. Murnane** and **Prof. Henry C. Kapteyn** for their hospitality. Furthermore, I thank **Dr. Tenio Popmintchev**, **Dimitar Popmintchev** and **Dr. Daniel Adams**.

Zum Schluss möchte ich den Menschen danken, die mich in besonderer Art und Weise unterstützen egal in welcher Lebenslage. An erster Stelle möchte ich meiner langjährigen Freundin **Annika König** danken, die mir gerade in den letzten Monaten viel Liebe und Zuneigung gegeben hat.

Zudem danke ich meiner Familie **Kurt, Susanne** und **Claudia Weier**, die mir stets mit Rat und Tat beigestanden haben. Ebenso danke ich **Claudia, Winfried** und **Mareike König** sowie meinen restlichen Freunden und Bekannten, besonders meinem Mitbewohner **Eugen Michel**, dem ich viel Erfolg bei seiner Promotion wünsche.

Curriculum Vitae

Personal Data

Name	Christian Michael Weier
Address	Krakastr. 38 52064 Aachen
E-Mail	c.weier@fz-juelich.de
Birthday	10.06.1986
Birthplace	Bonn
Nationality	German

Education

03/2011–04/2015	Ph.D. work at PGI-6, Forschungszentrum Jülich on 'Resonant Magnetic Scattering Studies using Synchrotron Radiation and Laser-Generated Extreme Ultraviolet Light'
10/2009–10/2010	Diploma thesis at RWTH Aachen, II. Physikalisches Institut 'Optische Untersuchung der Spindynamik und der elektrischen Spininjektion in Zinkoxid'
09/2007 from 10/2005	'Vordiplom' in physics Studies of physics at RWTH Aachen
08/1996–06/2005	'Abitur', Emil-Fischer-Gymnasium in Euskirchen
09/1992–07/1996	Primary school in Euskirchen-Flamersheim

Erklärung

Hiermit erkläre ich, dass ich die vorliegende Arbeit selbstständig und ohne fremde Hilfe verfasst habe. Ferner habe ich außer den angegebenen Quellen keine anderen Quellen und Hilfsmittel benutzt. Die dem Sinn oder Wortlaut nach entnommenen Textpassagen oder Abbildungen habe ich in jedem Einzelfall kenntlich gemacht. Dieser Dissertation geht weder ein erfolgloser Promotionsversuch voraus, noch wurde sie in einem weiteren Promotionsverfahren eingereicht. Abgesehen von den angegebenen Publikationen sind die Ergebnisse dieser Dissertation unveröffentlicht. Diese Dissertation, die den Doktorgrad "Dr. rer. nat." anstrebt, wurde von Prof. Dr. C. M. Schneider betreut.

Jülich, 07.01.2015

Christian Weier

Band / Volume 91

6th Georgian-German School and Workshop in Basic Science

A. Kacharava (Ed.) (2014), CD

ISBN: 978-3-89336-991-1

Band / Volume 92

Ab initio investigations of π -conjugated-molecule-metal interfaces for molecular electronics and spintronics

M. Callsen (2014), viii, 155 pp

ISBN: 978-3-89336-992-8

Band / Volume 93

Ladungstransportmessungen an Si(111) Oberflächen mit einem Multispitzen-Rastertunnelmikroskop

M. Blab (2014), iv, 132, X pp

ISBN: 978-3-89336-997-3

Band / Volume 94

Functional Soft Matter

Lecture Notes of the 46th IFF Spring School 2015

23 February – 06 March, 2015 Jülich, Germany

ed. by J. Dhont, G. Gompper, G. Meier, D. Richter, G. Vliegenthart, R. Zorn (2015), ca. 600 pp

ISBN: 978-3-89336-999-7

Band / Volume 95

2-Steps in 1-pot: enzyme cascades for the synthesis of chiral vicinal amino alcohols

T. Sehl (2014), XIV, 167 pp

ISBN: 978-3-95806-001-2

Band / Volume 96

Immunohistochemical and electrophysiological characterization of the mouse model for Retinitis Pigmentosa, *rd10*

S. Biswas (2014), XII, 119 pp

ISBN: 978-3-95806-011-1

Band / Volume 97

Single molecule localization microscopy: Imaging of cellular structures and a new three-dimensional localization technique

X. Fan (2014), XII, 92 pp

ISBN: 978-3-95806-014-2

Band / Volume 98

Cryogenic Break-Junction Characterization of Single Organic Molecules

T. Grellmann (2014), VI, 86 pp

ISBN: 978-3-95806-015-9

Band / Volume 99

Interacting Interactions: A Study on the Interplay of Molecule-Molecule and Molecule-Substrate Interactions at Metal-Organic Interfaces

M. Willenbockel (2014), IX, 245 pp

ISBN: 978-3-95806-018-0

Band / Volume 100

Microwire crossbar arrays for chemical, mechanical, and thermal stimulation of cells

P. Rinklin (2015), xii, 184 pp

ISBN: 978-3-95806-022-7

Band / Volume 101

Modification and characterization of potential bioelectronic interfaces

K. Greben (2015), 76 pp

ISBN: 978-3-95806-028-9

Band / Volume 102

Extending the precision and efficiency of the all-electron full-potential linearized augmented plane-wave density-functional theory method

G. Michalíček (2015), 195 pp

ISBN: 978-3-95806-031-9

Band / Volume 103

Metabolic engineering of *Escherichia coli* for the production of plant phenylpropanoid derived compounds

P. V. van Summeren-Wesenhausen (2015), V, 92 pp

ISBN: 978-3-95806-039-5

Band / Volume 104

Spin-reorientation transition in epitaxial $\text{Ni}_x\text{Pd}_{1-x}$ films on Cu(001): a microscopic analysis

D. Gottlob (2015), x, 134 pp

ISBN: 978-3-95806-049-4

Band / Volume 105

Resonant Magnetic Scattering Studies using Synchrotron Radiation and Laser-Generated Extreme Ultraviolet Light

C. M. Weier (2015), vii, 143 pp

ISBN: 978-3-95806-052-4

Weitere **Schriften des Verlags im Forschungszentrum Jülich** unter
<http://wwwzb1.fz-juelich.de/verlagextern1/index.asp>

**Schlüsseltechnologien /
Key Technologies
Band / Volume 105
ISBN 978-3-95806-052-4**

